

**The Burst and Transient Source Experiment (BATSE)
Earth Occultation Catalog of Low-Energy Gamma-Ray Sources
Short title: BATSE Earth Occultation Catalog**

B. A. Harmon¹ C. A. Wilson, & G. J. Fishman

NASA Marshall Space Flight Center, SD50, Huntsville, AL 35812

colleen.a.wilson-hodge@nasa.gov

V. Connaughton, W. Henze, & W. S. Paciesas

University of Alabama in Huntsville, Huntsville, AL 35899

M. H. Finger, M. L. McCollough² M. Sahi, & B. Peterson

*Universities Space Research Association, SD50, NASA Marshall Space Flight Center,
Huntsville, AL 35812*

C. R. Shrader

*Universities Space Research Association, Code 661, NASA Goddard Space Flight Center,
Greenbelt, MD 20771*

J. E. Grindlay

Harvard-Smithsonian Center for Astrophysics, 60 Garden Street, Cambridge, MA 02138

D. Barret

*Centre d'Etude Spatiale des Rayonnements, 9 Avenue du Colonel Roche,
31028 Toulouse Cedex 04, France*

ABSTRACT

The Burst and Transient Source Experiment (BATSE), aboard the *Compton Gamma Ray Observatory* (CGRO), provided a record of the low-energy gamma-ray sky (\sim 20-1000 keV) between 1991 April and 2000 May (9.1y). BATSE monitored the high energy sky using the Earth occultation technique (EOT) for point sources whose emission extended for times on the order of the CGRO orbital period (\sim 92 min) or greater. Using the EOT to extract flux information, a catalog of sources using data from the BATSE large area detectors has been prepared. The first part of the catalog consists of results from the all-sky monitoring of 58 sources, mostly Galactic, with intrinsic variability on timescales of hours to years. For these sources, we have included tables of flux and spectral data, and outburst times for transients. Light curves (or flux histories) have been placed on the world wide web.

We then performed a deep-sampling of these 58 objects, plus a selection of 121 more objects, combining data from the entire 9.1y BATSE dataset. Source types considered were primarily accreting binaries, but a small number of representative active galaxies, X-ray-emitting stars, and supernova remnants were also included. The sample represents a compilation of sources monitored and/or discovered with BATSE and other high energy instruments between 1991 and 2000, known sources taken from the HEAO 1 A-4 (Levine et al. 1984) and Macomb & Gehrels

(1999) catalogs. The deep sample results include definite detections of 83 objects and possible detections of 36 additional objects. The definite detections spanned three classes of sources: accreting black hole and neutron star binaries, active galaxies and supernova remnants. The average fluxes measured for the fourth class, the X-ray emitting stars, were below the confidence limit for definite detection.

Flux data for the deep sample are presented in four energy bands: 20-40, 40-70, 70-160, and 160-430 keV. The limiting average flux level (9.1 y) for the sample varies from 3.5 to 20 mCrab (5σ) between 20 and 430 keV, depending on systematic error, which in turn is primarily dependent on the sky location. To strengthen the credibility of detection of weaker sources (\sim 5-25 mCrab), we generated Earth occultation images, searched for periodic behavior using FFT and epoch folding methods, and critically evaluated the energy-dependent emission in the four flux bands. The deep sample results are intended for guidance in performing future all-sky surveys or pointed observations in the hard X-ray and low-energy gamma-ray band, as well as more detailed studies with the BATSE EOT.

Subject headings: gamma rays: observations — methods: data analysis — occultations — surveys — X-rays: stars — catalogs

¹Present address: NE50, U.S. Department of Energy, 19901 Germantown Road, Germantown, MD 20874

²Present address: Harvard-Smithsonian Center for Astrophysics, 60 Garden Street, Cambridge, MA 02138

1. Introduction

The *Compton Gamma Ray Observatory* (CGRO)³, one of the four missions in NASA’s “Great Observatories” series, was launched in 1991 April and operated in low Earth orbit until its controlled re-entry in 2000 June. CGRO was responsible for many discoveries in the study of gamma-ray bursts, accreting binaries, active galaxies, and pulsars (see general reviews by Gehrels & Shrader 1997; Kniffen & Gehrels 1997; Leonard & Wanjek 2000). The quest for the origin of gamma-ray bursts (Meegan et al. 1992; Fishman & Meegan 1995) led to the development and flight of the Burst and Transient Source Experiment (BATSE) on the CGRO. In addition to BATSE’s primary science goals, its nine years of nearly continuous operation and all-sky capability allowed monitoring of the low-energy gamma-ray sky using the Earth occultation technique (EOT). Several new objects were discovered in the BATSE dataset with the EOT, and numerous outbursts of transient and periodic sources were detected during the mission. Here we present a compilation of BATSE EOT observations that can be used as the basis for more detailed studies on individual sources, for which it is important to have a knowledge of the long-lived emission in the BATSE energy range. It is our hope that these results will stimulate and guide future observations of the low-energy gamma-ray sky. In this work, we performed a careful assessment of systematic error in deriving results for the entire mission. The intent was to push the instrumental and technical limits of the present application of the BATSE Earth occultation technique (EOT). These data are made available on-line to other investigators through the High Energy Astrophysics Science Archive Research Center (HEASARC) at NASA Goddard Space Flight Center, the web site of the BATSE Earth Occultation Team at the NASA Marshall Space Flight Center, and the Compton Observatory Science Support Center (COSSC).

To make the presentation of this work tractable,

we divided the catalog into two parts. First, we emphasized the all-sky monitoring capability of BATSE. For the bright sources that vary on timescales greater than a few hours, we give an overview of activity and representative flux and spectral behavior. We also briefly make note of the science investigations performed with the EOT during the mission. Second, we performed a “sky survey” of a comprehensive set of low-energy gamma-ray sources. We note that this is not a true survey, in that it is biased by preselection of sources. The emphasis is on obtaining good quality results along the Galactic plane where accreting sources dominate the low-energy gamma-ray sky.

We note that other missions with all-sky or wide-field coverage were operational between 1991 and 2000. A non-exhaustive list includes the Japanese *Ginga* satellite, with its All-Sky Monitor, functioning between 1987 February and 1991 October (Tsunemi et al. 1989), and covering the bandpass of 1–20 keV, the scanning and imaging instruments aboard the French-Russian spacecraft *Granat* (Brandt, Lund, & Rao 1990; Roques et al. 1990; Sunyaev et al. 1990; Paul et al. 1991), which operated between 1989 December and 1997 October, and the U.S. *Rossi X-Ray Timing Explorer* (RXTE) mission, with its All-Sky Monitor (2–12 keV) (Bradt, Rothschild, & Swank 1993; Levine et al. 1996), which began operation in 1995 December and remains operational. *Granat*/Sigma (Roques et al. 1990), a coded mask, sodium iodide imaging detector system, provided considerable coverage and detailed images of the central region of the Galaxy in the 35–1300 keV bandpass. There were also scanning instruments of common design on board *Granat* and Danish *EURECA* spacecraft known as WATCH (Lund 1986; Brandt 1994; Castro-Tirado 1994) that monitored a portion of the X-ray sky in the 5–120 keV band. The powerful Wide Field Cameras (Jager et al. 1997) on the Italian-Dutch *BepoSax* satellite (1.8–28 keV) provided coded aperture imaging for both surveying and monitoring of large areas of the sky. BATSE complemented these instruments by full-sky monitoring of the energy range from 20 keV up to about 1 MeV. Much potential remains for investigations using combinations of these datasets.

³Acronyms and abbreviations used throughout the text and tables are listed in Appendix A.

BATSE served as an all-sky monitor using the Earth occultation technique (Harmon et al. 2002) between 1991 April 23 and 2000 May 28 (~ 9.1 y). This capability was used to trigger numerous pointed observations with the CGRO and other observatories. We extracted Earth occultation measurements from the BATSE dataset at a maximum rate of twice per 92m orbit of CGRO in sixteen energy channels between 20 keV and 1 MeV. Intensity data for any part of the sky, subject to the geometric constraints of occultation, were available for the duration of the mission with the exception of a few brief intervals (see Appendix B). Although the BATSE EOT was limited in sensitivity by high backgrounds and modest spatial resolution ($\sim 1^\circ$), we could investigate intensity and spectral variations over a dynamical range from days to years. Although \sim daily timescales have been accessible with pointed instruments, BATSE was the first all-sky monitor since those of *Vela 5B* (Conner, Evans, & Belian 1969) and *Ariel 5* (Holt 1976), to cover the upper end of this time range.

On the other hand, no low-energy gamma-ray full-sky surveys have been performed since the pioneering HEAO 1 A-4 experiment in 1977-79 (Levine et al. 1984). That experiment covered the energy range between 13 and 180 keV, and resulted in the detection of about 70 sources (7 of them extragalactic). Such a survey with BATSE has been attempted by our group in the past (Grindlay et al. 1996; Harmon et al. 1997) using the Earth occultation imaging technique (Zhang et al. 1993; Harmon et al. 2002). This did not prove to be an efficient way to survey the sky due to the limitations on computer time combined with residual features and the small size (a few degrees) of the images. A new effort, incorporating more sophisticated background modeling techniques developed for the *International Gamma-Ray Astrophysics Laboratory*(INTEGRAL)(Lei et al. 1999) and detector point spread functions for limb geometry, holds much promise for achieving this goal (Shaw et al. 2001, 2003). In Fig. 1 we compare the sensitivity of the BATSE deep sample (this work) with that of the HEAO 1 survey and a proposed future low-energy gamma-ray sky survey mission the *Energetic X-ray Imaging Survey Telescope* (EXIST) (Grindlay

et al. 2001, 2003). The binning of the BATSE sensitivity curve reflects the maximum energy resolution obtainable with the EOT.

In addition to the list of monitored sources accumulated during the operation of BATSE, we reviewed the HEAO 1 A-4 hard X-ray (Levine et al. 1984) catalog and the recent gamma-ray source compilation of Macomb & Gehrels (1999) for completeness of the known high energy Galactic sources, and performed a literature search of other high-energy objects above the BATSE sensitivity threshold. We did not include the EGRET “unidentified” sources from Macomb & Gehrels (1999) due to the probable extragalactic nature of many of them, and the relatively large uncertainty in location ($\sim 1^\circ$) that would strongly affect the measured flux using the EOT.

The sources addressed in this catalog are shown on a sky map in Galactic coordinates in Fig. 2. We have included 179 sources in our deep sample of the sky. The majority of sources are accreting binaries; however, we include the brighter sources from the other object classes for comparison. Of the 179 sources, most (76%) are accretors, i.e., black hole or non-pulsed neutron star binaries (97), or binaries containing pulsars (41). Again we stress that our deep sampling of the known gamma-ray sources should not be considered as a true background-limited survey to a given brightness threshold. However, by virtue of our comparisons to HEAO 1 A-4 survey data, we believe that we have a reasonably complete sampling of high energy accreting systems in the Milky Way Galaxy down to an average flux level of ~ 30 mCrab (20-100 keV).

We also note that to date, samples of objects have been performed with BATSE for active galaxies (Connaughton et al. 1999; Malizia et al. 1999; Bassani et al. 2000), supernova remnants (McCollough et al. 1997), globular clusters (Ford et al. 1996), X-ray stars (White et al. 1994), and prompt emission from nearby novae (Hernanz et al. 2000). The most promising classes of sources, other than accreting binaries, for which BATSE has shown positive detections, are active galaxies, such as Seyferts and blazars, and supernova remnants. As part of our 179-source sam-

ple, we included selected supernova remnants (17) (some of which contain pulsars or soft gamma-ray repeaters (SGRs)), active galaxies (12), and X-ray emitting stars (12), that overlap these other studies.

In Sec. 2, we give a brief overview of BATSE and the use of the Earth occultation technique. We then discuss production details for the catalog. In Sec. 3 we present highlights of the all-sky monitoring effort, and give an overview of science obtained for the different classes of detected sources. Sec. 4 presents the deep sample results and how they are organized. We describe a sky-dependent systematic error model and apply it to the measured source fluxes. We then examine the consistency of source detections by focusing on some of the weak sources in the few mCrab intensity range. This is done by testing with methods that are independent of the occultation step fitting routines. Finally, in Sec. 5, we briefly discuss applications of the catalog data.

2. Analysis Methods and Treatment of Point Source Data

2.1. The BATSE Instrument and the Earth Occultation Technique

The Earth occultation analysis technique utilizes the large area detectors (LADs) on BATSE, which are sensitive to photons above 20 keV. The *Compton Gamma Ray Observatory* including placement of the BATSE detector modules on the spacecraft is illustrated pictorially in Fig. 3. The LADs are composed of sodium iodide (NaI(Tl)) crystals, 1.27 cm (0.5 in) thick by 50.8 cm (20 in) across (2025 cm² total area of one detector). Eight modules are mounted on the corners of the CGRO with normal vectors perpendicular to the faces of a regular octahedron. Any point on the sky can be viewed by four detectors at angles less than 90° to the source direction. For the EOT, the measurement sensitivity of the LADs is maintained by combining statistics from two, three and ultimately four detectors at successively larger angles from any one of the detector normals. A full description of the BATSE detectors and the exper-

iment can be found, for example, in Fishman et al. (1984, 1989a,b). In a companion paper to this catalog (Harmon et al. 2002, see also references therein), we discussed the use of the EOT in various forms, and described in detail a number of aspects of the technique such as source identification, sensitivity, and systematic error. The Earth occultation technique was also developed and applied to BATSE data in a separate, parallel effort at the Jet Propulsion Laboratory (JPL) (Skelton et al. 1994; Ling et al. 1996, 2000; Ling & Wheaton 2003). We discuss our results in comparison to this work in Appendix C.

In one orbit around the Earth, two occultation step features, a rise and set pair, will be superimposed on the background counting rate as each point source is occulted. A measurement can be made of the intensity of a source in each energy channel at rise or set. In practice, two measurements per orbit were not always achieved. The most common reasons were passages through the lower Van Allen radiation belt at the South Atlantic Anomaly when the detector high voltage was off, or that CGRO was out of line-of-sight contact with the NASA Tracking & Data Relay Satellites, or data were flagged and not available for analysis. In addition, high declination sources ($|\delta| \geq 41^\circ$) experience an interruption of occultations near the orbital poles (see Harmon et al. 2002), and source confusion, where occultations of one source are indistinguishable from another, limits the number of usable occultation steps. The combined impact of these effects caused Earth occultation coverage averaged over one precession cycle (~ 52 d) to range between 80%-90%, at best, and at worst, about 50%. The count rate for a source in the LAD was extracted by simultaneously fitting occultation step features with terms for each source in the fit and a quadratic polynomial to represent the detector background. The fit was performed independently for each LAD and in each energy channel.

Occultation steps (lasting ~ 10 s) are relatively sharp features superimposed on the slower background variations caused by orbital motion around the Earth. We assumed that the background was smooth and adequately fit by a second order polynomial. Occasional failures of this assumption were usually caused

by the presence in the data of bright pulsars, weak bursts, solar flares, and other disturbances on the timescale of the fitting window. Generally, in the absence of unusual background fluctuations, we have found that the LADs were consistently reproducible in the measured fluxes based on tests using the Crab Nebula fluxes in a given detector, angle and energy bin. The only exception to this was the late mission (approx. last two years) loss of gain stabilization in LAD 7. We took this considerably further, however, to reduce measurement inconsistencies between LADs that might be intermittent (unusual background fluctuations), and LAD-response related (time-independent effects). We did this by (1) performing a flagging procedure for outliers at the single step level (see Harmon et al. 2002, Sec 2.2, page 152), and also outlined in Sec 2.3 of this manuscript), and (2) developing an empirical correction to the detector response based on the Crab data in channels 1-10 in all eight LADs at angles between 0 and 90 degrees (see Harmon et al. 2002, Sec 3.5, pages 167-170). All light curves and spectra in the catalog were subjected to these two procedures except for a few sources as noted in Sec. 2.3. Any remaining non-Poissonian components in the data must then be accounted for in estimating systematic errors, which we have done on an average basis using a grid-interpolation procedure as discussed in Sec 4.2. More details of the properties of Earth occultation features and how the EOT was used can be found in Harmon et al. (2002).

2.2. Treatment of Catalog Data

A raw count rate history for each point source was accumulated from fitting occultation steps on successive days (usually about 15-30 steps per day). The instrument response was deconvolved in a following step to produce intensities in units of photon number, energy flux, or units relative to a reference source, such as the Crab Nebula. The process of generation and analysis of the occultation count rate histories is shown schematically in Fig. 4. The raw light curves, uncorrected for detector response, were generated with a software package known as OF_W. The code carries or collects all information on

source location, spacecraft orientation and trajectory, detector gains, and a limited amount of data on relative source intensity, required to extract source count rates from occultation step features in the BATSE CONT (2.048s, 20-1000 keV in 16 energy channels) data (see Fishman et al. 1989a,b, for a more complete description of datatypes).

In Table 1, we show the standard input parameters for OF_W. The definitions of these parameters are: (1) 2τ , length of the background data sample in seconds. The data that define the *fitting window* were selected to be symmetric about the occultation step of the source of interest (SOI). From an analysis of relative size of systematic error to the statistical error using the second-degree polynomial for the background (Shaw et al. 2001), a value for τ of ~ 110 s was found to be optimal. We also allowed an additional non-adjustable time of 20s for the width of the occultation step itself. (2) θ_{cut} is the maximum detector aspect angle of a source (i.e., the angle between the detector normal vector and the vector toward the source) allowed for source measurement. Since there was no improvement in the signal-to-noise ratio by combining data from detectors beyond about 60° , this was a convenient cutoff for choosing which detectors were used. This value produced a combination of one to four LADs depending on CGRO orientation. The only exceptions to this were cases where a small range of azimuthal viewing angles were occasionally blocked by the CGRO high gain antenna. When this occurred we excluded these LADs from the measurement. (3) θ_{int} is the maximum detector aspect angle for a source, with an occultation step time in the fitting window of the SOI, that must be simultaneously fit with the SOI (Harmon et al. 2002, see for fitting model details). A value of 70° was selected because bright sources such as the Crab or Cygnus X-1 still have substantial flux even at very large aspect angles. (4) δ is the minimum time separation between occultations of two sources in the fitting window that were allowed separate terms in the fit. If the times of the SOI and an interfering source fell within the fitting window and satisfied the aspect angle criteria, but were within $\delta=10$ s, then the fit was rejected by OF_W. (5) λ is the minimum fraction of data packets

accepted for an occultation step fit. The acceptance criterion helped to minimize potentially singular matrices and other instabilities in the fitting routines. For this work, λ was set at 95%. Finally, (6) ϕ_{cr} is the threshold photon flux, which if exceeded, caused OF_W to add a fitting term for an occultation step of a source within the fitting window of the SOI, provided criterion (4) was not invoked. A database was kept of sources that were found from previous passes through the BATSE dataset to exceed ϕ_{cr} for intervals of more than a few minutes, and typically a day or longer. The value of ϕ_{cr} , 0.01 photons $\text{cm}^{-2}\text{s}^{-1}$, refers to the energy band of 20-100 keV, which we took as our standard band for this work.

In addition to a list of sources for measurement, OF_W requires the following databases as also noted in Fig. 4.

2.2.1. Flare and Eclipse Databases

To optimize the sensitivity of the EOT, we tried to minimize the number of source terms (SOI + potentially interfering sources) in the fitting window. A database of source outburst times, and intensity bands provides information to determine whether terms for other sources should be included in the fit. This database was built up as new sources were found either through occultation analysis (light curves and images) or observations with other instruments.

Information about source outburst intensity levels as a function of time was read from the database by OF_W before the flux measurement was performed. For a first complete pass through the BATSE dataset (which we refer to as the “first iteration”), ϕ_{cr} was set at 0.02 photons $\text{cm}^{-2}\text{s}^{-1}$ (20-100 keV, ~ 75 mCrab). Sources dimmer than this threshold, however, were found to introduce significant interference in our measurements. For this work (the second iteration), we lowered ϕ_{cr} to 0.01 photons $\text{cm}^{-2}\text{s}^{-1}$ (20-100 keV, ~ 35 mCrab). In Table 2, we show the sources that consistently exceeded ϕ_{cr} (identified as “persistent sources”), along with their average flux, and for Table 3, we show those that exceeded ϕ_{cr} for an identifiable, but limited period of time. Although a wide

variety of source behavior was observed with BATSE (See also the assessment of the RXTE ASM data by Bradt et al. (2000)), Table 3 sources were broadly classified as “transient sources”, although duty fractions could range from $<1\%$ up to 90%. If the beginning and ending times of the fitting window fell within the outburst interval of a potentially interfering transient source, and it met the usual geometric criteria, a fitting term was included. For this particular iteration of the catalog, we have added a number of low-level outbursts for the transient sources in Table 3 not previously reported in other publications. Some special notes regarding the detection and monitoring of transients are given in Appendix A.

A few bright X-ray binaries containing neutron stars, Her X-1, 4U 1700-377, Vela X-1, Cen X-3, and OAO 1657-415, undergo complete eclipses by their companion stars and have well-documented ephemerides (see Fig. 5). We took advantage of this in the fitting process by eliminating interfering source terms for these sources during eclipse. Comparison of the eclipse times to the fitting window times were made in the solar system barycentric frame (Standish et al. 1992).

2.2.2. CGRO Orientation History

CGRO was 3-axis stabilized, and maintained the same orientation for extended periods, typically 2-week intervals. The CGRO orientation was defined by the right ascension and declination of X and Z-axes of the spacecraft in J2000 coordinates, and was used to determine the optimum detectors for the occultation measurement of the SOI and potentially interfering sources.

2.2.3. BATSE CONT Channel Energy Binning Lookup Table

The sixteen channel CONT data had programmable energy bins. These were usually kept to a standard set of values (see Appendix B), except for occasional changes that were made to allow higher resolution

measurements of sources with strong spectral cutoffs such as pulsars and SGs. Energy calibration of the bin boundaries or “edges” are required to obtain photon fluxes. They are also used to compute small electronic deadtime corrections in OF_W, which depend on the total observed counting rate (source + background).

2.3. Data Flagging and Computation of Photon Fluxes

Before deconvolution of the detector response, we flagged (i.e., excluded) any remaining large outliers from the single step raw light curve files. The two reasons for doing this were to place a tighter limit on obviously unphysical fitting results, and to exclude data contaminated by background fluctuations that flagging by daily visual inspection failed to remove (Harmon et al. 2002). Both of these situations were relatively rare; however, they could produce spurious daily flux averages. We settled on a scheme that could be implemented without special treatment of individual sources, and was based on a filter for variations from an average flux level. In this scheme, we averaged the count rate from a source for each CGRO observing period, and subtracted the average from the rates (channels 1-10) over the same period. We then made a cut on the rates at $\pm 3.5\sigma$ to remove outliers. This approach worked well for all sources except those that showed strong variations of 0.5-1 Crab on timescales of minutes to a few hours. The persistent sources that fell into this category were Cyg X-1, Sco X-1, 4U 1700-377, and Vela X-1. A few of the brighter, highly variable transient sources also exceeded this variability criterion during outburst. Typically, the percentage of rates rejected in this way was less than 5% for the majority of sources, and did not significantly affect the measured fluxes and uncertainties. However Cyg X-1 could, at times, have rejection rates as high as 13%. We therefore converted count rate data to photon fluxes for these four persistent sources without this flagging procedure. For the bright transient sources, we visually inspected the raw light curves during the times listed in Table 3, and removed flags on apparently

good data that were set by the automated flagging procedure.

Two methods were developed to obtain flux and spectral information from the BATSE occultation count rate data. The first method is a fitting procedure used commonly in high energy astronomy called “forward-folding” (Briggs 1995), where we assumed a spectral model that was a reasonable representation of a source flux in the LAD energy range. Then the selected model was folded through the instrument response (Pendleton et al. 1995) for the illuminated detectors to determine model count spectra. The count data were fit, by varying the model parameters, in a chi-square minimization procedure. Finally the best fitting model was integrated over the desired energy range to determine the photon flux. This method avoids a potentially unstable inversion of the BATSE response matrices, which have large off-diagonal elements due to the LAD’s relatively shallow detection depth and lack of Compton suppression. It lends itself well to generation of multi-channel spectra, obtaining photon fluxes in a desired energy range, and performing broad-band spectral analyses. For the spectral analysis results in Tables 2 and 3, we used a widely available code known as XSPEC (Arnaud 1996), and for the flux history generation, a code developed locally for specific use with Earth occultation data known as HISGEN (see Fig. 4). Both codes use forward-folding to estimate photon fluxes. The second method uses the Crab (Harmon et al. 2002, see for an example spectrum) as a standard candle by obtaining a ratio of the count rate for a given source relative to that of the Crab in the same detector orientation and energy channel. This is convenient for computing hardness ratios, epoch folding and investigating the deep sample results discussed later. The resulting fluxes were less model dependent than those using the forward-folding method.

Four energy bands in Crab-relative units were selected to report the results of the deep sample in Sec. 4: 20-40, 40-70, 70-160, and 160-430 keV. The energy binning is somewhat constrained by the CONT data channel binning scheme (see Appendix B, Table B1). And, although the LADs have some sensitivity to fluxes in excess of 430 keV, we chose not to include

a higher energy band due to statistics (a relative lack of positive detections at higher energy), and the self-consistent treatment of systematic error which was based on a study only in the 20-100 keV range. Conversion factors from the reported four-band Crab relative intensities to photon and energy fluxes can be found in Appendix B, Table B2.

3. BATSE All-Sky Monitor Results

High voltage was first applied to the Large Area Detectors on Truncated Julian Date (TJD) 8362, or 16 April 1991. Final shutdown occurred on TJD 11691, or 26 May 2000. Data were available between TJD 8362 and 11690, except for a few brief periods due to orbital reboots and occasional mission anomalies as listed in Appendix B. Light curves and representative spectra for the sources considered persistent or transient by OF_W (a total of 58 objects) can be found on the web at <http://gamma-ray.msfc.nasa.gov/batse/occultation> in visual as well as tabular form. Table 2 is a list of the “persistent (P)” sources known by the EOT flux history generator OF_W (see Fig. 4). Likewise, transient (T) sources in the BATSE flare database appear in Table 3. The tables carry information about source type, characteristic spectral data, outburst times, and energy flux for these sources in the 20–100 keV band.

Of the four general classes of sources represented in this catalog (x-ray binaries, supernova remnants/pulsars/SGRs, AGNs and x-ray stars), three are represented in Tables 2 and 3. The brightest sources in the BATSE database are clearly dominated by X-ray binaries (both HMXBs and LMXBs), but we also found one supernova remnant/pulsar (the Crab), and three galaxies (Centaurus A, Markarian 501, and NGC 4151). No X-ray stars were bright enough to be included. In the following sections we will briefly describe science investigations of these source classes using BATSE EOT results.

3.1. Black Hole Systems

Among the persistent black hole candidates, Cygnus X-1 (e.g., Ling et al. 1997; Paciesas et al. 1997; Zhang et al. 1997a; Brockopp et al. 1999b; Zdziarski et al. 2002), Cygnus X-3 (McCollough et al. 1999), GX 339-4 (e.g., Harmon et al. 1994; Rubin et al. 1998) 1E 1740-29 and GRS 1758-258 (e.g., Zhang, Harmon, Liang 1997c; Smith et al. 2002) have been studied most extensively using the BATSE EOT. Emission in the low-energy gamma-ray range is understood to be primarily upscattered low-energy photons by the inverse Compton process. BATSE studies have illustrated both spectral and intensity variations associated with state transitions (e.g, high (soft), low (hard) and off states) of black hole binaries. Such state transitions are thought to be driven by changes in the mass accretion rate. A prime example of this phenomenon is the 1996 hard-soft-hard state transition in Cyg X-1, which was monitored in both X-rays (2-12 keV) with RXTE/ASM and low-energy gamma-rays with BATSE (Zhang et al. 1997a; Esin et al. 1998; Zdziarski et al. 2002). These sources have also been found to exhibit rather closely correlated radio flux variations: 1E 1740-29 (Sunyaev et al. 1991; Mirabel et al. 1992), GX 339-4 (Fender et al. 1999), and Cyg X-3 (McCollough et al. 1999). In Fig. 6, we show the 9.1y flux histories for four of the more persistent black hole candidates. It can be seen, that, in addition to the periods of low gamma-ray flux (soft state) in Cyg X-1 around TJD 9400 and 10270, all of these sources show extended periods of low level activity. The low intensity or “quenched” state of Cyg X-3, in particular, precedes violent radio flaring and jet activity (McCollough et al. 1999).

Bright transients (\sim 200 mCrab or more) such as GRO J0422+32 (Shrader et al. 1994; Callanan et al. 1995; van der Hooft et al. 1999; Ling & Wheaton 2003), GRO J1655-40 (Harmon et al. 1995; Zhang et al. 1997b), GRS 1915+105 (Foster et al. 1996; Paciesas et al. 1996; Harmon et al. 1997), and XTE J1550-564 (Corbel et al. 2001; Wu et al. 2002) have been detected at an average rate of about 1 per year. In Fig. 7, we show the flux histories of several bright black hole transients. Some have confirmed optical

mass functions with lower limits exceeding the theoretical mass of a neutron star. Most have very bright high energy spectral tails extending to several hundred keV, and thus, even without firm mass limits, are considered likely to be black holes. These transients reach maximum brightness within a day to a few days with highly variable and generally unpredictable multiple outbursts over an interval of months to years following the initial outburst. The overall brightness of the secondary outbursts tends toward lesser intensity over time (GRS 1915+105 being an exception). Sometimes there is an apparent return to X-ray quiescence between outbursts, e.g., GRO J1655-4 (Orosz et al. 1997). Transitions occur between high, low, very high and/or intermediate states (Corbel et al. 2001), with spectral shapes and luminosity levels that appear to be the same as the persistent black hole systems. Radio spectral density measurements and long baseline interferometry of black hole transients at times reveal compact radio sources, and, with lesser regularity, extended high velocity ($\sim 0.3 - 0.9c$) radio-emitting jets (Mirabel & Rodriguez 1994; Hjellming & Rupen 1995; Tingay et al. 1995). The jet formation is sometimes associated with high energy outbursts (Harmon et al. 1995, 1997).

3.2. Low Mass X-Ray Binaries with Neutron Stars

Low mass X-ray binaries containing neutron stars detected by BATSE fall into two general categories, usually known as “atoll” and “Z” sources. The names are based on the X-ray spectral behavior (generally below the sensitive energy range of the LADs) where four energy bands are plotted as paired hardness ratios on a two-dimensional diagram (a color-color diagram). As the source intensity varies with time, the combined ratios will tend to trace out a Z or atoll-like track on the diagram. The physical differences between the two NS LMXB categories are not completely known. In particular, atoll sources tend to emit X-ray bursts, and have spectral states that resemble those of black hole binaries.

The realization that many LMXB X-ray burst sources produce significant emission above a few keV came as a result of observations with *Granat*/Sigma (Barret & Vedrenne 1994) and BATSE (Tavani & Barret 1997; Barret 2001). In pulsars, high energy radiation is produced by acceleration of particles in the strong magnetic fields ($\geq 10^{12}$ G) near the polar regions of the neutron star. The bursters are thought to have substantially weaker fields and should be inefficient particle accelerators. In addition, the presence of the neutron star surface is thought to generate a large flux of soft photons, effectively cooling surrounding plasma, and suppressing high energy emission. Nevertheless, a number of burst sources, e.g., KS 1731-260, 1E 1724-308 (Barret & Vedrenne 1994), Aql X-1 (Harmon et al. 1996), 4U 1608-522 (Zhang et al. 1996b), 4U 0614+091 (Ford et al. 1997), and GX 354+0 (Claret et al. 1994), show significant gamma X-ray flux, at times, in excess of 100 keV. They are considerably less luminous in the low-energy gamma-ray range relative to black hole LMXB systems, $\sim 0.05 - 0.1 L_{Edd}$ (Barret et al. 2000), which is probably related to the presence of the neutron star.

The spectra of LMXB bursters are similar to those of black hole systems, typically consisting of a soft, disk component with temperatures of a few keV and a low-energy gamma-ray tail. The spectra of these sources sometimes show a cutoff of 50-60 keV, but not always, and may extend to higher energy. Comparisons with soft X-ray measurements indicate that these sources exhibit anticorrelations between X-ray luminosity and spectral hardness (van Paradijs & van der Klis 1994; Ford et al. 1997), and thus, as in BHCs, spectral behavior of the LMXB NS systems should be governed by mass accretion rate. Whether or not NS binaries have equivalent spectral states to BH binaries is not clear, but these observations support the picture of a neutron star surrounded by an accretion disk as in BH systems, differing only at the innermost regions of the disk. Models involving boundary layers between the disk and neutron star surface have been devised, although broad-band spectral observations do not as yet strictly require conditions that are unique to neutron star binaries.

In Fig. 8, we show examples of persistent and

transient LMXBs containing neutron stars detected with BATSE. BATSE observations have shown that the gamma-ray flux from neutron star LMXBs varies over intervals of a few days or longer. Aquila X-1 was observed to have extended outbursts of many months in the low-energy gamma-ray band (Harmon et al. 1997) similar to LMXB BHCs. These outbursts were correlated with an increase in brightness of its optical counterpart *V1333 Aquilae*. 4U 1608-522 shows similar duration outbursts, one of which was bright enough to establish that the high energy spectrum had a high energy cutoff of about 60 keV (Zhang et al. 1996b). GS 1826-238, a source once thought to be a black hole candidate, was observed to produce X-ray bursts with *BeppoSax* (Ubertini et al. 1997), and therefore is clearly a neutron star system. The source reached a level of ~ 0.01 ph cm $^{-2}$ s $^{-1}$ around TJD 10000, and remained roughly a factor of 2 brighter as of mission end.

There is also mounting evidence that the Z-type LMXBs, e.g., Sco X-1 (Strickman & Barret 2000; D'Amico et al. 2001), GX 17+2 (Di Salvo et al. 2000), and GX 349+2 (Di Salvo et al. 2001), exhibit transient high energy radiation as do the atoll sources discussed above. These spectral tails carry only a few percent of the total luminosity of the source (Barret 2001), and it is unclear whether the high energy emission in the Z sources is the same spectral component more commonly seen in the atoll sources. So far, the presence of such hard tails has not been significantly investigated in the BATSE database, although the two bright Z-sources Sco X-1 and GX 17+2 were detected in the deep sample in excess of 160 keV (see Sec. 4).

3.3. Pulsed Sources

Accreting X-ray pulsars were primarily studied with BATSE using pulse frequency and pulsed flux measurements (Bildsten et al. 1997; Finger et al. 1999; Wilson-Hodge 1999; Wilson et al. 2002, 2003) that in general are more sensitive than EOT data. However, EOT fluxes been used to obtain pulse fractions, study correlations between the spin-up rate and total flux,

and for the characterization of apastron outbursts. EOT light curves for several accreting X-ray pulsars are shown in Fig. 9.

The most common use of EOT measurements has been to estimate the pulse fraction, i.e., the ratio of the pulsed flux to the mean flux (pulsed + unpulsed) in conjunction with simultaneous or approximately simultaneous pulsed flux measurements. These measurements, along with orbital parameters, can be used to investigate changes in the accretion environment, which can depend on a number of system properties such as disk-induced torques on the neutron star and the circumstellar environment of the companion. Formal pulsed fractions, using simultaneous data, have been computed for several sources including: GRO J1744-28, 25%, 20-40 keV, TJD 10092-10098 (Finger et al. 1996a), GX 301-2, $\sim 50\%$, 20-55 keV (Koh et al. 1997), GRS 0834-430, 10-15%, 20-70 keV, outbursts in 1991 and 1992 (Wilson et al. 1997a), EXO 2030+375, 36(5)%, 30-70 keV, TJD 9120-9131 (Stollberg et al. 1999), GRO J1008-57, 67(4)%, 20-70 keV, TJD 9186-9195 (Bildsten et al. 1997), A 0535+262, varied from $> 80\%$ at lowest flux to 30% at highest flux in giant outburst (Finger, Wilson, & Harmon 1996b; Bildsten et al. 1997), and GRO J2058+42, 36(3)%, 20-70 keV, TJD 9971-10018 (Wilson et al. 1998). Less rigorously determined pulse fractions, with approximately simultaneous data and some model-dependency, have been computed for 4U 1145-619, widely varying from 28(4)-70(20)%, 20-50 keV, TJD 8678-10742 (Wilson et al. 1994; Wilson-Hodge 1999), GS 1843+00, 7%, 20-50 keV, TJD 10515-10516 (Wilson et al. 1997b), and 4U 0115+63, 40-60%, 20-50 keV, TJD 11231 (Wilson et al. 1999).

Simple accretion theory predicts a correlation between bolometric flux F and spin-up rate $\dot{\nu}$ in X-ray pulsars, described by a power law $\dot{\nu} \propto F^{6/7}$. Using EOT data, this correlation has been fitted for the giant outbursts of GRO J2058+42 (Wilson et al. 1998) and A0535+262 (Finger, Wilson, & Harmon 1996b). This correlation indicates the likely presence of an accretion disk, because disk accretion is more efficient at transferring angular momentum than wind accretion. Furthermore, a correlation between the frequency of quasi-periodic oscillations and the 20-

100 keV flux measured with the EOT was consistent with predictions of either the beat frequency or Keplerian frequency models, confirming the presence of an accretion disk in A0535+262 (Finger, Wilson, & Harmon 1996b).

Using dynamic power spectra of BATSE EOT and RXTE ASM data, Clarkson et al. (2003) showed that the \sim 60-day superorbital period previously known in SMC X-1 changed smoothly from 60 days to 45 days and then returned to its former value on a time-scale of approximately 1600 days, varying in a coherent, almost sinusoidal, manner. They interpreted this variation as consistent with a radiation-driven warping model of the accretion disk.

Pravdo et al. (1995) and Pravdo & Ghosh (2001) folded EOT intensity histories at the 41.498 day orbital period of GX 301–2 from 1993 September - 1994 July (TJD 9258-9561). They discovered that the near-periastron flare was asymmetric and that a much weaker near-apastron flare was also present. In later data, after the secular spin-up trend reversed, they found that the apastron flare became vanishingly small. Laycock, et al. (2003) folded GX 301–2 EOT data for the entire BATSE mission and found increasing flux levels consistent with orbital phase 0.5, that were about 10% of the peak near-periastron flux. For EXO 2030+375, Laycock, et al. (2003) found evidence for an increase in flux near apastron, averaging 30-40% of the peak flux in EOT data folded for TJD 8363-9540, prior to the change from spin-up to spin-down (Wilson et al. 2002). Direct comparison of folded BATSE and RXTE ASM light curves from TJD 10114-10724 suggested that the apastron emission is softer than the periastron emission in EXO 2030+375.

Two X-ray pulsars, discovered with BATSE, were initially located using EOT data in conjunction with pulsed measurements: GRO J1008–57 (Stollberg et al. 1993) and GRO J2058+42 (Wilson et al. 1995, 1998). GRO J1849–03 (Zhang et al. 1996a,b), which was later found to be identical with GS 1845-024 (Finger et al. 1999), was located using Earth occultation imaging (see also Appendix A).

3.4. Active Galaxies

Several AGN are sufficiently bright in hard x-rays to permit spectral and/or variability studies using BATSE Earth occultation data alone. In Fig. 10 we show intensity histories for four of the brightest AGN in the BATSE database. An extensive analysis of the Seyfert galaxy NGC 4151 by Parsons et al. (1998) covered six years of BATSE monitoring data. Paciesas et al. (1994) analyzed BATSE observations of the radio-loud quasar 3C273 during 1991-1993. Using BATSE data, Malizia et al. (2000) discovered hard x-ray emission from the high-redshift quasar 4C71.07 and presented evidence for long-term source variability. Dean et al. (2000) discussed BATSE observations of variability in 4C71.07 and two other blazars, Mrk 501 and PKS 2005-489. Wheaton et al. (1996) reported BATSE spectra of the nearby radio galaxy Cen A from 1991-1992 derived using the methodology developed by JPL (Skelton et al. 1994; Ling et al. 1996, 2000, see also Appendix C).

In several cases the BATSE data were useful in multi-wavelength studies of AGNs. BATSE observations were included in a radio to gamma-ray spectral analysis of 3C273 by (Lichti et al. 1995). Courvoisier et al. (1999) and Turler et al. (1999) investigated correlations of BATSE results on 3C273 with optical and infrared data during a six-year period. BATSE observations of the synchrotron component of the TeV blazar Mrk 501 during its 1997 high state were used in a multi-wavelength study by Petry et al. (2000).

Finally, the BATSE light curves were useful as context information for observations of AGNs by other instruments. Steinle et al. (1998) used the BATSE long-term history of Cen A to characterize the source state during COMPTEL observations in 1991-1995. Similarly, Haardt et al. (1998) used the BATSE light curve in interpreting *BepoSAX* observations of 3C273 in 1996-1997.

4. BATSE Deep Sample Results

A comprehensive deep sampling of the low-energy gamma-ray sky using the present formulation of the

EOT is predicated on the sensitivity curve in Fig. 1. The improvement in sensitivity over the HEAO 1 A-4 survey is only fully realized if systematic error can be minimized. In Harmon et al. (2002) we identified systematic errors in the application of the EOT to BATSE. Improvements to the detector response model, and multiple passes through the BATSE dataset with a better picture of the bright sources in the sky (Tables 2 and 3), have allowed us to reduce some contributors to systematic error. These results encouraged us to combine all the mission data together to achieve maximum sky exposure. Later in this section we incorporate a systematic error model in assessing the detection confidence of the sources in our sample. Limited applications of the approach we take here can be found in White et al. (1994) and Zhang et al. (1996a).

In Table 4, we present the 179 objects in the BATSE deep sample in order of increasing right ascension (α). Firm detections, which include the systematic error assessment described later, are indicated in boldface text. The columns from left to right are (1) the BATSE catalog name, (2) an alternate name recognized by the SIMBAD catalog if the BATSE name was not recognized, or other well-known name for the source, (3) identification of the type of source, if known, given the classes defined in Fig. 2. (4) An assigned category (A, B, C, N or I, see definitions below) based on the significance of detection after, and before (in parentheses) correction for systematic error and, (5-6) its celestial coordinates (α, δ) (J2000) and (7-8) Galactic coordinates (b, l). The next columns from left to right are the (9) detection significance for the 20-100 keV average photon flux averaged over the mission (9.1y) before (in parentheses) and after correction for systematic error ⁴, and finally, the flux in mCrab (columns 10-13) of

⁴To compute the 20-100 keV flux for sources for which we did not have the spectral fitting information given in Tables 2 and 3, we assumed a power law spectral shape with a photon index of -3, typical of accreting systems (an intermediate value between spectral slopes seen in black holes and those of softer sources such as pulsars). Because the computed 20-100 keV photon flux is sensitive to the assumed power law spectral shape, we only report significance.

each source in the four energy bands 20-40, 40-70, 70-160, and 160-430 keV. The Crab relative fluxes, we found, are the most accurate method of displaying flux information for the deep sample in the absence of precise spectral fitting information for each source.

It is helpful to classify the sources in our sample according to a scheme based on their significance of detection and variability, and taking into account the systematic effects present in our results. We use the following categorization:

A. (Definite detections) Persistent sources in category A have an average flux (9.1y) that exceeded a threshold of $0.01 \text{ photons cm}^{-2}\text{s}^{-1}$ in the 20-100 keV band. Transient sources in category A (denoted with a dagger (\dagger) in column (4)) exhibited at least one identifiable outburst with an average daily flux exceeding a threshold of $0.01 \text{ photons cm}^{-2}\text{s}^{-1}$ in the 20-100 keV band. Typical category A sources show variability on timescales of at least hours to a few days, have a readily identifiable period by FFT, or variability that correlates well with behavior in other wavelength bands. Because category A source identifications are independent of duty fraction, the detection significance can vary from a statistical zero over 9.1y for brief transients, to very high values for bright, persistent sources. 54 sources fall into category A: 21 accreting PSR, 29 BH or NS binaries, 1 SNR (the Crab Nebula), 3 AGN and no x-ray emitting stars.

B. (Definite detections) Sources with a 9.1y-average flux that exceeded 10σ , but with average flux $<0.01 \text{ photons cm}^{-2}\text{s}^{-1}$ in the 20-100 keV band. A periodicity search or epoch folding analysis may show a period associated with the source. After correction for systematic error, 29 sources fall into category B: 6 accreting PSR, 18 BH or NS binaries, 2 SNR, 3 AGN and no x-ray emitting stars. In later sections, we test the category B sources in several ways for consistency of detection.

C. (Possible detections) Sources with a 9.1y-average flux (20-100 keV) with a significance $\geq 3\sigma$ and $<10\sigma$. Variability was not investigated; thus, transient activity was not considered and could be present in the BATSE dataset. After correction for system-

atic error, 36 sources fall into category C: 6 accreting PSR, 16 BH or NS binaries, 4 SNR, 1 SGR, 5 AGN and 4 x-ray emitting stars.

N. (Non-detections) Sources with a 9.1y-average flux (20-100 keV) of significance between $\pm 3\sigma$. Transient activity from the sources was not considered, and could be present in the BATSE dataset. After correction of systematic error, 45 sources fall into category N: 7 accreting PSR, 21 BH or NS binaries, 2 SNR, 2 SGRs, 4 isolated PSR, 1 AGN and 8 x-ray emitting stars.

I. (Indeterminate) Sources with a 9.1y-average flux (20-100 keV) of significance $<-3\sigma$, indicating confusion with nearby sources, or a poorly characterized systematic error in the surrounding sky region. The category I sources represented, for the most part, our inability to separate crowded source regions where bright sources known to OF_W were close by. Transient activity from category I sources was not considered and could be present in the BATSE dataset. After correction of systematic error, 15 sources fall into category I: 1 accreting PSR, 13 binary BH or NS, 1 SGR, and no SNR, isolated PSR, AGN, or x-ray emitting stars. Since these sources were indeterminate, we do not report 4-band fluxes for these in Table 4.

4.1. Determination of Systematic Errors Due to Sky Location

In addition to the set of 179 known sources, we produced light curves for a grid of 162 test or control “source” locations over the entire mission. The grid covers the entire Galactic plane, with the highest density of test locations in the central bulge region, as shown in Fig. 11. The grid has points every 3° along the plane between -60° and $+60^\circ$ longitude with two sets of grid points of the same spacing at $+6$ and -6° latitude. Beyond $\pm 60^\circ$ longitude, there are grid points at 6° spacing and 0° latitude. The grid light curves were subjected to the same flagging process for outliers as performed for the known source set. Deconvolution of the detector response for the grid points was performed using an assumed power law

of the spectrum with a photon index of -3. Ideally, with no systematic error (a perfect sky model) there should be no residual flux. However, a few points fall very close (less than a degree) to known bright sources, which is desirable, as it allows a more accurate assessment of systematic error due to the effects of finite spatial resolution. On the other hand, some grid points may fall very close to unknown sources that are not in our bright source model.

In Fig. 12, we show the average fluxes for the 9.1y-long light curves at each grid point as a function of Galactic longitude. The samples at -6° , 0° , 6° latitude are shown together for longitudes between -60° and 60° . We also show the standard deviation (in sigmas) for the one-day flux averages⁵. Average values (absolute) for the fluxes are approximately $0.0015 \text{ photons cm}^{-2}\text{s}^{-1}$ ($\sim 5 \text{ mCrab}$), with the exception of outliers near the Galactic center and points such as (l, b) of $(-24, 0)$, $(42, 0)$. We found no global trend in longitude or latitude, but there clearly were regions where known bright sources are concentrated, or unknown point source emission has not been well-characterized in our bright source model. Artifacts due to subtraction of point source fluxes can be manifest either as positive or negative measurements in the grid (Harmon et al. 2002), which are allowed by the fitting method. In specific cases we have found that simultaneous fits made to weak sources or empty fields with nearby bright sources can sometimes generate significantly negative measurements. Unknown sources could also produce negative residuals, but their actual effect is not separable from the subtraction of known sources.

We found that some of the positive grid outliers mentioned above fall near sources not known in iteration 2 but revealed very significant flux over at 9.1y average: 4U 1907+097, Cir X-1 and H 1624-490. Source confusion in the Galactic center region (GCR), as expected, also showed a large residual flux from unresolved point source emission. It was not possible to attribute the excess GCR flux to specific sources. We treat the GCR sources, along with

⁵An earlier version of this figure, including the first $\sim 7\text{y}$ of data, appears in Harmon et al. (2002).

the full source set, using a model for systematic error obtained from the grid analysis. However extra care should be used in interpreting fluxes from weak sources (category B and below) in the few degrees ($2\text{--}4^\circ$) surrounding this region. There are deep images of the GCR with *Granat*/Sigma (Paul et al. 1991), for example, that are better suited for determining the average emission characteristics of these sources. A similar situation is likely to exist for the Magellanic Cloud regions, which have not been evaluated extensively using BATSE data.

The second moments, or standard deviations had a completely different behavior. Unlike the average fluxes, standard deviations were a relatively smooth function of sky location. These are plotted in Fig. 12 in units of Gaussian statistical error for the average daily fluxes, i.e., a value of 1 in Fig. 12 means there was no contribution from any source of error except Poisson statistics (which, of course, is never the case!). The standard deviations were clearly broader than predicted for a Gaussian distribution about zero flux due to systematic errors ($1\sigma = \sim 0.01$ photons $\text{cm}^{-2}\text{s}^{-1}$). We found broadening factors of about 20% (between 70° and 180° longitude and peaking near a factor of 2 at about -105°) in excess of normal statistics. The standard deviations were largest near bright, variable sources such as Vela X-1 ($l=-96.9^\circ$) and Cygnus X-1 ($l=71.3^\circ$). These effects are caused by well-known properties of the two sources: the long period pulses from Vela X-1, and shot noise from Cyg X-1.

4.2. Application of the Systematic Error Model

Correction factors for the flux average (additive) and flux average error (multiplicative) for the 179-source set were derived as follows: Using the flux and standard deviation for the 162-point grid, we interpolated correction factors both for the flux and its associated error corresponding to the locations of the known 179 source set from the results shown in Fig. 12. If the known source was within Galactic longitudes of -60° (300°) and $+60^\circ$ longitude and within

$\pm 6^\circ$ latitude, we applied an interpolation based on the four nearest neighbors on the grid. Outside of the bulge region, -60° longitude and $+60^\circ$ longitude, we applied a two-point interpolation of the nearest neighbors on the grid. For any point sources less than $\pm 60^\circ$ longitude, and latitudes between 6° and 10° and between -6° and -10° , we also applied a two-point interpolation. Outside of these regions, well above and removed from the Galactic plane, there was no correction to the flux average, and a 1.4 multiplicative factor was applied to the average error. This value is a conservative estimate based on the observed standard deviations in Fig. 12.

The detection significance and relative fluxes in Table 4, corrected for systematic error, were then calculated as

$$\Pi_{cor} = \frac{F - F_{cor}}{\epsilon_{cor}\delta F} \quad (1)$$

where Π_{cor} is the corrected significance in column 9, and F_{cor} and ϵ_{cor} are the interpolated correction factors derived from the grid analysis, for the 20-100 keV flux (F) and error (δF), respectively, and

$$B_{i,cor} = B_i - \frac{F_{cor}}{F} B_i \quad (2)$$

where the $B_{i,cor}$ are the corrected Crab relative rates in columns 10-13. The statistical errors for the relative rates were also multiplied by the ϵ_{cor} .

In Fig. 13, we show the distribution of the 9.1 yr, 20-100 keV flux averages in order of brightness, beginning with the brightest persistent source, the Crab Nebula. The curve has been computed with and without systematic corrections. We also show the assigned category, as determined after the corrections were applied. We note that transients, and especially those with low duty fractions, may have an average flux that is much less than the peak flux, and can appear anywhere on the curve. Of the 179 sources, about 110-120 sources were above the 3σ flux limit. This agrees well with the combined number of sources (119) in categories A through C. Note that category N sources with a slightly negative, non-significant flux, and all of the category I sources, whose fluxes are $< -3\sigma$ negative, are not visible in the log plot. The main

effect of the systematic corrections is to smooth the trend of the lower part of the intensity curve, which shows a rollover at the low flux end. The physical interpretation of the rollover is that we are no longer able to distinguish significantly measurable flux due to systematic and statistical effects at low source intensity. We are also prone to missing sources in our biased sample such as transients or persistent sources with fluxes comparable to those in category C.

There is a possibility that the rollover of the intensity curve reflects the true Galactic distribution of sources. The depth of our sample in flux is significantly beyond the ~ 70 sources detected in the HEAO 1 A-4 survey (Levine et al. 1984), even with BATSE’s higher energy threshold. For example, HMXBs and LMXBs are thought, respectively, to be formed in binaries with population I and II progenitor stars, and thus have sharply differing Galactic distributions (Grimm, Gilfanov, & Sunyaev 2002). However, to extrapolate information about source populations in our data is difficult due to the missing sources and the relatively small size of the sample. A deep, unbiased survey with an instrument such as EXIST, with excellent background rejection and spatial resolution characteristics, could produce a much more precisely determined extension and shape for the curve shown in Fig. 13.

4.3. Consistency of Deep Sample Detections

Before concluding this work, it is interesting to look at the robustness and consistency of the reported detections in Table 4 without going into great detail. To do this, we examined sources at flux levels close to the sensitivity limit of the EOT, i.e., just above the level where systematic effects dominate.

We saw from the grid analysis that there were positive as well as negative flux offsets at the measured control locations, as well as a few significant outliers. Ideally, interpolation of the offsets should allow us to estimate systematic errors in the point source set. However, we have noted some shortcomings of the approach: there are category I sources remaining after the model was applied. Another im-

perfection is that there are cases where a reasonably bright source is omitted from our model (Tables 2 and 3), and we may erroneously subtract “real” flux from the statistically-derived average.

From the analysis of the grid outliers and in the results of Table 4, we found that the HMXB PSR 4U 1907+097 (Chitnis et al. 1993), and the LMXBs Cir X-1 (Iaria et al. 2001) and H 1624-490 (Balucinska-Church et al. 2000) have a raw significance in the 20-100 keV band sufficient to be considered as category B, but in failing to identify these sources as bright sources, they fall into categories C, C, and N, respectively, after an overestimated correction. We also found reasonable agreement between our uncorrected fluxes (i.e., before systematic error corrections were made) and the observed low-energy gamma-ray fluxes from the literature for these sources. The burster 1E 1724-307 of the Terzan 2 globular cluster is another example; 1E 1724-307 was the only category A source found in the deep sample. 1E 1724-307 has rather strong and variable hard X-ray emission (~ 30 mCrab) (Barret & Vedrenne 1994, see also Fig. 8) in the 20-100 keV band, and was not considered a bright source in the current pass through the data. We did not alter the systematic corrections to the flux for the four sources in the catalog, but it is likely, pending other tests, that these sources should be included in the bright source model for a future pass through the dataset.

Next we rigorously examined the category B subset of sources, a total of 29 objects, which we claimed are definite detections. These sources are gathered for inspection in Table 5. The (model-dependent) average fluxes (9.1y) in the 20-100 keV band are between 1.2 and 9.6×10^{-3} photons $\text{cm}^{-2}\text{s}^{-1}$, with detection significances, including systematic error, varying between 10 and 52σ . Unlike Table 4, we list both the uncorrected average flux and error, and the interpolated systematic correction based on the source location with respect to the Galactic plane.

Eighteen of the 29 sources were within 10° of the Galactic plane and thus had corrections to the given flux average and error. Correction factors to the average flux for the category B sources ranged

as high as 150% in the GCR. As indicated in Eq. (2), if $F_{cor} > 0$, it was subtracted from the statistical average. If $F_{cor} < 0$, it was added to the statistical average. As can be seen in column 4 of Table 4, the net effect of the systematic error corrections for the deep sample was to render a number of category B and C sources as a lower category, and some of the category I sources as category N. Of the 29 sources in category B, 27 did not require recategorization after systematic corrections were applied.

On the other hand, there were a few cases where addition of a large correction factor to the average flux of a category C or N (non-detection) source resulted in a total corrected flux level and significance equivalent to a category B source. Two of these appear in Table 5: 4U 1820-303, a category B(C) source, and 4U 1916-053, a category B(N) source. A previous survey for hard X-ray emission in the BATSE database (Bloser et al. 1996) reported 2σ upper limits of 30 mCrab for both 4U 1820-303 and 4U 1916-053 in the 20-100 keV band using 10 days of data. Since that time, Bloser et al. (2000a,b) followed up the BATSE results with observations of both 4U 1820-303 and 4U 1916-053 with RXTE, as did Church et al. (1998) using *BeppoSax*. Hard tails were observed in both sources. In our deep sample, we report a 20-40 keV flux over 9.1y in Table 5 from 4U 1820-303 of 11 ± 0.8 mCrab (uncorrected) in the 20-40 keV band, and a corrected flux of 23 ± 1.1 mCrab. The corrected flux is a reasonable factor of 4-5 lower than a recent RXTE measurement of the hard X-ray flux by Bloser et al. (2000b). 4U 1916-053 showed no significant detection (0.9 ± 0.7 mCrab) (uncorrected) in the 20-40 keV band, but a corrected flux of 38 ± 1.0 mCrab, reasonably close to the RXTE and *BeppoSax* results, but about a factor of 2 higher. Since it is unlikely that the source spends most of the time at flux levels more than that observed in the pointed observations, this suggests that the magnitude of the systematic correction for 4U 1916-053 is over-estimated. The sign of F_{cor} , i.e., the sense of the correction, though, to render a significant positive measurement, is correct. Of course, without specific knowledge of variability of the hard tails in these objects, it is not possible to make a definitive conclusion, but it is possible that

rather large systematic error corrections could be suspect in our model. This is not too surprising, since we are under sampling a rather complex and rapidly changing residual flux as a function of sky location as shown in the top frame of Fig 12. We are also correcting the 4-band fluxes, which span the energy range between 20 and 430 keV, with a correction deduced for the 20-100 keV band.

To investigate the impact of the correction factors more generally, we computed the relative change in significance for all sources in our sample before and after the correction was applied. This is shown as a histogram in Fig. 14. The distribution is dominated by the simple multiplicative correction of the second moment (centered at -0.3), but in cases where the uncorrected, statistically-derived flux was very small relative to the systematic correction to the flux, F_{cor}/F in Eq. (2) was consequently very large. These are represented by the outlying wings of the histogram. We therefore made symmetric cuts on the distribution of fractional changes in significance about the median value at -1.05 on the low end of the distribution and 0.45 on the high end in Fig. 14. 24 of the 179 sources had a fractional change in significance that fell outside of the vertical dashed lines. We also found that the absolute value of the significance was increased by application of the systematic error correction for 16 of the 24 sources beyond the cuts, whereas for most sources, the significance was reduced. We therefore decided it was better to quote the uncorrected relative Crab rates in the four bands for these 24 sources in Table 4, including the two category B sources discussed above. The 4-band fluxes with no systematic corrections to the statistically-derived fluxes are denoted by the four band rates in parenthesis. The judgment here is that the uncorrected 4-band fluxes for these objects are closer to the true 9.1y averages.

In the following sections we illustrate the robustness of the category B source detections using periodicity searches and Earth occultation imaging. It is important to establish the reliability of the EOT method at these low flux levels. For example, detection of the black hole candidate LS 5039 (McSwain et al. 2001) in the low-energy gamma-ray band has

not been reported previously in the literature, and 4U 1812-12, was reported only for the first time in Barret, Olive, & Oosterbroek (2003).

4.4. Periodicity Search of Light Curves

X-ray binaries sometimes exhibit periodic or quasi-periodic intensity changes, and in most cases, the observed periods correspond to the orbital period of the binary (P_{orb}). Super-orbital periods (P_{long}) also have been observed in accreting neutron star systems, and have been attributed to disk precession (Wijers & Pringle 1999), and/or periodic reversals of the spin direction (Bildsten et al. 1997). Laycock, et al. (2003) have investigated periodic behavior in HMXBs in the BATSE EOT database. Here we use the identification of a period or quasi-period in the category B sources to add confidence to the detection of the fluxes presented in Table 5.

Searches for periodic behavior in unevenly sampled data from the EOT are accomplished using the Lomb-Scargle algorithm for Fourier transforms (Scargle 1982; Horne & Baliunas 1986), and epoch folding techniques in specific cases. We first performed Fourier transforms to create power density spectra (PDS) of the 9.1-year one-day average light curves to search for periods in the flux variations from all sources.

The PDS were scanned in the frequency range between 0.002 d^{-1} (500 days, 6.6 cycles) and 0.5 d^{-1} (the Nyquist frequency of evenly sampled data). A simple threshold for reporting of a peak was set at a significance, or false alarm probability (FAP) (Press et al. 1992), of 0.01 (FAP=1 is roughly the level of Poisson noise) for the Lomb periodogram. The FAP is related to the PDS peak power z (Press et al. 1992) as

$$FAP(z) = 1 - (1 - e^{-z})^M \quad (3)$$

or if the probability is $\ll 1$, $FAP(z) \approx M e^{-z}$. M is the number of independent frequencies and is related to the total number of flux values N as

$$M = N \frac{\kappa \eta}{2} \quad (4)$$

The oversampling factor η was set at a value of 4, and the maximum (high end) frequency κ for the PDS was set at 2, so that $M=4N$. It should be noted that the FAP is strictly a meaningful quantity for a PDS of Gaussian distributed data that is normalized by the variance of the dataset. As we have shown earlier for EOT light curves, the second assumption is clearly violated. Thus the FAPs should only be taken as an indication of relative significance.

In Table 6 we list the search results from the PDS analysis of the category A and B sources. We limited ourselves to peaks in the PDS that corresponded to orbital and super-orbital periods found in the literature. The far column indicates the FAP computed for the power at the peak frequency. It can be seen that the FAP ranges from relative large values ~ 0.01 (closer to the Poisson noise level but very significant) to very small values for persistent, eclipsing category A sources such as Cen X-3, Vela X-1, OAO 1657-415, and 4U 1700-377 (see also Fig. 5), as well as some of the sources with superperiods such as LMC X-4 and HER X-1. The reported uncertainty in the centroid frequency is an approximate error based on the oversampling factor and not a formally derived error. The quoted error can be reduced by proper fitting of the PDS and subtraction of the sinusoidal signal from the light curve, and the variance recomputed (Horne & Baliunas 1986). Since we are interested only in confirming detections of the category B sources, this analysis was not performed.

The only category B sources with detected periods using FFTs were SMC X-1, LMC X-4, and 4U 1538-522. All are eclipsing HMXBs. Both SMC X-1 (Wojdowski et al. 1998) and LMC X-4 Laycock, et al. (2003) were previously known to show orbital and superorbital-related variations in the BATSE data. 4U 1538-522 was already detected by BATSE via its pulsed emission Bildsten et al. (1997), but this is the first reported EOT detection of its orbital period of 3.728d.

The FFT analysis was performed only on the 1-day resolution light curves with a simple cutoff for the FAP and is complicated by low frequency noise, CGRO orbital precession, and other effects. For ex-

ample, Laycock, et al. (2003) reported a marginal result for the orbital period of the HMXB pulsar 4U 1907+097 (8.3745d), a category C(B) source, that did not show up in the PDS search. Since only a few category B sources were detected in the PDS, we carried out epoch folding of the single step (twice per CGRO orbit sampling) light curves of at known periods for selected category B sources.

In Fig 15(a), we show 9.1y single step light curves of the three category B sources folded at the P_{orb} given in column 2 of Table 6 and the light curve of 4U 1907+097 folded at 8.3745d. In Fig 15(b), we show single step folded light curves for sources with the reported super-orbital periods in column 3 of Table 6. 4U 1538-522, LMC X-4, and SMC X-1 all exhibit sharp eclipse profiles, as well as prominent super-orbital variations for the latter two sources. We also epoch-folded single step 4-band rates searching for reported periods from soft X-ray and optical measurements among several of the remaining category B sources (some perhaps binary-orbit related) in X Per (250d, Delgado-Marti 2001), 1E 1145-614 (14.335d, Ray & Chakrabarty 2001), GX 349+2 (21.7h, Wachter 1997), GX 354+0 (63d, 72d, and 78d, Kong, Charles, & Kuulkers 1998), 4U 1820-303 (171d, Chou & Grindlay 2001), LS 5039 (4.117d, McSwain et al. 2001), SS 433 (\sim 13d, binary period, 65d, jet nodding, \sim 164d, jet precession, Eikenberry et al. 2001), 4U 1916-053 (199d, Bloser et al. 2000b), 4U 2127+119 (17.112h, Illovaisky et al. 1993) and Cyg X-2 (9.84, 40.4, 53.7, 61.3, and 68.8d, Paul, Kitamoto, & Makino 2000). Among these 10 sources, no convincing periodicities were seen in the epoch folded light curves. Given that the average fluxes of the HMXB eclipsers 4U 1538-522, LMC X-4, and SMC X-1 are comparable to the other category B sources in Table 5, it is somewhat surprising that other binaries, which have reported periods in X-rays, did not show recognizable periodic variations in the epoch folded light curves.

We point out that several of the category B LMXBs are high inclination, compact, ultra-short period binaries known as “dippers”. These close binaries have orbital periods of only minutes to hours. The actual dips and/or eclipses are very short, \sim few

minutes, and are observed as absorption-induced changes in the soft X-ray flux (\sim keV) (Church et al. 1998). Such short duration absorption dips are not accessible using the BATSE EOT; however, the reported superorbital periods are easily within the timescales accessible for epoch folding, yet none were seen. More work should be done with these sources, but the apparent lack of periodicity in the LMXBs (6 out of 6) is interesting. Assuming the reported X-ray and optical modulations are predominantly associated with disk precession as in the HMXBs, such effects do not appear to modulate the intensity of the observed gamma-ray flux in our category B LMXBs.

4.5. Earth Occultation Imaging of Category B Sources

Due to the limited success of the periodicity searches in the category B light curves, we employed Earth occultation imaging to localize the gamma-ray flux from these sources. The occultation imaging technique (Zhang et al. 1993) allows the construction of a 2-D image of a region of the sky to an accuracy of $1\text{-}2^\circ$ and has been used to identify new transients where the source location was previously unknown (e.g., GRO J1655-40, Zhang et al. 1994). For more details of the method, see Harmon et al. (2002) and references therein.

Most of the 29 category B sources of the EOT catalog are strong enough that we might expect to detect them in a 15-day integration ($\sim 6.5\sigma$ for a 25 mCrab source in the 20-100 keV band). A non-detection, however, does not imply that the EOT signal does not come from this source, because the application and interpretation of the imaging technique is complex and depends on more than the strength of the source signal and spectral signature.

Each of the category B sources was examined over at least one time interval to look for an excess in the image at the source location. A suitable limb geometry was chosen by displaying the rising and setting limbs over an entire CGRO precession period. This period will contain all possible limb geometries for a given source and allow the selection

of the longest consecutive time interval with near-orthogonal rising and setting limbs for the best possible spatial resolution. Images were generated for ten separate source locations within a 10° by 10° field of view. The technique is most efficient for imaging sources in the center of the field, but a true signal should appear when the source is offset from the center. Offsets up to 1° in each direction were considered and images were produced for LAD energy channels 1 through 3.

Although most of the category B sources exhibited at least some variability, the only flux-related selection of integration time intervals was made for those sources that are eclipsing binary systems or systems with a superorbital period. The RXTE ASM light curves (http://xte.mit.edu/ASM_lc.html) allowed the selection of time periods when the X-ray emitter was not eclipsed by its companion and was not occulted by a warped accretion disk in those systems with a known superorbital period.

Table 7 summarizes the imaging results. 22 of the 29 category B sources yielded at least one credible image. The difficulty in obtaining a good limb geometry is apparent in some of the sources where the contours appear elongated. In others, the noisiness of the sky was responsible for the lack of image contours associated with the category B source. Figures 16(a-d) show some of the noteworthy images for the different types of astrophysical objects seen by BATSE. The AGN 3C 273 has a spectrum hard enough to be imaged in the 100-300 keV energy range as seen in Fig 16(a). Figures 16(c) and 16(d) are both taken in the 50-100 keV energy range and show good source-centered images of the supernova remnant PSR 1508-59 and the X-ray binary EXO 0748-676 respectively. Some source images suffer from source confusion. In particular 4U 1702-429 and 4U 1705-440 (the latter a strong low-energy gamma-ray source in its hard state (Barret & Olive 2002)) are close to both each other and to the category A source OAO 1657-415 but separate contours delineate the sources in at least some of the grid positions. Another case is that of 4U 1812-12, which is close to GX 17+2, a category A source, but has a much harder spectrum. Even when it is offset from the center of the image, the

contours may encompass both sources in channel 1, but GX 17+2 drops out in channel 2 and the contours tighten around 4U 1812-12. Although these cases show poorly resolved contours, the spatial resolution is sufficient to support the reported detections of these sources. The ambiguity often disappears when the source of interest is in the center of the field-of-view, as can be seen in Fig 16(b) where the flux from 4U1812-12 (also called Ser X-2) swamps that from GX 17+2 even in the 20-50 keV range.

5. Use of the Deep Sample Results

The BATSE EOT deep sample has interesting implications for future studies. The deep sample can serve as a guide/comparison tool to an unbiased survey with other instruments such as INTEGRAL (Winkler 2001) and *Swift* (Barthelmy 2000). There also remains the possibility of an unbiased survey with BATSE (Shaw et al. 2001, 2003). This catalog serves as a first critical analysis of the entire BASTE dataset, and these results are made available on the world wide web for potential applications, some perhaps unforeseen.

The spectral information from BATSE were largely unexplored in this work. For example, it was not practical for us to present an analysis of the long-term spectra in the full 16 channel data that are available. However, we made limited comparisons of our 4-band results to those of the HEAO 1 survey Levine et al. (1984), long-term flux averages (~ 5 yrs) of the RXTE ASM compiled by Grimm, Gilfanov, & Sunyaev (2002), and to pointed instrument observations for AGNs and LMXB neutron stars from the *BeppoSAX* and RXTE. This can be done using the conversion factors given in Table A3, and the Crab Nebula, which averages about 75 c/s in the 2-12 keV ASM band. Allowing for the differing observation intervals involved, we find that our 4-band relative rates compare well in cross-checks with these results. This suggests that the BATSE data could be used at a next level to obtain duty fractions for these sources in various energy bands.

We find from the category B analysis that some

types of sources such as supernova remnants and AGNs show hard photon emission even into the 160–430 keV band as shown in Table 5. Accreting pulsars, in contrast, have relatively hard spectra near the BATSE threshold and sharp spectral cutoffs at higher energy consistent with our understanding of their emission mechanisms. Across the ASM (2–12 keV) and BATSE (20–40 keV) bands, the fluxes reported for the accreting pulsars are within a few σ agreement for the two instruments. The high duty fraction LMXB neutron stars with hard X-ray emission from pointed-instrument observations (Barret et al. 2000) have fluxes that are also comparable with the averages given in Table 5.

We caution users not to over interpret some results, such as the sources in category C considered as possible detections. Some could indeed be real detections, but represent the limits of the sensitivity of the current version of the BATSE EOT, and the fluxes are dominated by the systematic corrections. For example, a few X-ray stars (White et al. 1994, see also) appear in this category (none appeared in categories A or B and most are in category N), but the fluxes are too weak for testing with the methods employed in Sec. 4. We stress that the category C results definitely can suffer from source confusion and other systematic errors that could easily produce the low-level observed fluxes. As is, the 4-band relative rates in Table 4 for the category C and N sources should be used only to derive upper limits on the 9.1 γ averages.

This research has made use of the SIMBAD database, operated at CDS, Strasbourg, France. This work was supported by the Goddard Space Flight Center Compton Gamma Ray Observatory Science Support Center, which is funded by the NASA Office of Space Science. We also acknowledge the availability of RXTE ASM data courtesy of the RXTE Science Support Center. The authors thank students Patrick Pecot (Georgia Tech), Lindsay Waite (Vanderbilt), and Peter Fimognari (University of Alabama in Huntsville), for assistance with spectral analyses and period searches.

REFERENCES

Arnaud, K. A. 1996, in ASP Conf. Ser. 101, Astronomical Data Analysis Software and Systems V, ed. G. H. Jacoby & J. Barnes (San Francisco, CA: ASP), 17

Balucinska-Church, M., Humphrey, P. J., Church, M. J., & Parmar, A. N. 2000, A&A, 360, 583

Barret, D., & Vedrenne, G. 1994, ApJS, 92, 505

Barret, D., et al. 1996, A&AS, 120, no. 4, 121

Barret, D., Olive, J. F., Boirin, L., Done, C., Skinner, G. K., & Grindlay, J. E. 2000, ApJ, 533, 329

Barret, D. 2001, Adv. Space Res., 28, no. 2-3, 307

Barret, D., & Olive, J. F. 2002, ApJ, 576, 391

Barret, D., Olive, J. F., & Oosterbroek 2003, A&A, 400, 643

Barthelmy, S. D. 2000, Proc. SPIE 4140, 50

Bassani, L., Caroli, E., Di Cocco, G., Malaguti, G., Stephen, J. B., Malizia, A., Westmore, M. J., & Dean, A. J. 2000, in AIP Conf. Proc. 510, The Fifth Compton Symposium, ed. M. L. McConnell & J. M. Ryan (Melville, NY: AIP), 447

Bildsten, L. et al. 1997, ApJS, 113, 367

Bloser, P. F., et al. 1996, A&AS, 120, no. 4, 275

Bloser, P. F., Grindlay, J. E., Barret, D., & Boirin, L. 2000a, ApJ, 542, 989

Bloser, P. F., Grindlay, J. E., Kaaret, P., Zhang, W., Smale, A. P., & Barret, D. 2000b, ApJ, 542, 1000

Bradt, H. V., Rothschild, R. E., & Swank, J. H. 1993, A&AS, 97, 355

Bradt, H. V., Levine, A. M., Remillard, R. A., & Smith D. M. 2000, in Rossi2000: Astrophysics with the Rossi X-ray Timing Explorer (GSFC: Greenbelt), E114

Brandt, S., Lund, N., & Rao, A. R. 1990, *Adv. Space Res.*, 10, no. 2, 239

Brandt, S. 1994, Ph.D. Thesis, Copenhagen University Observatory

Briggs, M. S. 1995, in *AIP Conf. Proc.* 384, Gamma-Ray Bursts, Third Huntsville Symposium, ed. C. Kouveliotou, M. S. Briggs, & G. J. Fishman (Woodbury, NY: AIP), 133

Brocksopp, C., Tarasov, A. E., Lyuty, V. M., & Roche, P. 1999a, *A&A* 343, 861

Brocksopp, C., Fender, R. P., Larionov, V., Lyuty, V. M., Tarasov, A. E., Pooley, G. G., Paciesas, W. S., & Roche, P. 1999b, *MNRAS*, 309, 1063

Callanan, P. J., et al. 1995, *ApJ*, 441, 786

Castro-Tirado, A. J. 1994, Ph.D. Thesis, University of Copenhagen

Chitnis, V. R., Rao, A. R., Agrawal, P. C., & Manchanda, R. K. 1993, *A&A*, 268, 609

Chou, Y., & Grindlay, J. E. 2001, *ApJ*, 563, 934

Church, M. J., Parmar, A. N., Balucinska-Church, M., Oosterbroek, T., Dal Fiume, D., & Orlan-dini, M. 1998, *A&A*, 338, 556

Claret, A., et al. 1994, *ApJ*, 423, 436

Clarkson, W. I., Charles, P. A., Coe, M. J., Laycock, S., Tout, M. D., & Wilson, C. A. 2003, *MNRAS*, 339, 447

Connaughton, V., Robinson, C. R., McCollough, M. L., & Laurent-Muehleisen, S. 1999, in *ASP Conf. Ser.* 159, BL Lac Phenomenon, ed. L. O. Takalo & A. Sillanpaa (San Francisco: ASP), 209

Conner, J. P., Evans, W. D., & Belian, R. D. 1969, *ApJ*, 157, L157

Corbel, S., Kaaret, P., Jain, R. K., Bailyn, C. D., et al. 2001, *ApJ*, 554, 43

Courvoisier, T. J.-L., Paltani, S., Turler, M., Walter, R., & Cremonesi, I. D. 1999, *Astrophys. Lett. & Comm.*, 39, 49

D'Amico, F., Heindl, W. A., Rothschild, R. E., & Gruber, D. E. 2001, *ApJ*, 547, L147

Dean, A. J., Malizia, A., Westmore, M. J., Gurriaran, R., Lei, F., Bassani, L., & Stephen, J. B. 2000, in *AIP Conf. Proc.* 510, The Fifth Compton Symposium, ed. M. L. McConnell & J. M. Ryan (Melville, NY: AIP), 342

Delgado-Marti, H., Levine, A. M., Pfahl, E., & Rappaport, S. A. 2001, *ApJ*, 546, 455

Di Salvo, T., Stella, L., Robba, N. R., van der Klis, M., Burderi, L., et al. 2000, *ApJ*, 544, L119

Di Salvo, T., Mendez, M., van der Klis, M., Ford, E., & Robba, N. R. 2001, *ApJ*, 546, 1107

Eikenberry, S. S., Cameron, P. B., Fierce, B. W., Kull, D. M., Dror, D. H., Houck, J. R., & Margon, B. 2001, *ApJ*, 561, 1027

Esin, A. A., Narayan, R., Cui, W., Grove, E. J., & Zhang, S. N. 1998, *ApJ*, 505, 854

Fender, R. P., et al. 1999, *ApJ*, 519, L165

Finger, M. H., Koh, D. T., Nelson, R. W., Prince, T. A., Vaughan, B. A., & Wilson, R. B. 1996, *Nature*, 381, 291

Finger, M. H., Wilson, R. B., & Harmon, B. A. 1996b, *ApJ*, 459, 288

Finger, M. H., Bildsten, L., Chakrabarty, D., Prince, T. A., Scott, D. M., Wilson, C. A., Wilson, R. B., & Zhang, S. N. 1999, *ApJ*, 517, 449

Fishman, G. J., Meegan, C. A., Parnell, T. A., Wilson, R. B., & Paciesas, W. S. 1984, in *AIP Conf. Proc.* 115, High Energy Transients in Astrophysics, ed. S. E. Woosley (New York: AIP), 651

Fishman, G. J. et al. 1989a, in *Proc. of the Gamma Ray Observatory Science Workshop*, Goddard Sp. Flt. Ctr., Greenbelt, MD, ed. W. N. Johnson, (informally published), 2-39

Fishman, G. J. et al. 1989b, in *Proc. of the Gamma Ray Observatory Science Workshop*, Goddard

Sp. Flt. Ctr., Greenbelt, MD, ed. W. N. Johnson, (informally published), 3-47

Fishman, G. J., & Meegan, C. A. 1995, *ARA&A*, 33, 415

Fishman, G. J., Kouveliotou, C., van Paradijs, J., Harmon, B. A., Paciesas, W. S., Briggs, M. S., Kommers, J., & Lewin, W. H. G. 1995, *IAU Circ.* 6272

Ford, E., Kaaret, P., Harmon, B. A., Tavani, M., & Zhang, S. N. 1996, *ApJ*, 467, 272

Ford, E. C., et al. 1997, *ApJ*, 486, L47

Foster, R. S., Waltman, E. B., Tavani, M., Harmon B. A., Zhang, S. N., Paciesas, W. S., & Ghigo, F. D. 1996, *ApJ*, 467, L81

Gehrels, N., & Shrader, C. R. 1997, in *X-Ray Imaging and Spectroscopy of Cosmic Hot Plasmas*, Proc. of an International Symp. on X-Ray Astronomy, Tokyo, ed. F. Makino & K. Mitsuda, 593

Greiner, J., Dennerl, K., & Predehl, P. 1996, *A&A*, 314, L21

Grimm, H.-J., Gilfanov, M., & Sunyaev, R. 2002, *A&A*, 391, 923

Grindlay, J., Garcia, M., & Zhao, P. 1994, *IAU Circ.* 6096

Grindlay, J. E., Barret, D., Bloser, P. F., Zhang, S. N., Fishman, G. J., Harmon, B. A., & Paciesas, W. S. 1996, *A&AS*, 120, no. 4, 145

Grindlay, J., et al. 2001, in *AIP Conf. Proc.* 587, *Gamma 2001: Gamma-Ray Astrophysics 2001*, ed. S. Ritz, N. Gehrels, & C. R. Shrader (Melville, NY: AIP), 899

Grindlay, J., & EXIST Science Working Group, 2003, *BAAS*, 35, 654

Haardt, F., et al. 1998, *A&A*, 340, 35

Harmon, B. A., Zhang, S. N., Fishman, G. J., & Wilson, C. A. 1993, *IAU Circ.* 5890

Harmon, B. A., et al. 1994, *ApJ*, 425, L17

Harmon, B. A. et al. 1995, *Nature*, 374, 703

Harmon, B. A., Wilson, C. A., Tavani, M., Zhang, S. N., Rubin, B. C., Paciesas, W. S., Ford, E. C., & Kaaret, P. 1996, *A&AS*, 120, no. 4, 197

Harmon, B. A., Deal, K. J., Paciesas, W. S., Zhang, S. N., Robinson, C. R., Gerard, E., Rodriguez, L. F., & Mirabel, F. 1997, *ApJ*, 477, L85

Harmon, B. A., et al. 2002, *ApJS*, 138, 149

Hernanz, M., Smith, D. M., Fishman, G. J., Harmon, B. A., Gomez-Gomar, J., Jose, J., Isern, J., & Jean, P. 2000, in *AIP Conf. Proc.* 510, *The Fifth Compton Symposium*, ed. M. L. McConnell & J. M. Ryan (Melville, NY: AIP), 82

Hjellming, R. M., & Rupen, M. P. 1995, *Nature*, 375, 464

Holt, S. S. 1976, *Ap&SS*, 42, 123

Horne, J. H., & Baliunas, S. L. 1986, *ApJ*, 302, 757

Iaria, R. Burderi, L., DiSalvo, T., La Barbera, A., & Robba, N. R. 2001, *ApJ*, 547, 412

Ilovaisky, S. A., Auriere, M., Koch-Miramond, L., Chevalier, C., Cordini, J.-P., & Crowe, R. A. 1993, *A&A*, 270, 139

Jager, R., et al. 1997, *A&AS*, 125, 557

Kniffen, D. A., & Gehrels, N. 1997, in *AIP Conf. Proc.* 410, *Proc. of the Fourth Compton Symp.*, ed. C. D. Dermer, M. S. Strickman, & J. D. Kurfess (Woodbury, NY: AIP), 524

Koh, D. T., et al. 1997, *ApJ*, 479, 933

Kong, A. K. H., Charles, P. A., & Kuulkers, E. 1998, *New Astron.*, 3, 301

Kouveliotou, C., van Paradijs, J., Fishman, G. J., Briggs, M. S., Kommers, J., Harmon, B. A., Meegan, C. A., & Lewin, W. H. G. 1996, *Nature*, 379, 799

Laycock, S., Coe, M. J., Wilson, C. A., Harmon, B. A., & Finger, M. H. 2003, *MNRAS*, 338, 211

Lei, F., Ferguson, C., Bird, J. A., Lockley, J. J., & Dean, J. A., 1999, *Astrophys. Lett. & Comm.*, 39, 373

Leonard, P. J. T., & Wanek, C. 2000, *S&T*, 100 (July), 48

Levine, A. M., et al. 1984, *ApJS*, 54, 581

Levine, A. M., Bradt, H., Cui, W., Jernigan, J. G., Morgan, E. H., Remillard, R., Shirey, R. E., & Smith, D. A. 1996, *ApJ*, 469, L33

Lichti, G. G., et al. 1995, *A&A*, 298, 711

Ling, J. C., Wheaton, W. A., Mahoney, W. A., Skelton, R. T., Radocinski, R. G., & Wallyn, P. 1996, *A&AS*, 120, no. 4, 677

Ling, J. C., et al. 1997, *ApJ*, 484, 375

Ling, J. C., et al. 2000, *ApJS*, 127, 79

Ling, J. C., & Wheaton, W. A. 2003, *ApJ*, 584, 399

Liu, Q. Z., van Paradijs, J., & van den Heuvel, E. P. J. 2000, *A&AS*, 147, 25

Liu, Q. Z., van Paradijs, J., & van den Heuvel, E. P. J. 2001, *A&A*, 368, 1021

Lund, N. 1986, *Proc. SPIE*, 597, 95

Macomb, D. J., & Gehrels, N. 1999, *ApJS*, 120, 335

Malizia, A., Bassani, L., Zhang, S. N., Dean, A. J., Paciesas, W. S., & Palumbo, G. G. C. 1999, *ApJ*, 519, 637

Malizia, A., Bassani, L., Dean, A. J., McCollough, M., Stephen, J. B., Zhang, S. N., & Paciesas, W. S. 2000, *ApJ*, 531, 642

McCollough, M. L., Wilson, C. A., Zhang, S. N., & Harmon, B. A. 1997, in *ESA SP-382, The Transparent Universe, Proc. of the 2nd INTEGRAL Workshop*, ed. C. Winkler, T.J.-L. Courvoisier, & P. Durouchoux (Noordwijk: ESA Publ. Div.), 547

McCollough, M. L., et al. 1999, *ApJ*, 517, 951

McSwain, M. V., Gies, D. R., Riddle, R. L., Wang, Z., & Wingert, D. W. 2001, *ApJ*, 558, L43

Meegan, C. A., Fishman, G. J., Wilson, R. B., Horack, J. M., Brock, M. N., Paciesas, W. S., Pendleton, G. N., & Kouveliotou, C. 1992, *Nature*, 355, 143

Mirabel, I.F., Rodriguez, L. F., Cordier, B., Paul, J., & Lebrun, F. 1992, *Nature*, 358, 215

Mirabel, I. F., & Rodriguez, L. F. 1994, *Nature*, 371, 46

Orosz, J. A., Remillard, R. A., Bailyn, C. D., & McClinton, J. E. 1997, *ApJ*, 478, L83

Paciesas, W. S., Mallozzi, R. S., Pendleton, G. N., Harmon, B. A., Wilson, C. A., Zhang, S. N., & Fishman, G. J. 1994, in *AIP Conf. Proc. 304, The Second Compton Symposium*, ed. C. E. Fichtel, N. Gehrels, & J. P. Norris (New York: AIP), 674

Paciesas, W. S., Deal, K. J., Harmon, B. A., Zhang, S. N., Wilson, C. A., & Fishman, G. J. 1996, *A&AS*, 120, no. 4, 205

Paciesas, W. S., Robinson, C. R., McCollough, M. L., Zhang, S. N., Harmon, B. A., & Wilson, C. A. 1997, in *AIP Conf. Proc. 410, Proc. of the Fourth Compton Symp.*, ed. C. D. Dermer, M. S. Strickman, & J. D. Kurfess (Woodbury, NY: AIP), 834

Parmar, A. N., Angelini, L., Roche, P., & White, N. E. 1993, *A&A*, 279, 179

Parsons, A. M., Gehrels, N., Paciesas, W. S., Harmon, B. A., Fishman, G. J., Wilson, C. A., & Zhang, S. N. 1998, *ApJ*, 501, 608

Paul, B., Kitamoto, S., & Makino, F. 2000, *ApJ*, 528, 410

Paul, J., et al. 1991, *Adv. Space Res.*, 11, no. 8, 177

Paul, J., Bouchet, L., Churazov, E., & Sunyaev, R. 1996, *IAU Circ.* 6348

Pendleton, G. N., et al. 1995, *Nucl. Instr. and Meth. in Phys. Res. A*, 364, 567

Petry, D., et al. 2000, *ApJ*, 536, 742

Pravdo, S. H., Day, C. S. R., Angelini, L., Harmon, B. A., Yoshida, A., & Saraswat, P. 1995, *ApJ*, 454, 872

Pravdo, S. H., & Ghosh, P. 2001, *ApJ*, 554, 383

Press, W. H., Teukolsky, S. A., Vetterling, W. T., & Flannery, B. P. 1992, *Numerical Recipes in Fortran, The Art of Scientific Computing* (2nd ed.; New York: Cambridge University Press), 569

Priedhorsky, W. C., & Holt, S. S. 1987, *Space Sci. Rev.*, 45, 291

Ray, P. S., & Chakrabarty, D. 2001, *BAAS*, 33, 804

Roques, J. P., Mandrou, P., Paul, J., & Lebrun, F. 1990, *Adv. Space Res.*, 10, no. 2, 223

Rubin, B. C., et al. 1996, *ApJ*, 459, 259

Rubin, B. C., Harmon, B. A., Paciesas, W. S., Robinson, C. R., Zhang, S. N., & Fishman, G. J. 1998, *ApJ*, 492, L67

Scargle, J. D. 1982, *ApJ*, 263, 835

Shrader, C. R., Wagner, R. M., Hjellming, R. M., Han, X. H., & Starrfield, S. G. 1994, *ApJ*, 434, 698

Shaw, S. E., et al. 2001, in *ESA SP-459, Proc. of the Fourth INTEGRAL Workshop*, ed. B. Battist, A. Gimenez, V. Reglero, & C. Winkler (Noordwijk: ESA Publ. Div.), 521

Shaw, S. E., Westmore, M. J., Bird, A. J., Dean, A. J., Ferguson, C., Gurriaran, R., Lockley, J. J., & Willis, D. R. 2003, *A&A*, 398, 391

Singh, N. S., Naik, S., Paul, B., Agrawal, P. C., Rao, A. R., & Singh, K. Y. 2002, *A&A*, 392, 161

Skelton, R. T., Ling, J. C., Radocinski, R., & Wheaton, W. A. 1994, in *AIP Conf. Proc. 304, The Second Compton Symposium*, ed. C. E. Fichtel, N. Gehrels, & J. P. Norris (New York: AIP), 758

Smith, D. M., Heindl, W. A., & Swank, J. H. 2002, *ApJ*, 578, L129

Soffitta, P., Tomsick, J. A., Harmon, B. A., Costa, E., Ford, E. C., Tavani, M., Zhang, S. N., Kaaret, P. 1998, *ApJ*, 494, L203

Standish, E. M., Newhall, X. X., Williams, J. G., & Yeomans, D. K. 1992, in *Explanatory Supplement to the Astronomical Almanac*, ed. P. K. Seidelmann (Mill Valley, CA: University Science Books), 279

Steinle, H., et al. 1998, *A&A*, 330, 97

Stollberg, M. T., Finger, M. H., Wilson, R. B., Harmon, B. A., Rubin, B. C., Zhang, S. N., & Fishman, G. J. 1993, *IAU Circ.* 5836

Stollberg, M. T., Finger, M. H., Wilson, R. B., Scott, D. M., Crary, D. J., & Paciesas, W. S. 1999, *ApJ*, 512, 313

Strickman, M., & Barret, D. 2000, in *AIP Conf. Proc. 510, The Fifth Compton Symposium*, ed. M. L. McConnell & J. M. Ryan (Melville, NY: AIP), 222

Sunyaev, R. A., Babichenko, S. I., Gogonov, D. A., Tabaldyev, S. R., & Iamburenko, N. S. 1990, *Adv. Space Res.*, 10, no. 2, 233

Sunyaev, R. et al. 1991, *ApJ*, 383, 49

Tavani, M., & Barret, D. 1997, in *AIP Conf. Proc. 410, Proc. of the Fourth Compton Symp.*, ed. C. D. Dermer, M. S. Strickman, & J. D. Kurfess (Woodbury, NY: AIP), 75

Tingay, S. J., et al. 1995, *Nature*, 374, 141

Tsunemi, H., Kitamoto, S., Manabe, M., Miyamoto, S., Yamashita, K., & Nakagawa, M. 1989, *PASJ*, 41, 391

Turler, M., et al. 1999, *A&AS*, 134, 89

Ubertini, P., et al. 1997, *IAU Circ.* 6611

van der Hooft, F. et al. 1999, *ApJ*, 513, 477

van Paradijs, J., & van der Klis, M. 1994, *A&A*, 281, L17

Vargas, M., et al. 1997, *ApJ*, 476, L23

Wachter, S. 1997, *ApJ*, 490, 401

Wheaton, W. A., Ling, J. C., Mahoney, W. A., Radocinski, R. G., Skelton, R. T., & Wallyn, P. 1996, *A&AS*, 120, no. 4, 545

White, S. M., Harmon, B. A., Lim, J., & Kundu, M. R. 1994, in *ASP Conf. Ser.* 64, *Proc. of the 8th Cambridge Workshop on Cool Stars, Stellar Systems, and the Sun*, ed. J-P. Caillault (San Francisco: ASP), 498

Wijers, R. A. M. J., & Pringle, J. E. 1999, *MNRAS*, 308, 207

Wilson, C. A., et al. 1995, *IAU Circ.* 6238

Wilson, C. A., Finger, M. H., Harmon, B. A., Scott, D. M., Wilson, R. B., Bildsten, L., Charabarty, D., & Prince, T. A. 1997a, *ApJ*, 479, 388

Wilson, C. A., Finger, M. H., Harmon, B. A., Chakrabarty, D., & Strohmayer, T. 1998, *ApJ*, 499, 820

Wilson, C. A., Finger, M. H., Coe, M. J., Laycock, S., & Fabregat, J. 2002, *ApJ*, 570, 287

Wilson, C. A., Finger, M. H., Coe, M. J., Negueruela, I. 2003, *ApJ*, 584, 996

Wilson-Hodge, C. A. 1999, Ph.D. Dissertation, University of Alabama, Huntsville

Wilson, R. B., Finger, M. H., Stollberg, M., Prince, T. A., Grunsfeld, J. M., Harmon, B. A., & Zhang, S. N. 1994, *IAU Circ.* 5955

Wilson, R. B., Harmon, B. A., Scott, D. M., Finger, M. H., Robinson, C. R., Chakrabarty, D., & Prince, T. A. 1997b, *IAU Circ.* 6586

Wilson, R. B., Harmon, B. A., & Finger, M. H. 1999, *IAU Circ.* 7116

Winkler, C. 2001, in *ESA SP-459, Proc. of the Fourth INTEGRAL Workshop*, ed. B. Battrick, A. Gimenez, V. Reglero, & C. Winkler (Noordwijk: ESA Publ. Div.), 471

Wojdowski, P., Clark, G. W., Levine, A. M., Woo, J. W., & Zhang, S. N. 1998, *ApJ*, 502, 253

Wu, K., Soria, R., Campbell-Wilson, D., Hannikainen, D., Harmon, B. A., Hunstead, R., Johnston, H., McCollough, M., & McIntyre, V. 2002, *ApJ*, 565, 1161

Zdziarski, A. A., Poutanen, J., Paciesas, W. S., & Wen, L. 2002, *ApJ*, 578, 357

Zhang, S. N., Fishman, G. J., Harmon, B. A., & Paciesas, W. S. 1993, *Nature*, 366, 245

Zhang, S. N., et al. 1994, *IAU Circ.* 6096

Zhang, S. N., Harmon, B. A., Paciesas, W. S. & Fishman, G. J. 1996a, *A&AS*, 120, no. 4, 137

Zhang, S. N., et al. 1996b, *A&AS*, 120, no. 4, 227

Zhang, S. N., Cui, W., Harmon, B. A., Paciesas, W. S., Remillard, R. E., & van Paradijs, J. 1997a, *ApJ*, 477, L95

Zhang, S. N., et al. 1997b, *ApJ*, 479, 381

Zhang, S. N., Harmon, B. A., & Liang, E. P. 1997c, in *AIP Conf. Proc.* 410, *Proc. of the Fourth Compton Symp.*, ed. C. D. Dermer, M. S. Strickman, & J. D. Kurfess (Woodbury, NY: AIP), 873

Table 1. OF_W Input Parameters

Parameter	Description	Value
2τ	Length of CONT data fitting window	220s
θ_{cut}	Aspect angle cutoff for “source-pointed” LADs	60°
θ_{int}	Aspect angle cutoff for interfering sources	70°
δ	Exclusion time for interfering source step	10s
λ	Fraction of data packets required in fitting window	0.95
ϕ_{cr}	Photon flux minimum level for interfering sources	0.01 ph cm ⁻² s ⁻¹ ^a

^aFlux value is for the energy band 20-100 keV with the assumed spectral model for the source (see Sec. 4)

Table 2. Occultation (OF_W) Persistent (P) Sources^a

Source Name	Type	Fit Range (keV)	Model	Param Value ^b	Time Range of Fit (TJD)	Flux (20-100 keV) (erg cm ⁻² s ⁻¹ ×10 ⁻⁸)	χ^2 /DOF
1E1740-29	LMXB?,BHC	20-600	PL	2.57±0.23	10008-10014	0.347	13.70/9
3C273	QSR	20-350	PL	1.7 (1.57±0.25)	9517-9521	0.077	10.06/7
4U0614+091	LMXB,NS	20-100	PL	2.24±0.70	10005-10008	0.162	1.67/3
4U1700-377	HMXB,NS	20-150	OTTB	25 (30.7±4.6)	8701-8705	0.325	3.43/4
4U1705-440	LMXB,NS	20-150	PL	3.17±0.45	9136-9140	0.274	1.15/4
CENX-3	HMXB,PSR	20-150	OTTB	10 (10.4±1.8)	9048-9053	0.220	6.13/4
CEN_A	SY2	20-500	PL	2.0 (2.15±0.10)	8899-8903	0.240	4.93/8
CRAB	SNR	20-200	PL	fl* (2.09±0.02)	10266-10272	1.732	5.80/4
CYGX-1	HMXB,BHC	20-350	PL	fl* (1.89±0.04)	10000-10005	2.367	55.32/7
...	OTTB	171.3±12.3	...	2.337	12.11/7
CYGX-3	HMXB,BHC?	20-200	PL	3.0 (2.81±0.20)	10940-10944	0.358	2.86/5
GRS1758-258	LMXB,BHC	20-200	PL	1.8 (2.72±0.35)	10838-10842	0.334	2.55/5
GX1+4	LMXB,PSR	20-200	OTTB	37.2±6.9	9703-9707	0.460	5.74/5
GX17+2	LMXB,NS	20-150	PL	2.81±0.72	10007-10012	0.263	3.85/4
GX301-2	HMXB,PSR	20-150	OTTB	8.0 (7.8±1.1)	8924-8928	0.927	1.06/4
GX354+0	LMXB,NS	20-120	OTTB	47.2±26.2	9888-9892	0.250	0.11/3
HERX-1	LMXB,PSR	20-120	OTTB	10 (10.4±2.1)	8965-8969	0.261	2.81/3
LMCX-4	HMXB,PSR	20-100	PL	3.67±0.75	9284-9289	0.187	3.02/3
NGC4151	SY1	20-150	PL	2.4 (1.90±0.30)	9660-9665	0.091	2.82/4
OAO1657-415	HMXB,PSR	20-200	OTTB	26 (36.5±4.3)	10600-10603	0.550	7.03/5
SCOX-1	LMXB,NS	20-150	PL	5.0 (5.38±0.09)	10001-10006	1.645	8.69/4
SMCX-1	HMXB,PSR	20-100	PL	2.96±0.66	11323-11330	0.065	2.56/3
VELAX-1	HMXB,PSR	20-100	OTTB	15 (11.3±0.8)	11282-11286	0.584	4.00/3

^aPlots and XSPEC input files for these spectra are available on <http://gamma-ray.msfc.nasa.gov/batse/occultation/>.

^bIn column 5, parameter values with errors result from spectral fits described in this table. Parameter values without errors

result from historical spectral fits and were used to generate flux histories. If only a single value is listed, the spectral model for flux histories was allowed to default to a power law with photon index = 3.0. For the Crab and Cyg X-1, f^* denotes that the power law index was allowed to float when flux histories were generated.

Table 3. Occultation (OF-W) Transient (T) Sources^a

Name	Type	Outburst Times (TJD)	Fit Range (keV)	Model	Param Value ^b	Time Range of Fit (TJD)	Flux (20-100 keV) (erg cm ⁻² s ⁻¹ ×10 ⁻⁸)	χ^2 /DOF
Pulsed Transients								
2S1417-624	PSR	9600-9708, 11542-11578	20-130	OTTB	27 (19.1±2.3)	9645-9650	0.400	7.64/4
4U0115+634	PSR	8363-8375, 9483-9523, 10040-10072, ... 10084-10093, 11228-11280	20-130	OTTB	16.1±3.3	10042-10046	0.226	6.97/4
4U1145-619	PSR	8866-8878, 9054-9078, 9230-9270, ... 9424-9445, 9610-9622, 9805-9811, ... 10186-10198, 10354-10363, 10546-10553	20-130	PL	3.77±0.28	10356-10361	0.344	3.24/4
A0535+262	PSR	9044-9057, 9180-9205, 9384-9433, ... 9493-9508	20-150	PL	3.66±0.31	9499-9503	0.241	6.32/4
A1118-616	PSR	8616-8678	20-130	OTTB	12.9±2.0	8619-8624	0.216	5.06/4
EXO2030+375	PSR	8385-8395, 8427-8439, 8475-8487, ... 8569-8583, 8619-8632, 8659-8673, ... 8705-8718, 8799-8807, 8842-8858, ... 8890-8906, 8936-8950, 9028-9042, ... 9076-9088, 9114-9137, 9166-9182, ... 9214-9228, 9261-9271, 9487-9498, ... 9580-9593, 9626-9640, 10313-10318, ... 10357-10367, 10404-10412, 10500-10508 ... 10998-11017	20-120	PL	1.64±0.71	8477-8482	0.092	3.38/3
GROJ1008-57	PSR	9182-9209	20-100	OTTB	25 (22.1±3.0)	9191-9195	0.400	7.85/3
GROJ1744-28	PSR	10052-10203, 10435-10560	20-150	PL	3.62±0.34	10189-10193	0.660	4.90/4
GROJ1944+26	PSR	11062-11682	20-120	OTTB	12 (5.2±3.1)	11504-11509	0.144	1.72/3
GROJ2058+42	PSR	9977-10016	20-120	OTTB	31.2±5.1	9991-9996	0.288	3.96/3
GRS0834-430	PSR	8375-8440, 8490-8550, 8590-8640, ... 8700-8750, 8810-8850, 8950-8990 ... 9100-9140	20-100	PL	3.7 (3.09±0.23)	8816-8821	0.264	6.52/3
GS1843+00	PSR	10478-10610	20-100	OTTB	31.2±4.6	10510-10515	0.364	2.70/3
GS1845-024	PSR	8404-8424, 8646-8666, 8886-8908, ... 9130-9150, 9370-9398, 9616-9638, ... 9856-9876, 10098-10122, 10342-10362, ... 10582-10608, 10824-10845, 11067-11084, ... 11307-11328, 11550-11571	20-150	PL	2.53±0.39	10836-10842	0.254	4.19/4
XTEJ0111-7317	PSR	11116-11203	20-100	OTTB	12 (13.5±9.1)	11175-11178	0.143	2.76/3
XTEJ1543-568	PSR	11610-11660	20-100	OTTB	15 (16.1±6.1)	11649-11654	0.141	0.86/3
Nonpulsed Transients								
4U1543-47	BHC	8729-8745, 8782-8843, 8880-9042	20-200	PL	2.7 (2.56±0.11)	8730-8735	0.562	7.28/5
4U1608-522	NS	8415-8602, 8620-8965, 9000-9075, ... 9340-9395, 10165-10280, 10380-10408,	20-300	OTTB	50 (76.7±15.5)	11511-11516	0.179	7.57/6

Table 3—Continued

Name	Type	Outburst Times (TJD)	Fit Range (keV)	Model	Param Value ^b	Time Range of Fit (TJD)	Flux (20-100 keV) (erg cm ⁻² s ⁻¹ ×10 ⁻⁸)	χ^2 /DOF
...	...	10920-11185, 11300-11600	...	PL	2.12±0.44	10889-10894	0.132	0.52/3
4U1630-47	BHC	10258-10335, 10842-11455	20-150	PL	2.48±0.24	9323-9329	0.196	3.81/5
AQLX-1	NS	8405-8590, 8720-8783, 9137-9593,	20-200	PL
...	...	9910-9950, 10232-10360, 10435-10550,	...	PL
...	...	11357-11486	...	PL
EXO1846-031	BHC	9302-9313	20-350	PL	2.08±0.11	9302-9307	0.243	4.15/7
GROJ0422+32	BHC	8840-9100	20-500	OTTB	110 (199.9±8.4)	8950-8955	0.356	12.54/8
GROJ1655-40	BHC	9540-9548, 9560-9580, 9590-9612,	20-300	PL	2.8 (2.55±0.09)	10370-10375	0.616	8.55/6
...	...	9644-9712, 9728-9740, 9759-9832,	...	PL
...	...	9920-9963, 10228-10480, 10510-10555,	...	PL
...	...	10592-10680	...	PL
GROJ1719-24	BHC	9252-9365, 9395-9471, 9502-10106	20-150	PL	2.3 (4.09±0.76)	9423-9427	0.173	2.61/4
GRS1009-45	BHC	9240-9384	20-500	PL	2.6 (2.42±0.09)	9271-9276	0.412	15.03/8
GRS1739-278	BHC	9950-10600	20-500	PL	1.62±0.40	10518-10523	0.097	6.45/7
GRS1915+105	BHC	8740- (e.o.m.)	20-350	PL	2.8 (2.80±0.10)	10410-10415	0.718	11.84/7
GS1354-645	BHC	10742-10855	20-300	OTTB	88.6±16.0	10800-10805	0.239	9.85/6
GS1826-238	NS	10145- (e.o.m.)	20-120	PL	2.07±0.37	11499-11505	0.158	1.86/3
GX339-4	BHC	8430-8650, 8865-9000, 9336-9506,	20-400	OTTB	60 (117.8±16.4)	8940-8945	0.408	6.99/7
...	...	9532-9712, 9753-10820, 11208-11310	...	PL
MKN501	Blazar	10549-10552, 10554-10555, 10645-10647,	20-500	PL	2.82±0.34	10549-10552	0.218	16.5/8
...	...	10682-10684, 10693-10694	...	PL
NOVA_MUSCAE	BHC	8400-8500	20-600	PL	2.5 (1.91±0.05)	8449-8455	0.233	8.89/9
V4641_SGR	BHC	11430-11437	20-200	PL	3.5 (3.23±0.13)	11430-11437	0.611	5.14/5
XTEJ0421+560	BHC	10903-10907	20-100	OTTB	26.9±9.4	10903-10907	0.191	0.23/2
XTEJ1118+480	BHC	11547-11561, 11626- (e.o.m.)	20-500	PL	2.1 (2.09±0.14)	11551-11556	0.188	3.24/8
XTEJ1550-564	BHC	11063-11148, 11200-11271, 11640- (e.o.m.)	20-500	OTTB	101 (108.9±4.9)	11645-11650	0.964	11.61/8
XTEJ1748-288	BHC	10967-10977, 10987-11025	20-300	PL	2.2 (2.88±0.12)	10969-10974	0.475	3.60/6
XTEJ1859+226	BHC	11460-11501	20-500	PL	2.1 (2.80±0.14)	11470-11475	0.395	8.80/8

^aPlots and XSPEC input files for these spectra are available on <http://gamma-ray.msfc.nasa.gov/batse/occultation/>.

^bIn column 6, parameter values with errors result from spectral fits described in this table. Parameter values without errors result from historical spectral fits and were used to generate flux histories. If only a single value is listed, the spectral model for flux histories was allowed to default to a power law with photon index = 3.0.

Table 4. BATSE Earth Occultation Deep Sample Results^a

Name	Alt Name	Type	Category ^b	$(\alpha, \delta)^c$ (deg)		$(l, b)^c$ (deg)	Significance	Flux (mCrab) ^{d,e}		160-430 keV		
				20-40	40-70			70-160	160-430 keV			
SMCX-3	SMC X-3	HMXB,PSR	C	13.02	-72.43	302.86	-44.69	4.0(5.6)	4.3 \pm 1.0	0.9 \pm 0.8	-0.5 \pm 0.8	-8.4 \pm 2.4
SMCX-2	SMC X-2	HMXB,PSR	C	13.64	-73.68	302.63	-43.44	4.1(5.7)	3.6 \pm 1.0	1.0 \pm 0.8	0.6 \pm 0.8	-1.5 \pm 2.4
XTEJ0111-7317	XTE J0111-732	HMXB,PSR	A [†]	17.80	-73.29	300.97	-43.76	1.2(1.7)	2.1 \pm 2.0	3.0 \pm 1.7	4.0 \pm 1.8	0.8 \pm 5.2
SMCX-1	SMC X-1	HMXB,PSR	B	19.27	-73.44	300.42	-43.56	28.7(40.1)	24.0 \pm 0.8	9.1 \pm 0.7	-0.6 \pm 0.8	-6.8 \pm 2.1
4U0115+634	...	HMXB,PSR	A [†]	19.63	63.74	125.93	1.03	13.4(18.4)	9.9 \pm 0.9	4.8 \pm 0.7	1.1 \pm 0.7	3.4 \pm 2.1
TTARI	TT ARI	Nova-like star	N	31.72	15.30	148.53	-43.80	-1.2(-1.7)	-0.4 \pm 0.7	-0.6 \pm 0.7	-2.2 \pm 0.7	-4.2 \pm 1.8
LSI+61-303	...	HMXB,Radio Star	C	40.13	61.23	135.68	1.09	5.2(9.5)	3.0 \pm 0.9	2.3 \pm 0.7	3.3 \pm 0.7	5.1 \pm 2.1
NGC1275	...	SY	B	49.95	41.51	150.58	-13.26	10.7(15.0)	7.4 \pm 0.8	3.0 \pm 0.7	3.4 \pm 0.7	4.0 \pm 2.0
V0332+530	V0332+53	HMXB,PSR	N	53.75	53.17	146.05	-2.20	1.0(2.3)	1.1 \pm 0.7	-0.1 \pm 0.7	-0.1 \pm 0.7	1.5 \pm 1.9
HR1099	...	RS CVn	C	54.20	0.59	184.91	-41.57	4.6(6.4)	2.3 \pm 0.7	1.7 \pm 0.7	0.4 \pm 0.7	2.0 \pm 1.8
XPER	X PER	HMXB,PSR	B	58.85	31.05	163.08	-17.14	23.8(33.3)	9.6 \pm 0.8	12.9 \pm 0.7	6.6 \pm 0.7	0.0 \pm 2.0
VWHYI	VW HYI	DN	N	62.30	-71.29	284.89	-38.13	2.0(2.8)	1.3 \pm 1.0	1.0 \pm 0.8	-1.1 \pm 0.8	-8.0 \pm 2.2
XTEJ0421+560	CI Cam	HMXB,BHC?	A [†]	64.90	56.00	149.17	4.12	1.8(4.5)	1.6 \pm 0.8	0.3 \pm 0.7	-0.1 \pm 0.7	1.5 \pm 1.9
GROJ0422+32	...	LMXB,BHC	A [†]	65.43	32.91	165.88	-11.91	120.7(169.0)	37.5 \pm 0.8	45.2 \pm 0.7	56.8 \pm 0.7	57.2 \pm 2.0
HD32918	...	RS CVn?	C	74.58	-75.28	287.41	-33.24	3.8(5.4)	2.5 \pm 1.0	2.3 \pm 0.8	1.1 \pm 0.8	-5.4 \pm 2.4
SAXJ0501+11	SAX J0501.7+1146	LMXB?,NS	C	75.43	11.78	188.91	-17.95	4.4(6.1)	2.5 \pm 0.8	1.5 \pm 0.7	1.8 \pm 0.7	-0.5 \pm 2.0
4U0512-041	4U 0513-40	LMXB,NS	N(C)	78.53	-40.04	244.51	-35.04	2.9(4.1)	0.7 \pm 0.8	2.4 \pm 0.7	0.9 \pm 0.8	2.3 \pm 2.1
SGR0526-66	...	SGR	N	81.50	-66.08	276.09	-33.25	1.2(1.6)	0.8 \pm 1.4	0.7 \pm 1.3	-0.5 \pm 1.3	-7.6 \pm 3.5
LMCX-4	LMC X-4	HMXB,PSR	B	83.21	-66.37	276.34	-32.53	25.9(36.3)	20.4 \pm 1.0	9.6 \pm 0.8	0.8 \pm 0.8	-8.0 \pm 2.2
CRAB	...	SNR,PSR	A	83.63	22.01	184.56	-5.78	1560.6(2055.7)	1021.7 \pm 0.8	1022.5 \pm 0.7	1022.5 \pm 0.7	1038.1 \pm 1.9
SN1987A	...	SNR	C	83.87	-69.27	279.71	-31.94	4.3(6.1)	3.9 \pm 1.1	2.2 \pm 1.0	1.8 \pm 1.0	-6.6 \pm 2.7
A0535-668	1A 0535-66	HMXB,PSR	N	83.92	-66.86	276.88	-32.20	-1.5(-2.0)	-0.3 \pm 2.0	-1.5 \pm 1.8	-2.9 \pm 1.8	-10.2 \pm 5.0
A0535+262	1A 0535+262	HMXB,PSR	A [†]	84.73	26.32	181.45	-2.64	46.6(64.7)	45.1 \pm 1.0	23.6 \pm 0.8	7.7 \pm 0.8	2.6 \pm 2.3
MCG8-11-11	MCG +08-11-011	SY1	C(B)	88.73	46.44	165.73	10.41	8.6(12.1)	4.5 \pm 0.8	4.6 \pm 0.8	5.4 \pm 0.8	2.5 \pm 2.2
4U0614+091	...	LMXB,NS	B	94.28	9.14	200.88	-3.36	40.4(54.0)	22.6 \pm 0.9	18.1 \pm 0.7	13.5 \pm 0.7	8.2 \pm 2.0
A0620-00	1A 0620-00	LMXB,BHC	C	95.69	-0.35	209.96	-6.54	6.5(3.8)	(0.1 \pm 0.7)	(3.0 \pm 0.6)	(1.1 \pm 0.6)	(7.3 \pm 1.0)
GEMINGA	...	SNR,PSR	C(N)	98.48	17.77	195.14	4.27	6.6(2.7)	(0.2 \pm 0.6)	(1.4 \pm 0.6)	(1.8 \pm 0.6)	(3.1 \pm 1.5)
PSR0656+14	...	PSR	N	104.95	14.24	201.11	8.26	1.6(-2.2)	(-1.0 \pm 0.6)	(-1.0 \pm 0.5)	(1.0 \pm 0.5)	(0.7 \pm 1.4)
EXO0748-676	...	LMXB,NS	B	117.14	-67.75	279.98	-19.81	15.4(21.6)	9.6 \pm 1.0	9.1 \pm 0.8	4.7 \pm 0.8	-5.7 \pm 2.2
CPPUP	CP PUP	Nova	N(I)	122.94	-35.35	252.93	-0.84	-1.2(-5.5)	-1.4 \pm 1.2	-0.5 \pm 1.0	-0.1 \pm 1.0	-0.3 \pm 3.1
VELA	...	SNR,PSR	B	128.84	-45.18	263.55	-2.79	14.7(24.3)	10.3 \pm 1.2	10.1 \pm 1.1	11.6 \pm 1.1	12.4 \pm 2.8
GRS0834-430	Ginga 0834-43	HMXB,PSR	A [†]	129.16	-43.26	262.16	-1.45	25.8(46.1)	22.1 \pm 1.1	14.8 \pm 1.1	7.1 \pm 1.1	4.3 \pm 3.0
4U0836-429	4U 0836-42	LMXB,NS	C(B)	129.35	-42.90	261.96	-1.12	7.6(12.4)	5.8 \pm 1.3	6.1 \pm 1.1	6.1 \pm 1.1	3.3 \pm 3.2
OJ287	OJ 287	BL Lac	C	133.70	20.11	206.81	35.82	4.3(6.1)	3.2 \pm 0.7	1.1 \pm 0.7	0.7 \pm 0.7	0.6 \pm 1.8
VELAX-1	VELA X-1	HMXB,PSR	A	135.53	-40.55	263.06	3.93	250.6(449.0)	227.2 \pm 1.1	84.1 \pm 0.9	8.1 \pm 0.9	1.7 \pm 2.7
H0918-549	...	LMXB,NS	N(C)	140.11	-55.21	275.85	-3.84	2.3(9.2)	1.7 \pm 1.2	1.5 \pm 1.0	0.8 \pm 1.0	-2.5 \pm 2.8
SN1993J	...	SNR	C	148.85	69.02	142.15	40.91	4.8(6.8)	2.0 \pm 1.0	2.9 \pm 0.8	3.2 \pm 1.0	8.5 \pm 2.4
GROJ1008-57	...	HMXB,PSR	A [†]	152.50	-58.31	283.03	-1.82	0.3(5.1)	0.3 \pm 1.2	0.2 \pm 1.0	0.0 \pm 1.0	-0.5 \pm 2.7
GRS1009-45	Granat 1009-45	LMXB,BHC	A [†]	153.40	-45.08	275.88	9.34	9.9(24.1)	6.6 \pm 1.0	5.3 \pm 0.9	4.4 \pm 1.0	3.5 \pm 2.6
1E1024-57	2E 1024.0-5733	HMXB?	N(C)	156.49	-57.81	284.52	-0.24	0.7(5.0)	0.6 \pm 1.2	0.4 \pm 1.0	0.0 \pm 1.0	-0.9 \pm 2.7
1E1048-593	2E 1048.1-5937	HMXB?	N(C)	162.54	-59.89	288.26	-0.52	-0.0(3.2)	0.0 \pm 1.1	0.0 \pm 1.0	0.0 \pm 1.1	0.0 \pm 2.8
PSR1055-52	...	PSR	N(C)	164.49	-52.45	285.99	6.65	0.5(4.1)	0.2 \pm 1.2	0.4 \pm 1.0	0.4 \pm 1.0	0.1 \pm 2.8
MKN421	...	BL Lac	C	166.11	38.21	179.83	65.03	4.4(6.2)	2.6 \pm 0.8	1.7 \pm 0.7	2.0 \pm 0.7	2.8 \pm 2.0
XTEJ1118+480	...	LMXB,BHC	A [†]	169.57	48.05	157.62	62.32	6.5(9.1)	3.0 \pm 0.8	3.2 \pm 0.8	3.8 \pm 0.8	6.1 \pm 2.2
A1118-616	1A 1118-616	HMXB,PSR	A [†]	170.24	-61.92	292.50	-0.89	-1.6(2.1)	(2.3 \pm 0.9)	(-1.1 \pm 0.8)	(-4.6 \pm 0.9)	(-5.5 \pm 2.3)
CENX-3	CEN X-3	HMXB,PSR	A	170.31	-60.62	292.09	0.34	33.9(62.3)	32.2 \pm 1.1	7.1 \pm 1.0	-2.7 \pm 1.0	-6.8 \pm 2.6
NOVA-MUSCAE	Nova Mus 1991	LMXB,BHC	A [†]	171.61	-68.68	295.30	-7.07	6.2(13.1)	4.1 \pm 1.1	4.1 \pm 1.0	3.1 \pm 1.1	0.2 \pm 2.9
AX1138-68	...	HMXB,PSR	C(N)	174.51	-69.90	296.66	-7.93	4.8(6.0)	(0.9 \pm 0.7)	(-0.2 \pm 0.6)	(-0.7 \pm 0.7)	(-5.1 \pm 1.8)
1E1145-614	1E 1145.0-6140	HMXB,PSR	B	176.87	-61.95	295.49	-0.01	22.7(37.3)	20.3 \pm 1.3	14.6 \pm 1.1	4.1 \pm 1.1	-5.3 \pm 3.1
4U1145-619	...	HMXB,PSR	A [†]	177.00	-62.21	295.61	-0.24	24.8(39.8)	22.2 \pm 1.1	16.4 \pm 1.1	4.7 \pm 1.1	-5.2 \pm 2.9
SN1994W	...	SNR	N	180.55	62.14	132.70	54.04	1.9(2.7)	1.6 \pm 1.0	0.8 \pm 0.8	0.9 \pm 0.8	8.5 \pm 2.4
NGC4151	...	SY1	A	182.64	39.40	155.08	75.06	93.0(130.2)	38.6 \pm 0.8	42.2 \pm 0.7	37.0 \pm 0.7	20.9 \pm 2.0
GX301-2	...	HMXB,PSR	A	186.66	-62.77	300.10	-0.03	155.8(221.3)	147.2 \pm 1.1	37.2 \pm 0.9	0.1 \pm 0.9	-3.3 \pm 2.6
3C273	...	QSR	B	187.28	2.05	289.95	64.36	51.7(72.4)	18.6 \pm 0.8	19.3 \pm 0.7	23.2 \pm 0.7	32.6 \pm 2.0
REJ1255+266	...	UVS	C	193.78	26.69	5.00	89.07	4.5(6.3)	2.8 \pm 0.8	2.0 \pm 0.7	1.0 \pm 0.8	0.1 \pm 2.1
3C279	...	QSR	C	194.05	-5.79	305.11	57.06	5.0(6.9)	2.8 \pm 0.8	2.1 \pm 0.7	3.0 \pm 0.7	7.0 \pm 2.1
4U1254-690	4U 1254-69	LMXB,NS	N(C)	194.40	-69.29	303.48	-6.42	2.1(8.4)	2.0 \pm 1.1	1.2 \pm 0.9	0.0 \pm 1.1	-3.1 \pm 2.8
GX304-1	...	LMXB,NS	I	195.32	-61.60	304.10	1.25	-3.7(-3.8)
PSR1259-63	...	HMXB?,PSR	N	195.70	-63.84	304.19	-0.99	-2.5(-1.7)	-3.2 \pm 1.1	-1.2 \pm 1.0	0.0 \pm 1.1	-13.4 \pm 2.9
CEN-A	...	SY2	A	201.37	-43.02	309.52	19.42	110.7(154.9)	40.7 \pm 0.8	46.0 \pm 0.8	54.5 \pm 0.8	66.3 \pm 2.2

Table 4—Continued

Name	Alt Name	Type	Category ^b	(α, δ) ^c (deg)		(l, b) ^c (deg)		Significance	Flux (mCrab) ^{d,e}			
				(α) (deg)	(δ) (deg)	(l) (deg)	(b) (deg)		20-40	40-70	70-160	160-430 keV
4U1323-619	4U 1323-62	LMXB,NS	B	201.65	-62.14	307.03	0.46	12.0(27.5)	8.2 ± 1.2	8.4 ± 1.0	4.7 ± 1.0	-0.1 ± 2.8
GS1354-645	Ginga 1354-64	LMXB,BHC	A [†]	209.50	-64.70	309.97	-2.74	4.0(14.4)	2.5 ± 1.2	2.5 ± 1.0	2.4 ± 1.0	-0.7 ± 2.8
NGC5548	...	SY1	B	214.50	25.13	31.95	70.50	13.3(18.6)	6.0 ± 0.8	6.3 ± 0.7	5.7 ± 0.7	6.4 ± 2.0
2S1417-624	...	HMXB,PSR	A [†]	215.30	-62.70	313.02	-1.60	15.5(26.2)	12.6 ± 1.2	9.2 ± 1.0	1.0 ± 1.0	-4.5 ± 2.8
CENX-4	CEN X-4	LMXB,NS	N(C)	224.59	-31.67	332.24	23.88	2.2(3.1)	0.9 ± 0.8	0.9 ± 0.7	1.2 ± 0.7	0.6 ± 2.1
PSR1509-58	...	SNR,PSR	B	228.48	-59.14	320.32	-1.16	11.8(26.5)	6.9 ± 1.1	6.9 ± 0.9	8.2 ± 0.9	9.7 ± 2.4
H1517+656	...	BL Lac	N	229.45	65.42	102.26	45.39	1.5(2.1)	0.2 ± 1.0	1.2 ± 0.8	1.9 ± 1.0	4.8 ± 2.5
CIRX-1	CIR X-1	LMXB,NS	C(B)	230.17	-57.17	322.12	0.04	3.8(16.1)	3.5 ± 1.1	1.2 ± 0.9	1.2 ± 0.9	0.3 ± 2.6
TRAX-1	TRA X-1	LMXB,NS	N	232.07	-61.88	320.32	-4.43	-1.1(-1.4)	-3.4 ± 1.1	0.2 ± 0.9	1.2 ± 0.9	-1.1 ± 2.6
4U1538-522	4U 1538-52	HMXB,PSR	B	235.60	-52.39	327.42	2.16	18.3(24.6)	16.3 ± 1.1	7.7 ± 0.9	1.3 ± 0.9	-4.1 ± 2.6
XTEJ1543-568	...	HMXB,PSR	A [†]	236.05	-56.74	324.99	-1.46	-3.7(-6.9)	-3.0 ± 1.1	-2.1 ± 0.9	-3.4 ± 0.9	-9.1 ± 2.6
4U1543-47	...	LMXB,BHC	A [†]	236.79	-47.67	330.92	5.43	10.1(16.6)	6.4 ± 1.0	5.0 ± 0.9	4.3 ± 0.9	1.5 ± 2.5
XTEJ1550-564	...	LMXB,BHC	A [†]	237.74	-56.48	325.88	-1.83	17.1(23.1)	10.5 ± 1.0	12.2 ± 0.9	7.1 ± 1.0	-2.3 ± 2.5
2S1553-542	...	HMXB,PSR	I	239.46	-54.41	327.95	-0.86	-5.3(-16.9)
4U1608-522	...	LMXB,NS	A [†]	243.17	-52.43	330.92	-0.85	50.9(43.8)	21.7 ± 1.0	31.9 ± 0.9	29.3 ± 1.0	9.9 ± 2.5
SCOX-1	SCO X-1	LMXB,NS	A	244.98	-15.64	359.10	23.78	460.6(644.9)	364.3 ± 0.8	45.0 ± 0.8	12.2 ± 0.8	9.9 ± 2.2
H1624-490	...	LMXB,NS	N(B)	247.02	-49.20	334.92	-0.27	0.0(24.7)	0.0 ± 1.2	0.0 ± 1.0	0.0 ± 1.2	0.0 ± 3.0
4U1627-673	4U 1626-67	LMXB,PSR	B	248.07	-67.46	321.79	-13.09	14.8(20.7)	14.5 ± 1.0	4.2 ± 1.0	-1.2 ± 1.0	-7.2 ± 2.7
4U1630-47	...	LMXB,BHC	A [†]	248.50	-47.39	336.91	0.26	-10.2(48.0)	(31.4 ± 0.8)	(24.3 ± 0.7)	(13.1 ± 0.8)	(10.0 ± 2.1)
SGR1627-41	...	SGR	I(B)	248.97	-47.60	336.97	-0.12	-5.4(19.5)
4U1636-536	...	LMXB,NS	B	250.23	-53.75	332.92	-4.82	10.9(21.3)	11.9 ± 1.3	5.2 ± 1.2	0.6 ± 1.2	-3.4 ± 3.0
GX340+0	...	LMXB,NS	C	251.45	-45.61	339.59	-0.08	4.8(4.8)	10.8 ± 1.3	-4.8 ± 1.2	-0.9 ± 1.2	-5.8 ± 3.3
MKN501	...	Blazar	A [†]	253.47	39.76	63.60	38.86	8.1(11.3)	5.4 ± 1.0	4.4 ± 0.8	4.9 ± 0.8	2.7 ± 2.5
GROJ1655-40	...	LMXB,BHC	A [†]	253.50	-39.85	344.98	2.46	40.6(45.0)	40.6 ± 1.6	35.0 ± 1.3	26.9 ± 1.5	23.4 ± 3.9
HERX-1	HER X-1	LMXB,PSR	A	254.46	35.34	58.15	37.52	58.4(81.8)	41.7 ± 0.8	14.1 ± 0.7	2.5 ± 0.8	1.4 ± 2.1
OAO1657-415	...	HMXB,PSR	A	255.20	-41.67	344.35	0.31	55.5(62.6)	64.4 ± 1.7	49.3 ± 1.4	12.1 ± 1.6	3.0 ± 4.2
A1658-298	3A 1658-298	LMXB,NS	N(I)	255.52	-29.95	353.83	7.27	-0.4(-12.3)	-0.4 ± 1.3	-0.2 ± 1.2	-0.2 ± 1.2	-0.2 ± 3.1
GX339-4	...	LMXB,BHC	A [†]	255.71	-48.79	338.94	-4.33	89.0(116.8)	58.8 ± 1.4	71.8 ± 1.2	73.7 ± 1.3	58.0 ± 3.5
4U1700-377	...	HMXB,NS?	A	255.99	-37.84	347.76	2.17	193.0(260.4)	212.8 ± 1.6	149.6 ± 1.3	63.6 ± 1.5	13.4 ± 3.9
GX349+2	...	LMXB,NS	B	256.43	-36.42	349.10	2.75	14.4(17.1)	21.9 ± 1.6	5.3 ± 1.5	2.3 ± 1.6	0.6 ± 4.2
4U1702-429	...	LMXB,NS	B	256.56	-43.04	343.89	-1.32	12.3(10.7)	20.2 ± 2.5	17.0 ± 2.2	14.1 ± 2.3	13.4 ± 6.4
H1705-250	...	LMXB,BHC	C(I)	257.06	-25.09	358.59	9.06	4.1(-6.6)	(-4.0 ± 1.0)	(-3.7 ± 0.8)	(-2.9 ± 0.9)	(2.7 ± 2.3)
4U1705-440	4U 1705-44	LMXB,NS	B	257.23	-44.10	343.32	-2.34	20.6(19.8)	22.8 ± 1.6	14.0 ± 1.4	10.8 ± 1.4	16.5 ± 3.9
PSR1706-44	...	PSR	N	257.43	-44.49	343.10	-2.69	2.1(-0.0)	(-1.1 ± 3.3)	(-5.2 ± 3.0)	(3.7 ± 3.3)	(10.2 ± 9.1)
MXB1715-321	1H 1715-321	LMXB,NS	I	259.70	-32.18	354.13	3.07	-6.8(-12.4)
GROJ1719-24	...	LMXB,BHC	A [†]	259.90	-24.97	0.18	7.02	70.4(78.5)	38.1 ± 1.5	58.7 ± 1.3	57.6 ± 1.4	45.3 ± 3.5
1E1724-307	4U 1724-307	LMXB,NS	A	261.89	-30.80	356.32	2.30	22.7(27.7)	30.3 ± 2.4	32.5 ± 2.0	21.6 ± 2.1	11.3 ± 5.7
GX9+9	...	LMXB,NS	B	262.93	-16.96	8.51	9.04	12.2(11.2)	15.3 ± 1.5	6.5 ± 1.3	3.4 ± 1.3	7.9 ± 3.6
GX354+0	...	LMXB,NS	B	263.00	-33.84	354.30	-0.16	50.2(68.2)	46.4 ± 1.3	34.5 ± 1.1	18.2 ± 1.1	2.0 ± 3.2
GX1+4	...	HMXB,PSR	A	263.01	-24.75	1.94	4.80	85.8(109.9)	82.9 ± 1.6	76.0 ± 1.3	28.7 ± 1.4	3.4 ± 3.6
1730-335	4U 1730-333	LMXB,NS	N	263.35	-33.39	354.84	-0.16	-1.0(-0.7)	(-6.7 ± 3.1)	(4.2 ± 2.7)	(4.4 ± 2.9)	(2.8 ± 7.7)
KS1731-260	...	LMXB,NS	N(C)	263.55	-26.09	1.07	3.66	1.6(6.1)	4.1 ± 3.3	2.8 ± 2.8	0.3 ± 3.0	-0.1 ± 8.1
SLX1732-304	...	LMXB,NS	I(N)	263.95	-30.48	357.56	0.99	-6.3(-0.5)
GX359+2	...	LMXB,NS	I(C)	264.65	-28.48	359.57	1.55	-12.0(9.1)
4U1735-444	...	LMXB,NS	C	264.74	-44.45	346.06	-6.99	4.0(3.1)	10.3 ± 1.5	-3.9 ± 1.3	1.3 ± 1.4	9.0 ± 3.7
GRS1737-31	Granat 1737-31	LMXB,BHC	I	264.95	-30.96	357.62	0.01	-12.1(-4.0)
XTEJ1739-285	...	XRS	I(C)	264.98	-28.48	359.73	1.31	-16.9(6.0)
GRS1739-278	Granat 1739-278	LMXB,BHC	A [†]	265.67	-27.75	0.67	1.18	0.3(20.3)	0.6 ± 3.7	0.5 ± 3.1	0.3 ± 3.2	0.2 ± 8.7
1E1740-29	1E1740.7-2942	LMXB [?] ,BHC	A	265.97	-29.74	359.12	-0.10	92.4(183.9)	76.7 ± 1.5	74.3 ± 1.4	74.6 ± 1.4	61.2 ± 3.7
GROJ1744-28	...	LMXB,PSR	A [†]	266.14	-28.74	0.05	0.30	5.5(27.7)	17.2 ± 4.3	11.4 ± 3.8	4.3 ± 4.1	4.8 ± 10.9
KS1741-293	...	LMXB,NS	N(A)	266.20	-29.35	359.56	-0.07	0.8(14.7)	3.2 ± 6.8	2.9 ± 6.0	1.0 ± 6.4	1.3 ± 17.5
H1743-322	...	LMXB,NS	N(C)	266.26	-32.23	357.13	-1.61	2.5(3.9)	1.6 ± 2.6	4.6 ± 2.3	5.9 ± 2.3	9.4 ± 6.2
SLX1744-300	...	LMXB,NS	C(A)	266.86	-30.04	359.26	-0.91	7.7(44.4)	10.6 ± 1.9	7.5 ± 1.7	4.9 ± 1.8	5.2 ± 4.7
GX3+1	...	LMXB,NS	B	266.98	-26.56	2.30	0.79	13.1(29.0)	15.2 ± 1.4	8.1 ± 1.3	5.5 ± 1.3	8.5 ± 3.6
XTEJ1748-288	...	LMXB,BHC	A [†]	267.03	-28.48	0.68	-0.23	-12.4(49.9)	(40.5 ± 1.1)	(28.9 ± 1.0)	(17.8 ± 1.0)	(18.9 ± 2.6)
H1745-203	...	LMXB,NS	I	267.22	-20.37	7.73	3.80	-7.3(-10.3)
XBO1745-248	GPS 1745-248	LMXB,NS	C(B)	267.23	-24.89	3.84	1.46	10.0(10.8)	11.6 ± 1.5	5.4 ± 1.3	5.2 ± 1.3	7.5 ± 3.5
GROJ1750-27	...	HMXB,PSR	N(B)	267.50	-27.00	2.16	0.17	1.2(20.1)	1.4 ± 1.4	0.6 ± 1.3	0.5 ± 1.3	1.0 ± 3.3
4U1746-370	4U 1746-37	LMXB,NS	N	267.55	-37.05	353.53	-5.00	0.5(2.7)	0.9 ± 1.5	0.5 ± 1.3	0.2 ± 1.3	0.3 ± 3.7
EXO1747-214	...	LMXB,NS	I	267.61	-21.42	7.00	2.95	-10.7(-11.4)

Table 4—Continued

Name	Alt Name	Type	Category ^b	$(\alpha, \delta)^c$		$(l, b)^c$ (deg)	Significance	Flux (mCrab) ^{d,e}				
				(deg)	(deg)			20-40	40-70	70-160	160-430 keV	
SAXJ1750-29	SAX J1750.8-2900	LMXB?,NS	I(B)	267.70	-29.00	0.53	-1.00	-12.4(30.9)	
XTEJ1755-324	...	LMXB,BHC	C(B)	268.87	-32.48	358.04	-3.63	7.1(15.0)	7.7 ± 1.5	5.5 ± 1.2	3.8 ± 1.4	5.9 ± 3.4
H1755-338	...	LMXB,NS	C	269.67	-33.81	357.22	-4.87	8.2(8.1)	8.3 ± 1.4	6.1 ± 1.2	4.3 ± 1.4	7.2 ± 3.4
GX5-1	...	LMXB,NS	C	270.28	-25.08	5.08	-1.02	3.8(6.0)	21.2 ± 6.8	8.4 ± 6.0	-7.7 ± 6.4	-24.0 ± 17.5
GRS1758-258	Granat 1758-258	LMXB,BHC	A	270.30	-25.74	4.51	-1.36	74.3(106.3)	46.8 ± 1.3	42.4 ± 1.1	50.4 ± 1.1	38.0 ± 3.0
GX9+1	...	LMXB,NS	N	270.38	-20.53	9.08	1.15	2.1(0.2)	(6.3 ± 1.0)	(-5.5 ± 0.9)	(-7.3 ± 0.9)	(-8.5 ± 2.4)
2S1803-245	...	LMXB,BHC	I	271.71	-24.58	6.15	-1.90	-5.9(-3.1)
SGR1806-20	AX 1805.7-2025	SGR	N	272.17	-20.41	10.00	-0.24	-1.6(-0.5)	(1.1 ± 0.9)	(-1.2 ± 0.8)	(-2.9 ± 0.8)	(-9.5 ± 2.1)
NOVA-SAG	Nova Sgr 1991	Nova	N(I)	273.56	-32.21	0.20	-6.97	2.2(-13.1)	(-7.5 ± 0.9)	(-7.2 ± 0.8)	(-5.5 ± 0.9)	(-6.2 ± 2.2)
GX13+1	...	LMXB,PSR	C	273.63	-17.16	13.52	0.11	7.7(4.0)	(1.6 ± 1.0)	(3.1 ± 0.9)	(0.8 ± 1.0)	(-2.2 ± 2.5)
4U1812-12	...	LMXB,NS	B	273.81	-12.03	18.11	2.40	16.2(22.9)	22.5 ± 2.5	25.2 ± 2.2	21.1 ± 2.3	15.6 ± 6.0
GX17+2	...	LMXB,NS?	A	274.01	-14.04	16.43	1.28	65.4(85.2)	56.1 ± 1.2	32.1 ± 1.0	24.4 ± 1.0	12.0 ± 2.8
AM-HER	...	CV	N	274.05	49.87	77.87	25.88	1.5(2.1)	2.3 ± 1.0	0.4 ± 0.8	-1.2 ± 1.0	-2.3 ± 2.4
V4641-5GR	...	LMXB,BHC	A [†]	274.84	-25.41	6.78	-4.79	-6.9(-4.7)	(-0.6 ± 0.9)	(-3.3 ± 0.7)	(-4.6 ± 0.8)	(-8.8 ± 2.0)
4U1820-303	...	LMXB,NS	B(C)	275.92	-30.36	2.79	-7.91	13.9(9.1)	(10.9 ± 0.8)	(-1.5 ± 0.7)	(-3.5 ± 0.7)	(-7.9 ± 1.9)
H1822-000	...	LMXB,NS	N(I)	276.34	-0.01	29.94	5.79	-0.8(-9.9)	-0.6 ± 1.2	-0.4 ± 1.0	-0.5 ± 1.0	-0.1 ± 2.6
H1822-371	...	LMXB,NS	B	276.45	-37.10	356.85	-11.29	17.7(24.8)	21.5 ± 1.1	2.5 ± 1.0	-1.9 ± 1.0	-6.3 ± 2.7
LS5039	...	HMXB,BHC	B(C)	276.56	-14.85	16.88	-1.29	10.7(7.3)	(3.4 ± 0.8)	(3.0 ± 0.7)	(2.0 ± 0.7)	(3.0 ± 1.8)
GS1826-238	Ginga 1826-238	LMXB,NS	A [†]	277.37	-23.80	9.27	-6.09	25.5(64.0)	15.7 ± 1.1	17.0 ± 1.0	12.7 ± 1.0	5.3 ± 2.7
SCTX-1	SCT X-1	HMXB,PSR	N(I)	279.18	-7.58	24.51	-0.20	-1.1(-3.3)	-1.1 ± 1.2	-0.6 ± 1.0	0.6 ± 1.0	2.0 ± 2.6
SERX-1	SER X-1	LMXB,NS	C(B)	279.99	5.04	36.12	4.84	6.0(14.2)	5.0 ± 1.1	2.7 ± 0.9	2.2 ± 1.1	2.5 ± 2.7
GS1843+00	Ginga 1843+00	HMXB,PSR	A [†]	281.50	1.00	33.20	1.67	18.8(36.1)	11.6 ± 1.0	11.0 ± 1.0	7.6 ± 1.0	6.8 ± 2.6
GS1845-024	2S 1845-024	HMXB,PSR	A [†]	282.07	-2.42	30.42	-0.40	2.3(35.9)	1.4 ± 1.0	1.4 ± 0.9	0.8 ± 1.0	0.5 ± 2.6
EXO1846-031	...	LMXB,BHC	A [†]	282.30	-3.10	29.92	-0.92	-1.7(24.5)	(10.3 ± 0.8)	(10.9 ± 0.7)	(6.7 ± 0.7)	(4.6 ± 1.8)
4U1850-087	4U 1850-08	LMXB,NS	C(B)	283.27	-8.71	25.36	-4.32	8.8(16.3)	5.6 ± 1.0	5.7 ± 0.9	4.1 ± 1.0	1.3 ± 2.5
XTEJ1859+226	...	LMXB,BHC	A [†]	284.67	22.66	54.05	8.61	6.2(-3.6)	(-2.2 ± 0.7)	(-0.7 ± 0.6)	(-0.7 ± 0.7)	(-3.4 ± 1.8)
SGR1900+14	...	SGR	C(B)	286.81	9.32	43.02	0.77	9.2(52.1)	7.2 ± 1.1	4.8 ± 0.9	3.0 ± 1.1	1.1 ± 2.6
4U1905+000	4U 1857+01	LMXB,NS	I	287.11	0.17	35.03	-3.71	-6.9(-10.7)
4U1907+097	...	HMXB,PSR	C(B)	287.41	9.83	43.74	0.48	10.0(51.1)	8.6 ± 1.1	5.1 ± 0.9	2.8 ± 1.1	1.4 ± 2.8
AQLX-1	AQL X-1	LMXB,NS	A [†]	287.82	0.58	35.72	-4.14	22.8(36.6)	15.9 ± 1.1	13.4 ± 0.9	9.3 ± 1.1	1.8 ± 2.6
SS433	...	HMXB,NS?	B	287.96	4.98	39.70	-2.24	21.7(39.9)	17.7 ± 1.0	11.8 ± 1.0	4.9 ± 1.0	0.0 ± 2.8
GRS1915+105	Granat 1915+105	LMXB,BHC	A [†]	288.82	10.97	45.40	-0.23	208.8(359.5)	163.3 ± 1.1	114.7 ± 1.0	63.7 ± 1.0	33.5 ± 2.7
4U1916-053	...	LMXB,NS	B(N)	289.70	-5.24	31.36	-8.46	12.5(0.4)	(0.9 ± 0.7)	(-0.2 ± 0.6)	(-1.0 ± 0.6)	(-1.6 ± 1.7)
1940-04	XB 1940-04	LMXB,NS	N	295.65	-3.88	35.32	-13.15	-1.8(-2.5)	-1.5 ± 0.8	0.6 ± 0.8	-0.3 ± 0.8	0.7 ± 2.2
GROJ1944+26	...	HMXB,PSR	A [†]	296.41	27.36	63.20	1.40	4.5(5.1)	4.3 ± 1.1	1.1 ± 0.9	-2.4 ± 1.1	-3.7 ± 2.7
GROJ1948+32	...	HMXB,PSR	N	298.00	30.00	66.19	1.53	-1.2(-1.5)	-0.1 ± 1.1	-0.8 ± 1.1	-4.8 ± 1.1	-6.5 ± 2.9
PSR1951+32	...	PSR	N	298.24	32.88	68.77	2.82	-2.8(2.8)	(2.8 ± 0.7)	(0.6 ± 0.7)	(-4.5 ± 0.7)	(-3.1 ± 1.8)
H1954+319	...	HMXB,NS	N(C)	298.93	32.01	68.32	1.88	1.8(8.6)	2.2 ± 1.3	1.0 ± 1.1	-1.6 ± 1.1	-0.5 ± 3.2
CYGX-1	CYG X-1	HMXB,BHC	A	299.59	35.20	71.34	3.07	1186.8(1870.2)	876.9 ± 0.9	1019.5 ± 0.9	1128.6 ± 0.9	924.5 ± 2.5
ASM2000+25	Ginga 2000+25	LMXB,BHC	N	300.53	25.14	63.20	-2.91	0.1(-2.2)	0.0 ± 1.1	0.0 ± 0.9	0.2 ± 1.1	0.0 ± 2.8
XTEJ2012+381	...	LMXB,BHC	I(C)	303.16	38.18	75.39	2.25	-3.8(3.2)
WR140	...	HMXB,NS	C	305.12	43.85	80.93	4.18	5.2(5.4)	1.9 ± 1.0	3.6 ± 0.9	6.6 ± 0.9	11.3 ± 2.5
GS2023+338	Ginga 2023+338	LMXB,BHC	I(N)	306.02	33.87	73.12	-2.09	-7.5(2.1)
NOVA-CYG	Nova Cyg 1992	Nova	N	307.63	52.63	89.13	7.82	2.0(2.9)	1.0 ± 1.0	1.1 ± 0.9	-0.1 ± 0.9	2.6 ± 2.2
EXO2030+375	...	HMXB,PSR	A [†]	308.06	37.64	77.15	-1.24	-7.0(-2.4)	(1.7 ± 0.7)	(-1.0 ± 0.7)	(-3.6 ± 0.7)	(-5.3 ± 1.9)
CYGX-3	CYG X-3	HMXB,BH?	A	308.11	40.96	79.85	0.70	197.8(264.3)	131.7 ± 0.8	77.0 ± 0.8	31.8 ± 0.8	15.5 ± 2.1
AEAQR	AE AQR	CV	N(I)	310.04	-0.87	45.28	-24.42	-2.3(-3.2)	-1.4 ± 0.8	-0.6 ± 0.7	-2.1 ± 0.7	0.7 ± 2.0
GRS2037-404	Granat 2037-404	LMXB,BHC?	N	310.11	-40.24	1.46	-37.28	-0.6(-0.9)	-0.6 ± 0.8	-0.1 ± 0.7	0.3 ± 0.7	2.5 ± 2.1
GROJ2058+42	...	HMXB?,PSR	A[†]	314.23	42.70	84.04	-1.79	7.9(2.0)	(1.7 ± 0.7)	(1.2 ± 0.6)	(-1.4 ± 0.6)	(-0.5 ± 1.7)
SAXJ2103+45	SAX J2103.5+4545	HMXB,PSR	C	315.89	45.75	87.13	-0.68	6.8(6.1)	4.2 ± 0.9	2.6 ± 0.7	-0.4 ± 0.7	3.4 ± 2.0
4U2127+119	...	LMXB,NS	B	322.49	12.17	65.01	-27.31	11.3(15.8)	5.6 ± 0.7	5.2 ± 0.7	2.8 ± 0.7	-3.3 ± 2.0
4U2129+470	4U 2129+47	LMXB,NS	N	322.86	47.29	91.58	-3.04	0.8(2.4)	0.7 ± 0.9	0.0 ± 0.7	0.8 ± 0.7	0.3 ± 2.0
CEPX-4	CEP X-4	HMXB,PSR	N(C)	324.90	57.00	99.03	3.32	1.1(4.8)	0.7 ± 0.9	0.4 ± 0.7	0.5 ± 0.7	-0.7 ± 2.1
SSCYG	SS CYG	DN	C(B)	325.68	43.59	90.56	-7.11	9.3(13.2)	5.7 ± 0.7	3.4 ± 0.6	3.0 ± 0.7	1.0 ± 1.9
CYGX-2	CYG X-2	LMXB,NS	B	326.17	38.32	87.33	-11.32	19.8(27.7)	15.0 ± 0.8	3.7 ± 0.7	2.6 ± 0.7	2.0 ± 2.0
PKS2155-30	QSO 2155-304	BL Lac	C	329.72	-30.23	17.73	-52.25	6.3(8.8)	3.3 ± 0.8	2.5 ± 0.7	2.8 ± 0.7	2.6 ± 2.0
ARLACERT	AR Lac	RS CVn	N	332.17	45.74	95.56	-8.30	-1.4(-1.1)	-1.0 ± 0.7	0.0 ± 0.7	-0.2 ± 0.7	2.6 ± 1.8
G109-1	GAL 109.1-01.0	SNR,PSR	N	345.28	58.88	109.09	-1.00	0.4(2.2)	0.1 ± 0.9	0.3 ± 0.7	0.5 ± 0.7	0.9 ± 2.1
CAS-A	...	SNR	C(B)	350.85	58.81	111.74	-2.13	7.2(11.0)	4.2 ± 0.9	2.9 ± 0.7	1.9 ± 0.7	2.6 ± 2.0

^aDaily 4-band light curves in Crab units for the 83 category A & B sources and FITS files containing daily 20-100 keV fluxes and 16-channel spectra for all 179 sources are available on <http://gammaray.msfc.nasa.gov/batse/occultation/>.

^b A^\dagger denotes a category A transient source, otherwise the source is considered a persistent source.

^clisted positions should be used for reference only. These positions were used in the analysis, and many are based on historical measurements and are often only accurate to within a few arcminutes. Location errors of a few arcminutes do not significantly affect flux measurements with the BATSE EOT.

^dConversion factors from mCrab units to photon and energy fluxes are given in Appendix B, Table B2.

^eParenthesis denote cases where the uncorrected flux was very small relative to the systematic flux correction. In these cases the uncorrected 4-band fluxes are reported because we believe they are closer to the true 9.1-year averages. See section 4.3 for details.

Table 5. BATSE Deep Sample Category “B” Sources

Name	Type	Behavior	F (ph cm $^{-2}$ s $^{-1}$)	F_{cor} (ph cm $^{-2}$ s $^{-1}$)	δF (ph cm $^{-2}$ s $^{-1}$)	ϵ_{cor}	(20-40) (mCrab)	(40-70) (mCrab)	(70-160) (mCrab)	(160-430) (mCrab)
SMCX-1	HMXB,PSR	P	4.27E-03	0.00E+00	1.06E-04	1.40	24.2 \pm 0.6	9.2 \pm 0.5	-0.6 \pm 0.6	-70 \pm 1.5
NGC1275	SY	...	1.84E-03	0.00E+00	1.23E-04	1.40	7.1 \pm 0.6	3.1 \pm 0.5	3.3 \pm 0.5	3.9 \pm 1.4
XPER	HMXB,PSR	...	3.90E-03	0.00E+00	1.17E-04	1.40	9.6 \pm 0.5	12.7 \pm 0.5	6.5 \pm 0.5	-0.2 \pm 1.3
LMCX-4	HMXB,PSR	P	5.60E-03	0.00E+00	1.55E-04	1.40	20.2 \pm 0.6	9.4 \pm 0.6	0.7 \pm 0.6	-8.0 \pm 1.5
4U0614+091	LMXB,NS	P	5.98E-03	-5.87E-04	1.11E-04	1.47	20.6 \pm 0.6	16.6 \pm 0.5	12.4 \pm 0.5	8.0 \pm 1.4
EXO0748-676	LMXB,NS	...	3.16E-03	0.00E+00	1.46E-04	1.40	9.2 \pm 0.7	8.8 \pm 0.6	5.1 \pm 0.6	-6.1 \pm 1.6
VELA	SNR,PSR	...	3.47E-03	-2.57E-04	1.42E-04	1.77	9.5 \pm 0.6	9.3 \pm 0.6	10.6 \pm 0.6	11.6 \pm 1.6
1E1145-614	HMXB,PSR	...	6.06E-03	8.64E-05	1.62E-04	1.62	20.5 \pm 0.7	14.8 \pm 0.6	4.2 \pm 0.7	-6.5 \pm 1.8
3C273	QSR	P	4.13E-03	0.00E+00	5.71E-05	1.40	18.4 \pm 0.5	19.2 \pm 0.5	23.1 \pm 0.5	32.3 \pm 1.4
4U1323-619	LMXB,NS	...	4.00E-03	1.08E-03	1.46E-04	1.66	11.3 \pm 0.7	11.2 \pm 0.6	6.3 \pm 0.6	-0.3 \pm 1.6
NGC5548	SY1	...	2.22E-03	0.00E+00	1.19E-04	1.40	6.3 \pm 0.5	6.3 \pm 0.5	5.7 \pm 0.5	5.8 \pm 1.4
PSR1509-58	SNR,PSR	...	3.76E-03	1.21E-03	1.42E-04	1.53	10.3 \pm 0.6	10.3 \pm 0.6	11.7 \pm 0.6	14.1 \pm 1.6
4U1538-522	HMXB,PSR	...	3.66E-03	-4.37E-04	1.49E-04	1.50	14.8 \pm 0.7	6.8 \pm 0.6	1.1 \pm 0.6	-3.8 \pm 1.7
4U1627-673	LMXB,PSR	...	3.31E-03	0.00E+00	1.60E-04	1.40	14.5 \pm 0.7	4.2 \pm 0.6	-1.3 \pm 0.7	-7.3 \pm 1.8
4U1636-536	LMXB,NS	...	3.93E-03	1.05E-03	1.84E-04	1.44	15.8 \pm 0.8	7.4 \pm 0.7	0.7 \pm 0.8	-5.1 \pm 2.1
GX349+2	LMXB,NS	...	4.53E-03	-6.12E-04	2.65E-04	1.35	20.3 \pm 1.2	5.0 \pm 1.1	2.6 \pm 1.1	0.0 \pm 3.0
4U1702-429	LMXB,NS	P	4.31E-03	-2.11E-03	4.02E-04	1.30	14.1 \pm 1.8	11.2 \pm 1.6	10.0 \pm 1.7	9.4 \pm 4.7
4U1705-440	LMXB,NS	P	5.51E-03	-1.96E-03	2.78E-04	1.31	17.6 \pm 1.2	10.3 \pm 1.0	7.9 \pm 1.1	12.7 \pm 2.9
GX9+9	LMXB,NS	...	2.40E-03	-1.47E-03	2.14E-04	1.49	9.2 \pm 1.0	3.8 \pm 0.8	2.2 \pm 0.9	5.2 \pm 2.3
GX354+0	LMXB,NS	P	9.56E-03	5.77E-04	1.40E-04	1.28	49.4 \pm 1.0	37.1 \pm 0.9	19.1 \pm 0.9	1.9 \pm 2.4
GX3+1	LMXB,NS	...	6.36E-03	2.25E-03	2.20E-04	1.43	23.4 \pm 1.0	12.4 \pm 0.9	8.3 \pm 0.9	12.9 \pm 2.4
4U1812-12	LMXB,NS	...	8.13E-03	-3.26E-04	3.56E-04	1.47	20.7 \pm 1.6	23.5 \pm 1.4	20.4 \pm 1.5	14.3 \pm 4.0
4U1820-303	LMXB,NS	...	1.55E-03	-1.68E-03	1.70E-04	1.37	10.6 \pm 0.8	-1.7 \pm 0.7	-3.4 \pm 0.7	-8.5 \pm 1.8
H1822-371	LMXB,NS	...	4.06E-03	0.00E+00	1.64E-04	1.40	21.2 \pm 0.7	2.5 \pm 0.6	-2.2 \pm 0.7	-6.5 \pm 1.8
LS5039	HMXB,BHC	...	1.20E-03	-1.43E-03	1.66E-04	1.48	3.2 \pm 0.7	2.9 \pm 0.7	2.0 \pm 0.7	3.7 \pm 1.8
SS433	HMXB,NS?	...	6.36E-03	1.20E-03	1.59E-04	1.49	21.9 \pm 0.7	14.7 \pm 0.6	6.1 \pm 0.7	-0.2 \pm 1.8
4U1916-053	LMXB,NS	...	6.27E-05	-2.61E-03	1.48E-04	1.44	0.6 \pm 0.7	-0.4 \pm 0.6	-1.0 \pm 0.6	-1.6 \pm 1.7
4U2127+119	LMXB,NS	...	1.87E-03	0.00E+00	1.18E-04	1.40	5.7 \pm 0.5	5.1 \pm 0.5	2.8 \pm 0.5	-2.6 \pm 1.4
CYGX-2	LMXB,NS	...	3.40E-03	0.00E+00	1.23E-04	1.40	15.2 \pm 0.6	3.8 \pm 0.5	2.5 \pm 0.5	2.0 \pm 1.4

Note. — Definitions for F , δF , F_{cor} , and ϵ_{cor} are given in Eq. (1).

Table 6. Orbital, Superorbital and Quasi- Periods Observed in BATSE EO Light Curves

Name	Other Instruments/Meth			Earth Occultation		
	P_{orb} (d)	P_{long} (d)	refs	<i>FFT Peaks</i>		FAP
Category A						
4U 1700-377	3.411581	...	[4]	3.411±0.001	...	3.43E-65
CEN X-3	2.08706533	~140	[1]	2.0873±0.0003	...	5.28E-25
CYG X-1	5.599829	294	[3,8]	5.6 ^a
CYG X-3	4.792426h	...	[6]	4.79249h ^a
EXO2030+375	46.0	...	[7]	45.9±0.1	...	5.78E-20
GRO J2058+42	~110	...	[2]	97.5±0.4	...	2.88E-3
GRS 0834-430	105.8	...	[2]	broad power 97-118	...	<7.48E-6
GS 1845-024	242.18	...	[5]	241.9±4.5	...	1.63E-10
GX 301-2	41.498	...	[2,3]	41.49±0.07	...	4.91E-77
HER X-1	1.700167412	35	[1,2]	...	34.80±0.04	<1.0E-99
AOO 1657-415	10.44809	...	[2]	10.45±0.01	...	2.21E-46
VELA X-1	8.964368	...	[2]	8.963±0.006	...	<1.0E-99
Category B						
4U 1538-522	3.72839	...	[2]	3.728±0.001	...	1.43E-2
LMC X-4	1.40841	30.4	[1]	...	30.34±0.03	5.63E-52
SMC X-1	3.892116	~55	[1,3]	3.892±0.001	58.6±0.2	9.95E-2,3.37E-7

References. — [1] Wijers & Pringle (1999) [2] Bildsten et al. (1997) [3] Friedhorsky & Holt (1987) [4] Rubin et al. (1996) [5] Finger et al. (1999) [6] Singh et al. (2002) [7] Wilson et al. (2002) [8] Brocksopp et al. (1999a)

^aDetected only in FFTs of single step data

Table 7. Earth Occultation Imaging Results for Category B Sources

Source Name	# of Days	Channel/Position Results
SMC X-1	14	visible in all 3 channels, some positions
NGC 1275	14	visible in all 3 channels, some positions
XPER	15	slight indication of excess in some positions
LMC X-4	15	strong in ch 1-2, visible in 3, most positions
4U 0614+091	13	visible in ch 1 when in center of grid
EXO 0748-676	13	strong in ch 1-2, most positions, sometimes in ch 3
Vela pulsar	11	no convincing image – noisy sky around source
1E 1145-614	14	slight indication of excess in some positions, ch 1
3C 273	11	visible in some positions, strongest in ch 3
4U 1323-619	13	strong in most positions, chs 1-3
NGC 5548	13	no convincing image
PSR 1508-59	15	visible in all 3 channels, some positions
4U 1538-422	12	visible only in center of grid
4U 1626-673	10	visible in some positions, ch 1 only
4U 1636-536	10	visible in some positions, ch 1-3
GX 349+2	13	visible in most positions, ch 1-2
4U 1702-429	11	confusion with 4U 1705-440, ch 1-3
4U 1705-440	12	strongly visible most positions - confusion with 4U 1702-429
GX 9+9	15	no convincing image
GX 354+0	14	visible most positions, ch 1-3
GX 3+1	14	visible in center ch 1-3, else sky too noisy
4U 1812-12	11	bright, distinguishable from GX 17+2 in ch 2
4U 1820-303	14	no convincing image
H 1822-371	15	visible some positions, ch 1-2, not compact
LS 5039	12	slight excess in some positions, ch 1-3
SS 433	12	slight excess in some positions, ch 1
4U 1916-053	13	no convincing image
4U 2127+119	14	no convincing image
CYG X-2	14	no convincing image

A. Special Notes on Transient Activity in the BATSE Database

The available literature on the results of BATSE detection and monitoring for transient sources is not always complete. The difficulty of identifying new sources, in particular, directly stems from the limited spatial resolution and sensitivity of the BATSE EOT. As discussed in Harmon et al. (2002), our ability to spatially resolve point sources on the sky is limited by the geometry of the Earth's limb at the time of measurement, coupled with the slow change of this geometry (\sim days) as the spacecraft orbit precesses. This is compounded by the sometimes brief duration of transient outbursts. Some special notes are provided here regarding activity that was not as well understood at the time of its occurrence.

EXO 1846-031, GS 1843+00 and GS 1845-024

These sources, occupying a relatively small (few-degree) region on the sky, were all detectable at various times in the BATSE database. First noted in a deep search of the BATSE database using epoch folding, a source with a 241 day period was given the name GRO J1849-03 (Zhang et al. 1996a, 1996b). At that time, the regularity of the outbursts suggested that GRO J1849-03 was a HMXB, but pulsations were not detected. Later sensitivity enhancements in BATSE pulsar analysis, however, revealed 94-s pulsations detected at times of outbursts. This observation, combined with a pulse arrival timing analysis that revealed an orbital period of 242.18 ± 0.01 days, identified GRO J1849-03 with GS 1845-024 (Finger et al. 1999). A more precise positional confirmation was also made with the Wide Field Camera on *BepiSax* (Soffitta et al. 1998).

BATSE observed short-lived transients with a hard spectrum in 1993 (Harmon et al. 1993) and slightly less than a year later (Zhang et al. 1994) in this same region of the sky. The spectral shape, both times, was reminiscent of a BHC. Unfortunately, the limb geometry was not sufficiently to locate the source to more than a few degrees in one direction within the few days that the outbursts were observable. A follow-up observation two weeks after the

1994 outburst did not indicate any unusual optical activity in the vicinity of EXO 1846-031 (Grindlay, Garcia, & Zhao 1994). The BATSE error boxes were consistent with the reported discovery location of the black hole transient EXO 1846-031 (Parmar et al. 1993), and so we tentatively identified the outbursts with this source (Zhang et al. 1994).

In Table 3, we include the regular outbursts of GS 1845-024, a single outburst of the pulsar GS 1843+00 (Wilson et al. 1997b) and the two outbursts with hard spectra attributed to EXO 1846-031.

Galactic Center Transient GRS 1739-278

A transient source was first detected on 16 Mar 1996 with *Granat*/Sigma (Paul et al. 1996) in the Galactic center region with a hard spectrum. A study of its properties with *Granat* (Vargas et al. 1997) indicated that the source, named GRS 1739-278, probably contained a black hole. Because of its proximity ($\sim 1^\circ$) to a bright source discovered with BATSE only a few months earlier (GRO J1744-28 or “bursting pulsar”) (Fishman et al. 1995; Kouveliotou et al. 1996), it was difficult to separate the fluxes from the two sources. The first observations showing a clear detection of GRS 1739-278 by RXTE/ASM was on TJD 10143 (1 Mar 1996), although a single measurement exists on TJD 10101 (19 January 1996) that indicates about a 3σ detection. Greiner, Dennerl, & Predehl (1996) made a follow-up observation to the *Granat* discovery on TJD 10158 (18 Mar 1996) to get a more accurate location for the X-ray counterpart, and discovered a substantial X-ray scattering halo. Due to the delay in arrival time of the scattered photons, the ROSAT results implied that the source could have first appeared as early as 1995 November-December. A very sparsely sampled BATSE light curve for GRS 1739-278 indicated the source was visible as early as ~ 10035 (14 Nov 1995) at a level of ~ 200 mCrab in the 20-100 keV band, and decaying below the source confusion limit (~ 50 mCrab) in the Galactic center region by ~ 10497 (18 Feb 1997). These beginning and ending dates for the outburst were entered into the flare database and Table 3.

RXTE Transients XTE J1550-564, XTE J1859+226, XTE J1118+480, XTE J1543-568, XTE J0111-7317

and V4641 SGR (*Sagittarius*)

These transients were discovered in outburst by RXTE during the final years of the CGRO mission. Several of these transients were quite bright and reached a Crab or more in the BATSE energy bandpass. The RXTE/ASM, which was designed to quickly locate and monitor new transients, generally was able to report these outbursts rapidly, sometimes even before BATSE data containing the same transient were received for processing. It is interesting scientifically, as well as important to our accounting of bright sources, to examine archival data for these transients, especially prior to the launch of RXTE in 1995.

As part of the deep sample, light curves were generated for XTE J1550-564, XTE J1859+226, XTE J1118+480, XTE J1543-568, XTE J0111-7317 and V4641 SGR. All showed detectable outbursts as recorded in Table 3. Examination of light curves from the beginning of the CGRO mission in April 1991 prior to the known outbursts occurring at various times after December 1995 did not show any emission more than five successive days greater than ~ 100 mCrab intensity in the 20-100 keV band. Outbursts of lesser duration and intensity could possibly be present in the dataset, but require more in-depth analysis.

B. Energy Channel Mapping Scheme, Flux Conversion Factors and Data Problems

Pulse height data from the BATSE large area detectors were normally acquired into 128 high energy resolution (HER) channels. Due to telemetry limits, the HER data were mapped into 16 broader energy channels and read out at 2.048s to create the continuous (CONT) background data. EOT measurements were made with the CONT dataset. Normally the CONT channel bin edges were kept to a constant set of values, that, coupled with the LAD gain control, kept the effective energy loss pulse height response per channel extremely stable. However, on rare occasions, the 128 to 16 channel mapping was changed to accommodate a greater energy dispersion when observations of sources with softer spectra and possible

line features were desired (e.g., accreting pulsars or soft gamma-ray repeaters). Table B1 shows several mapping schemes (numbered 0, 1, 2, 3, 4a and 4b) that were used during the mission and the times in which these were applied. From column 2, it can be seen that scheme 2 was used about 90% of the time.

Schemes 2, 3, 4a and 4b had in common several of the same HER channels for which we could obtain 4-energy band data spanning changes in the HER to CONT channel mapping. Using the Crab fluxes as a standard candle, a tool was created for which the flux of any source relative to the Crab could be generated in the energy bands 20-40, 40-70, 70-160 and 160-430 keV. The Crab relative rates quoted in Tables 4 and 5 can be converted to photon number per keV ($\text{ph cm}^{-2}\text{s}^{-1} \text{ keV}^{-1}$) or energy flux per band using the multipliers given in Table B2. Note that this method of four-band conversion to Crab relative rates cannot be used for schemes 0 or 1, and so data before TJD 8406/81139 and for the brief intervals TJD 8807/8279 - 8809/64510 and 8812/65817 - 8812/66102 cannot be treated in this manner.

Table B3 is a list of days when unusual or anomalous events occurred during the CGRO mission and no Earth occultation measurements could be extracted. These events produced gaps in most or all source flux histories at the given times. Routine events causing loss of measurements such as source interference, exceeding the critical angle for Earth occultation, or telemetry gaps are not included. Table B3 gives the times, data condition reported, and the cause of the anomaly.

C. Comparison to JPL Enhanced BATSE Occultation Package (EBOP)

Skelton et al. (1994), Ling et al. (1996, 2000) and co-workers at the Jet Propulsion Laboratory developed an Earth occultation software package over a period of several years with the intent to generate higher sensitivity results than can be obtained with the treatment described in Harmon et al. (2002). The JPL package is known as the Enhanced BATSE Occultation Package (EBOP) and has been applied to

BATSE data independent of the efforts at MSFC. Ling et al. (2000) published a compendium of measurements (also called a catalog) for the 1991 May to 1994 October epoch. We feel it is very important to compare the results from EBOP with those of this work, since there are significant discrepancies between what we report and what can be found in Ling et al. (2000).

Primarily, there are two major differences between the JPL method and the method used here. First, EBOP uses a semi-physical model for the detector background counting rates. The model is based on expected contributions of low-energy gamma-ray fluxes local to the low Earth orbit (LEO) environment. These include cosmic ray secondary radiation and activation products from orbital passes through radiation fields in LEO. The JPL global background model consists of a mix of the local radiation components and a combination (determined by the fit) of the BATSE spectroscopic detector (Fishman et al. 1989a,b) counting rates as a predictor of the low-energy background in the LADs. Secondly, the extraction of source signals is usually performed in one-day segments, with a single fit including terms for *all* sources in the EBOP catalog with no *a priori* assumptions of their intensity. The main goal of this work is increase sensitivity by fitting much longer intervals of background data than the four minutes typically used in our work, which does not require a sophisticated background model.

In Table C1, we compare selected results for a few sources from the deep sample in Table 4 and the EBOP catalog (Ling et al. 2000). To best illustrate the comparison, we selected sources over a range of flux intensities, as well as to pick sources that did not show a large degree of variability on timescales of months to years. Table C1 shows fluxes in three selected energy bands with centroid energies that overlap in EBOP and the Table 4 deep sample. Results from the deep sample are quoted with and without systematic error corrections. The EBOP results are reported as minimum and maximum average fluxes for several ~ 400 day intervals in Table 3 of Ling et al. (2000). The deep sample results are the 9.1y averages from this work (Table 4) converted from mCrab

to photon flux with the multiplicative factors from Table B2. For the Crab, the two methods give very similar results, and confirm the cross-check of the of the two methods from Ling et al. (2000). Sources of moderate intensity, such as 4U 1700-37 and NGC 4151, show significant discrepancies, particularly for the highest of the three energy bands. For relatively weak sources at the few mCrab level, such as the LMXB Circinus X-1, the supernova remnant PSR 1509-58, and the Seyfert Galaxy NGC 1275, our average fluxes are roughly an order of magnitude less than the EBOP results. For Sct X-1, we only show upper limits ($<2\sigma$) (corrected for systematic error), whereas the JPL method yielded significant broadband emission at least an order of magnitude higher.

To make sure that the time interval for which the averages were constructed was not a major factor in the comparison, we generated long term spectra for TJD 8393-8800 as was done in Ling et al. (2000). Figures 17a and 17b show the broad-band spectra of Cir X-1 and PSR 1509-58 using the MSFC method with no systematic error correction applied, the EBOP results from Ling et al. (2000), and the Table 4-band average fluxes with systematic error corrections. The broad-band spectra from the JPL and MSFC methods are considerably different over most of the sensitive energy range of the LADs. Differences between the broad-band MSFC data and the 4-band averages for Cir X-1 are mostly caused by the large systematic error correction for that source. The findings reflect the same conclusions made using Table C1.

Ling et al. (2000) discuss sources of error for the Earth occultation analysis specific to EBOP in some detail and point out that the high energy fluxes they see for some sources such as Sct X-1 and NGC 1275 should be viewed with caution. Since we observe considerably lower fluxes for these and other sources in the 160-430 keV band, it suggests that their concern could be justified.

Here we point out possible reasons for the discrepancy between our work and the EBOP results. One possibility concerns unaccounted for components in the gamma-ray background for which the LADs

have significant sensitivity, but are not included in the JPL model. We have found that, when fitting the background near occultation steps for more than a few minutes, there is an increased likelihood for slow, very significant variations to cause the measured background to be considerably different from the assumed model. These variations are not associated in any way with occultation steps. Such effects could be high energy diffuse emission from the Galactic plane or unusual local background variations on specific days (e.g., solar activity or electron precipitation events) that can affect the computed level of the background in the high energy (a few hundred keV) data. These variations from the model can be transferred to source terms which are fit simultaneously with the background. Another possibility is the assumed set of sources used by the JPL method. JPL used a set of 64 sources, all of which are fit simultaneously, regardless of any intensity or time information. Our catalog consisted of 179 sources, however, no more than 10 sources were fit simultaneously in the MSFC method, and usually only 1-3 per 4-minute fitting window were typical. This reduces the tendency toward large scale coupling between source terms, and presupposes that we have partial information about what sources a detector is likely to be seeing. This may not explain anomalously large fluxes at high energy in the JPL data, but it can help to explain the tendency to yield fluxes higher than the MSFC method for lower intensity sources. Although a finite source set is also a problem for the MSFC method, the strategy was to iteratively improve characterization of the sources in the catalog based on average brightness, times of transient activity, and to use a source set taken from published catalogs. Our method therefore yields improved results by having a better knowledge of source activity each time a pass through the dataset is performed.

Table A1. LIST OF ACRONYMS AND ABBREVIATIONS

Acronym or Abbrev.	Meaning
AGN	active galaxy or galactic nucleus
ASM	All-Sky Monitor
BATSE	Burst and Transient Source Experiment
BH or BHC	black hole candidate
BL Lac	BL Lacertae object
CGRO	<i>Compton Gamma Ray Observatory</i>
CH	channel
CONT	large area detector continuous data
CV	cataclysmic variable
DN	dwarf nova
EBOP	JPL Enhanced BATSE Occultation Package
EGRET	Energetic gamma-ray Experiment Telescope
EXIST	Energetic X-Ray Imaging Survey Telescope
EOT	Earth occultation technique
FFT	fast Fourier transform
GCR	Galactic center region
HEAO	<i>High Energy Astronomy Observatory</i>
HER	high energy resolution
HISGEN	BATSE photon flux history generator
HMXB	high mass x-ray binary
INTEGRAL	<i>International Gamma-Ray Astrophysics Laboratory</i>
JPL	Jet Propulsion Laboratory
LAD	BATSE large area detector
LMXB	low mass x-ray binary
MSFC	Marshall Space Flight Center
NS	neutron star
OCCSYS	automated data flagging software
OF_W	MSFC EOT flux history generator
OTTB	optically thin thermal bremsstrahlung spectral fitting model
PL	power law spectral fitting model
PSR	pulsar
QSR	quasar
ROSAT	German X-Ray Roentgen Satellite
RS CVn	eruptive variable of RS Canum Venaticorum type.
RXTE	<i>Rossi X-Ray Timing Explorer</i>
S/C	spacecraft
SGR	soft gamma-ray repeater
SNR	supernova remnant

Table A1—Continued

Acronym or Abbrev.	Meaning
SOD	seconds of day
SOI	source of interest
SY(1 or 2)	Seyfert galaxy, type 1 or 2
TJD	Truncated Julian Date (Julian Date - 2,440,000.5)
UVS	ultraviolet source
XRS	X-ray source

Table B1. BATSE LAD 128-Channel to 16-Channel Mapping (Lookup Table)

Scheme #	%Time	TJD (Days)	SOD (secs)	CONT energy channel															
				0	1	2	3	4	5	6	7	8	9	10	11	12	13	14	15
0	0.2	8361	0	0	13	15	17	19	22	25	30	37	49	64	74	89	100	111	125
1	1.2	8367	0	0	9	11	14	18	22	26	30	38	49	65	75	90	98	106	122
2	12.0	8406	81139	0	7	9	11	14	18	23	28	36	49	65	75	90	98	106	122
0	0.1	8807	8279	0	13	15	17	19	22	25	30	37	49	64	74	89	100	111	125
2	0.1	8809	64511	0	7	9	11	14	18	23	28	36	49	65	75	90	98	106	122
0	0.0	8812	65817	0	13	15	17	19	22	25	30	37	49	64	74	89	100	111	125
2	17.7	8812	66103	0	7	9	11	14	18	23	28	36	49	65	75	90	98	106	122
3	0.1	9400	59319	7	9	11	14	18	20	23	25	28	32	36	49	65	75	90	122
2	19.3	9419	60041	0	7	9	11	14	18	23	28	36	49	65	75	90	98	106	122
4a	3.5	10062	71275	122	7	8	9	10	11	12	14	16	18	23	28	36	49	75	90
2	8.6	10178	85302	0	7	9	11	14	18	23	28	36	49	65	75	90	98	106	122
4b	1.2	10465	83335	0	7	8	9	10	11	12	14	16	18	23	28	36	49	75	122
2	14.4	10504	80991	0	7	9	11	14	18	23	28	36	49	65	75	90	98	106	122
4b	2.1	10983	71907	0	7	8	9	10	11	12	14	16	18	23	28	36	49	75	122
2	0.1	11053	51166	0	7	9	11	14	18	23	28	36	49	65	75	90	98	106	122
4b	0.1	11055	54394	0	7	8	9	10	11	12	14	16	18	23	28	36	49	75	122
2	18.2	11085	74663	0	7	9	11	14	18	23	28	36	49	65	75	90	98	106	122

Table B2. Conversion Factors for 4-Energy Band Data in Table 4

HER Channels	Energy Band (keV)	Log Avg (keV)	Multiplier ($\text{ph cm}^{-2}\text{s}^{-1}\text{keV}^{-1}$)	Multiplier ($\text{ergs cm}^{-2}\text{s}^{-1}$)
7 - 11	20-40	28.3	8.508×10^{-6}	7.567×10^{-12}
11 - 18	40-70	52.9	2.323×10^{-6}	5.830×10^{-12}
18 - 36	70-160	105.8	5.514×10^{-7}	8.079×10^{-12}
36 - 75	160-430	262.3	6.261×10^{-8}	6.887×10^{-12}

Note. — lower HER channel is the lower energy edge of the corresponding CONT channel and the higher HER channel is the corresponding upper edge of the corresponding CONT channel as given in Table B1. Example: HER channels 7 - 11, corresponds to CONT channels 1 - 2 in scheme 2 and CONT channels 1 - 4 in scheme 4a.

Table B3. List of Mission Anomalies/Data Loss Events Affecting BATSE Earth Occultation Results

TJD/SoD	Condition	Cause of Anomaly
8449/05500-12000	some LAD gains out of balance	SAA passage w/HV on
8490/03000-35000	some LAD gains out of balance	SAA passage w/HV on
8588	observing plan read error	?
8741/80355 - 8742/11519	data crash	flight software problem
8742/63376 - 8742/83566	data crash	flight software problem
8807/03065-66377, 68578-71280	HV off	S/C power supply problem
8807/66300 - 8809/53160	LAD gains out of balance	S/C power supply (cont.)
8812/65733-65964, 68510-71490	HV off	change S/C power supply
8812/65960-68512	LAD gains out of balance	S/C power supply (cont.)
9075/57503-62797	data crash	flight software problem
9075/79431 - 9076/09796	data crash	flight software problem
9110/84820 - 9112/54665	HV off	reboost activities
9113/81403 - 9115/53135	HV off	reboost activities
9152/84296 - 9154/16964	HV off	reboost activities
9336/49077-65666	HV off	reboost activities
9336/65666-75000	some LAD gains out of balance	reboost activities
10014/03349-15300	LAD gains out of balance	SAA passage w/HV on
10014/15300-65700	LAD 3 gain out of balance	SAA passage w/HV on; LAD 3 reset
10014/15300 - 10016/10008	LAD 6 gain out of balance	SAA passage w/HV on; HV reset
10416/16897-19200	bad rates	recovery from flight software upset
10417/70332-71000	bad rates	recovery from flight software upset
10416/16897 - 10418/69320	LAD gains slightly out of balance	flight software upset
10900 - 11690	LAD 7 gain decreased	AGC caused HV to reach maximum value
11001/11000-50000	LAD gains out of balance	SAA passage w/HV on
11001/50000 - 11002/30400	LADs 0,6 gains out of balance	SAA passage w/HV on
11002/30400 - 11003/46570	LAD 0 gain out of balance	SAA passage w/HV on
11003/46570-50500	LADs 0,2,6 gains out of balance	HV reset
11046/74756 - 11047/28002	data lost	bad solar ephemeris
11047/30897-71816	data lost	bad solar ephemeris
11047/71816 - 11050/77609	HV off	bad solar ephemeris
11307/04563-31857	data lost	high-gain antenna problems
11354/03716 - 11359/72432	data lost	high-gain antenna problems
11518/55813 - 11522/00089	data lost	gyro failure

Table C1. Comparison of JPL EBOP and MSFC Catalog Results

Source	Energy Band (keV)	EBOP ph cm ⁻² s ⁻¹ keV ⁻¹	Energy Band (keV)	MSFC ph cm ⁻² s ⁻¹ keV ⁻¹	MSFC/w cor. ph cm ⁻² s ⁻¹ keV ⁻¹
CRAB	45-55	$2.58-3.10 \times 10^{-3}$	40-70	2.36×10^{-3}	2.38×10^{-4}
	98-123	$5.10-5.60 \times 10^{-4}$	70-160	5.61×10^{-4}	5.64×10^{-4}
	230-313	$6.14-7.01 \times 10^{-5}$	160-430	6.47×10^{-5}	6.50×10^{-5}
4U1700-37	45-55	$4.89-5.39 \times 10^{-4}$	40-70	3.49×10^{-4}	3.48×10^{-4}
	98-123	$3.99-4.34 \times 10^{-5}$	70-160	3.52×10^{-5}	3.51×10^{-5}
	230-313	$1.70-4.44 \times 10^{-6}$	160-430	8.39×10^{-7}	8.39×10^{-7}
NGC4151	45-55	$9.93-16.1 \times 10^{-5}$	40-70	9.80×10^{-5}	9.80×10^{-5}
	98-123	$2.18-2.88 \times 10^{-5}$	70-160	2.04×10^{-5}	2.04×10^{-5}
	230-313	$2.69-4.08 \times 10^{-6}$	160-430	1.31×10^{-6}	1.31×10^{-6}
CIRX-1	45-55	$6.66-7.87 \times 10^{-5}$	40-70	8.13×10^{-6}	$<6.97 \times 10^{-6}$
	98-123	$1.91-2.48 \times 10^{-5}$	70-160	1.87×10^{-6}	$<1.65 \times 10^{-6}$
	230-313	$4.99-7.18 \times 10^{-6}$	160-430	$<2.69 \times 10^{-7}$	$<3.44 \times 10^{-7}$
NGC1275	45-55	$4.59-5.82 \times 10^{-5}$	40-70	6.97×10^{-6}	6.97×10^{-6}
	98-123	$1.26-1.70 \times 10^{-5}$	70-160	1.87×10^{-6}	1.87×10^{-6}
	230-313	$3.60-4.20 \times 10^{-6}$	160-430	2.50×10^{-7}	2.50×10^{-7}
PSR1509-58	45-55	$5.23-8.77 \times 10^{-5}$	40-70	2.37×10^{-5}	1.60×10^{-5}
	98-123	$1.48-2.61 \times 10^{-5}$	70-160	6.67×10^{-6}	4.52×10^{-6}
	230-313	$4.48-5.97 \times 10^{-6}$	160-430	8.95×10^{-7}	6.07×10^{-7}
SCTX-1	45-55	$1.53-1.67 \times 10^{-4}$	40-70	$<4.65 \times 10^{-7}$	$<2.32 \times 10^{-6}$
	98-123	$2.31-2.91 \times 10^{-5}$	70-160	$<1.49 \times 10^{-6}$	$<1.43 \times 10^{-6}$
	230-313	$4.26-5.50 \times 10^{-5}$	160-430	2.50×10^{-7}	$<4.51 \times 10^{-7}$

FIGURE CAPTIONS

Fig. 1.— Comparison of sensitivity (5σ) in photons $\text{cm}^{-2}\text{s}^{-1}\text{keV}^{-1}$ for BATSE, the 1977-1979 HEAO 1 A-4 sky survey (Levine et al. 1984) and the survey concept mission EXIST (Grindlay et al. 2001, 2003). Nominal energy bins for the two historical instruments are shown. An approximate representation of the Crab Nebula spectrum is shown for reference.

Fig. 2.— Aitoff-Hammer projection of the sky in Galactic coordinates showing the locations of the 179 sources in the BATSE Earth occultation catalog. The sources are labeled by object type.

Fig. 3.— (a) The *Compton Gamma Ray Observatory* showing placement of the BATSE detector modules. The detector modules on the top four corners of the spacecraft are numbered 0,2,4, and 6, proceeding clockwise from the detector facing the reader above the high gain antenna. Similarly the bottom four modules are numbered 1,3,5, and 7.(b) Major components of the BATSE detector modules (one of eight).

Fig. 4.— Flow diagram for processing of BATSE Earth Occultation data. Part (a) shows major processing steps beginning with components of the BATSE data archive on the far left (see text) leading to raw (counts per detector) rate histories. The raw histories were then converted to photon fluxes (20-100 keV) using the BATSE detector response, and also to intensities relative to the Crab Nebula flux in four flux bands (20-40, 40-70, 70-160 and 160-430 keV). Part (b) shows the final processing steps (epoch folding, FFT analysis, deriving average flux and uncertainty) in generating the tables in the catalog. The “Crab model” allows conversion of raw count rates directly into Crab relative fluxes (see text). Iteration $\#n$ refers to a single pass through the entire 9.1y dataset, which can be repeated to increase the size of the sky sample and to reduce systematic error.

Fig. 5.— Eclipse profiles in the 20-40 keV band for the five bright persistent HMXBs 4U 1700-377, Cen X-3, Her X-1, OAO 1657-415 and Vela X-1 in the BATSE dataset. Published ephemerides are used to eliminate fitting terms for these binaries while eclipses are in progress. Table 6 indicates the orbital periods used in epoch folding of the occultation flux histories shown in the figure.

Fig. 6.— Flux histories (20-100 keV, 1991 April - 2000 June) for four persistent black hole binary systems observed with BATSE.

Fig. 7.— Flux histories (20-100 keV, various times) for five transient black hole binary systems.

Fig. 8.— Flux histories (20-100 keV, 1991 April - 2000 June) for five low mass X-ray binary neutron star systems.

Fig. 9.— (a) Flux histories (20-100 keV, 1991 April - 2000 June) for six persistent accreting X-ray pulsars. For purposes of this catalog, a persistent source is defined as consistently exceeding $0.01 \text{ photons cm}^{-2} \text{ s}^{-1}$ (20-100 keV, $\sim 35 \text{ mCrab}$). Two of these systems GX 1+4 ($P_{\text{spin}} \simeq 120 \text{ s}$) and Her X-1 ($P_{\text{spin}} \simeq 1.24 \text{ s}$) have a low-mass companion, while the rest, Cen X-3 ($P_{\text{spin}} \simeq 4.8 \text{ s}$), GX 301-2 ($P_{\text{spin}} \simeq 681 \text{ s}$), OAO 1657-415 ($P_{\text{spin}} \simeq 10.4 \text{ s}$), and Vela X-1 ($P_{\text{spin}} \simeq 283 \text{ s}$) have a high-mass evolved supergiant companion. (b) Flux histories (20-100 keV, various times) for four transient X-ray pulsars. For purposes of this catalog, a transient source is defined as exceeding $0.01 \text{ photons cm}^{-2} \text{ s}^{-1}$ (20-100 keV, $\sim 35 \text{ mCrab}$) for an identifiable, but limited period of time. All four sources shown, EXO 2030+375 ($P_{\text{spin}} \simeq 42 \text{ s}$), GRO J1944+26 ($P_{\text{spin}} \simeq 15.8 \text{ s}$), GRS 0834-430 ($P_{\text{spin}} \simeq 12.3 \text{ s}$), and GS 1845-02 ($P_{\text{spin}} \simeq 94.8 \text{ s}$), have an identified Be star companion.

Fig. 10.— Flux histories (20-100 keV, 1991 April - 2000 June) for four galaxies with gamma ray active

nuclei.

Fig. 11.— Sky grid, consisting of 162 points, used for determination of location-dependent systematic error. Grid spacing is described in the text.

Fig. 12.— (Top) Measured averages in photons $\text{cm}^{-2}\text{s}^{-1}$ (20-100 keV) and (Bottom) width (in σ s or standard deviations) of the 9.1y flux histories for the grid locations shown in Fig. 11 as a function of Galactic longitude.

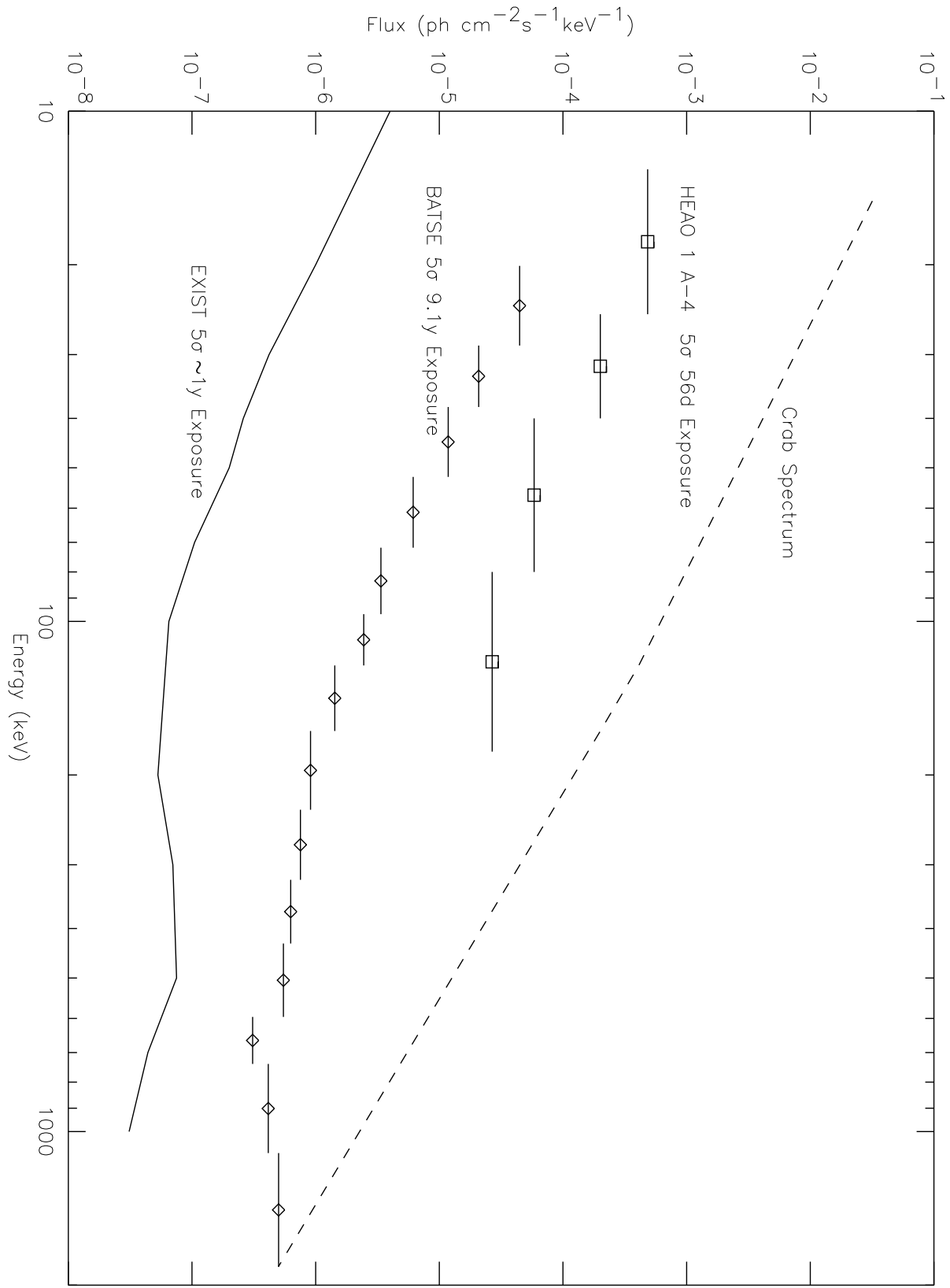
Fig. 13.— Distribution of 9.1y flux averages (20-100 keV) in order of brightness before (filled circles) and after correction with systematic error model. Symbols denote source categories used for the deep sample results.

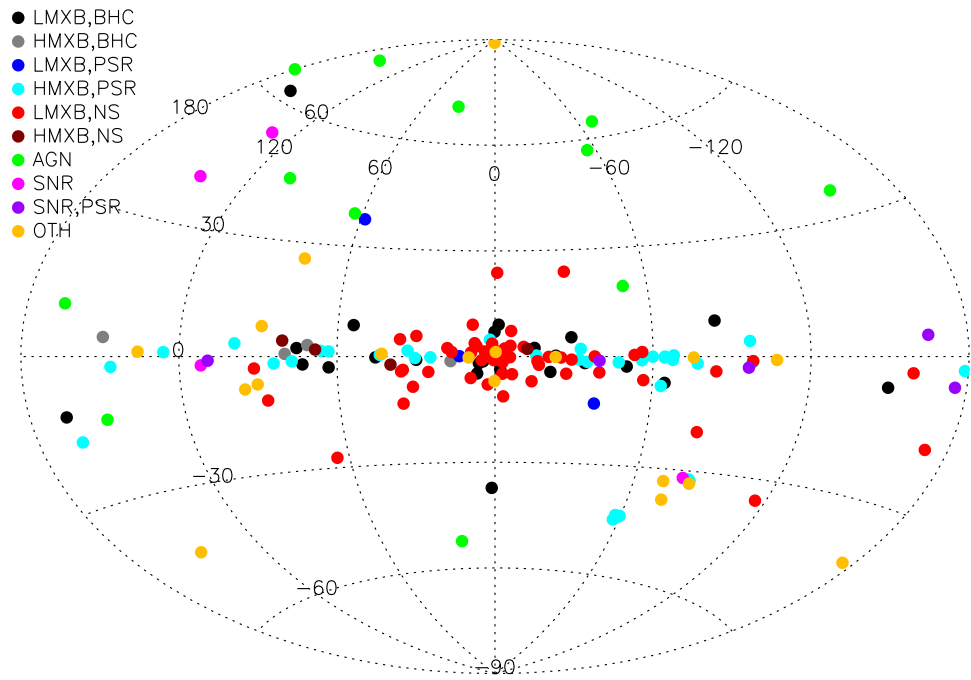
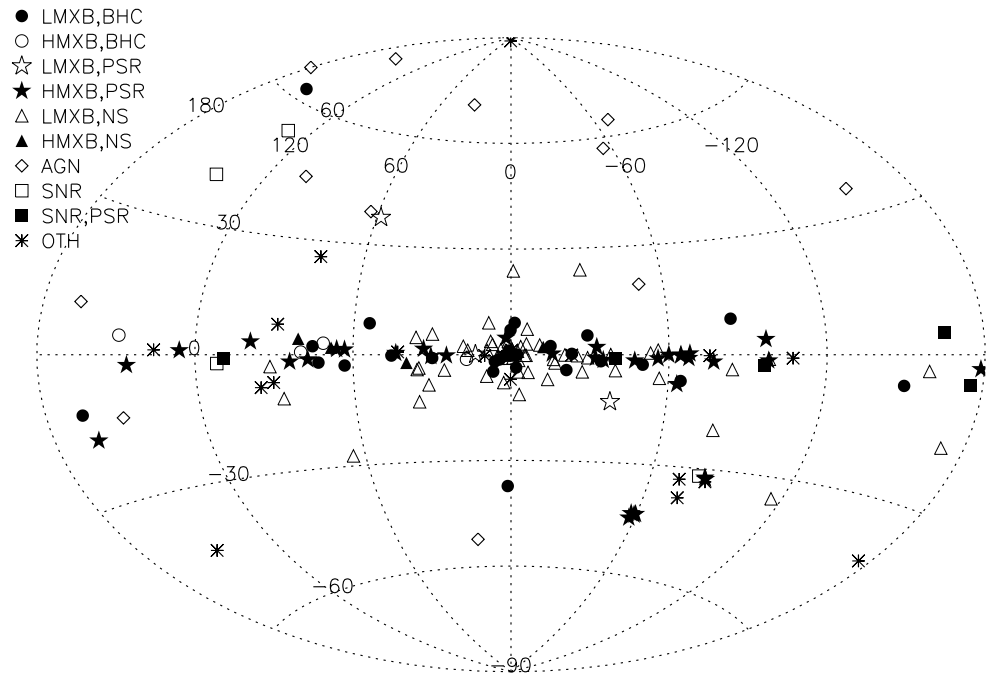
Fig. 14.— Histogram of fractional changes in flux significance of the deep sample when systematic errors were applied. The peak in the histogram at ~-0.3 corresponds to cases where the correction to the flux is zero, and the correction is dominated by the correction to the flux uncertainty. Systematic corrections to the average fluxes in Table 4 were only applied when the computed fractional change was between the two vertical dashed lines.

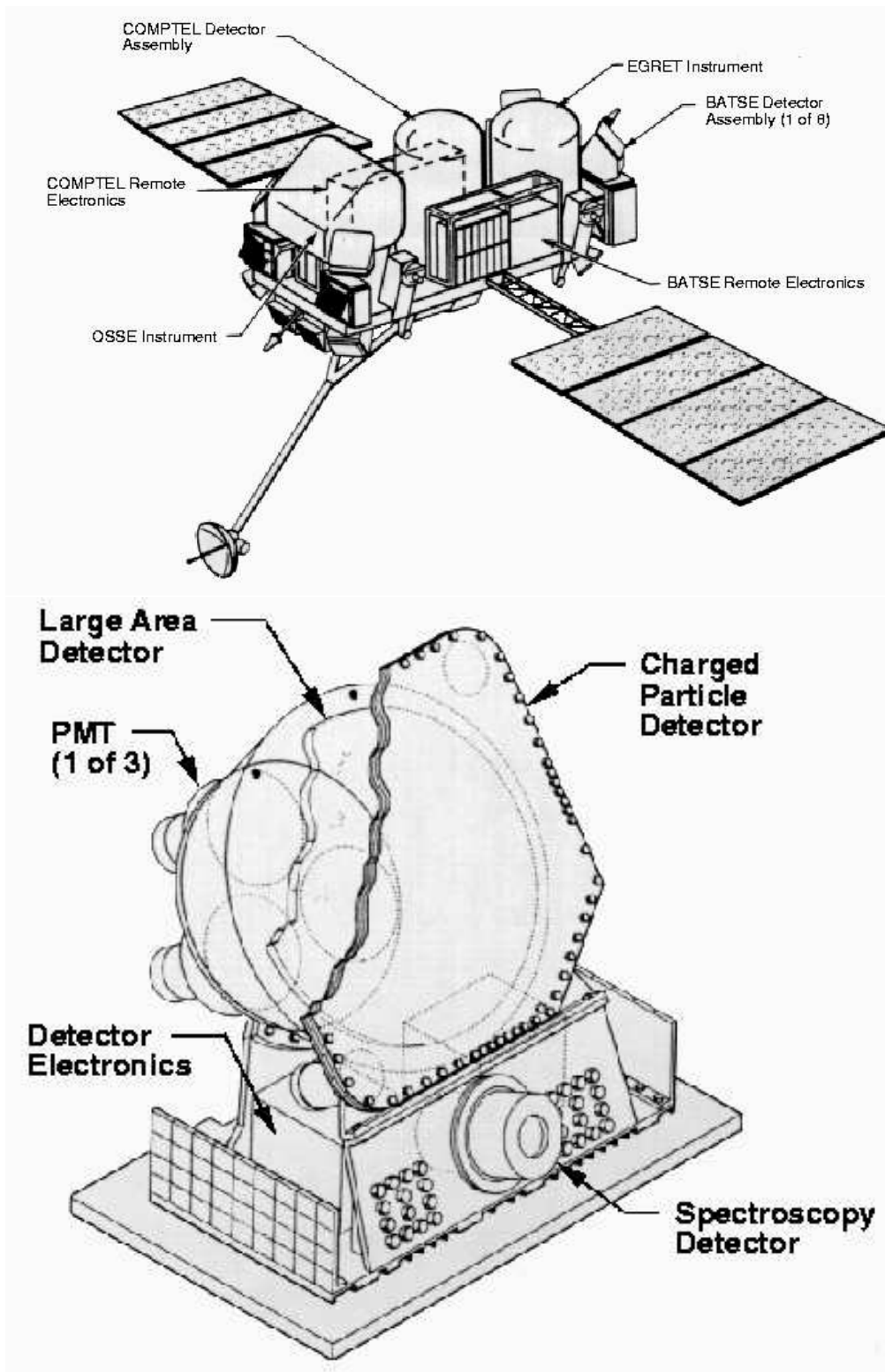
Fig. 15.— (a) Flux histories in the indicated energy band for the three category B sources (LMC X-1, SMC X-1 and 4U 1538-522) detected in the FFT analysis and epoch folded at the appropriate orbital periods as given in Table 6. We also show the epoch folded history result of the category C(B) source 4U 1907+097 detected in the BATSE EOT light curves by Laycock et al. (2003). (b) Flux histories in the indicated energy band for the two category B sources LMC X-4 and SMC X-1 epoch folded at the appropriate superorbital periods as given in Table 6. Note the effect of the superorbital period shift in SMC X-1, which smears the profile over long times.

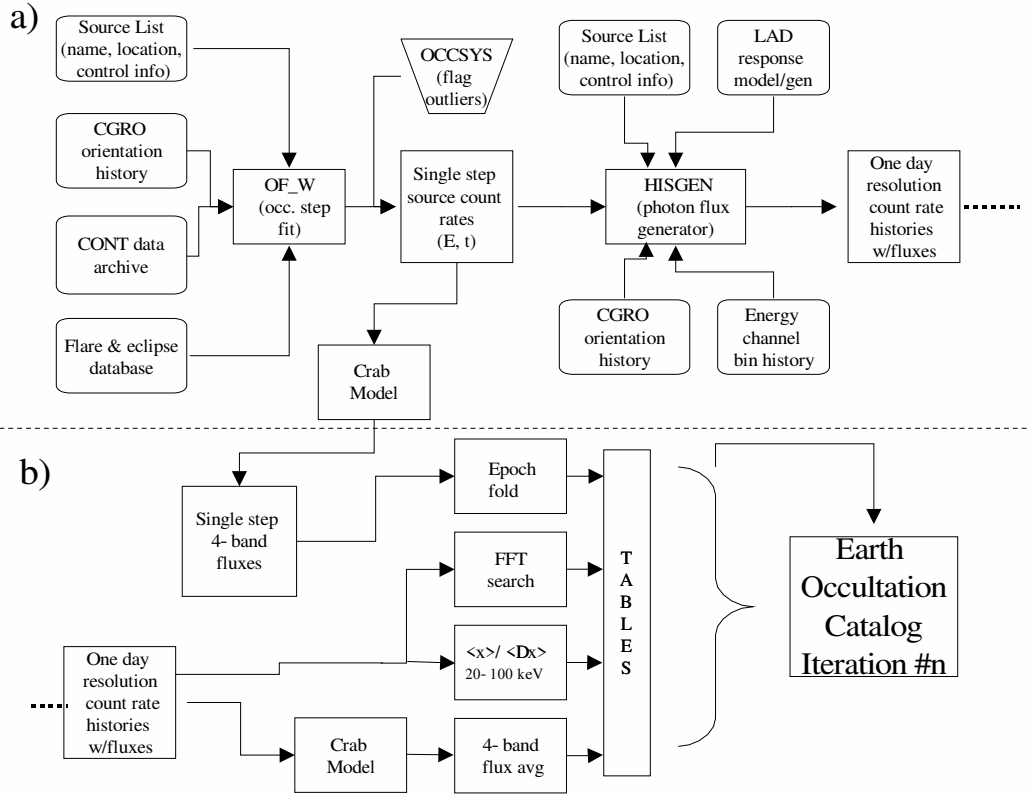
Fig. 16.— Images of selected category B sources: (a) 3C 273 (20-50 keV), an AGN, (b) 4U 1812-12 (Ser X-2) (20-50 keV), a LMXB, (c) PSR 1509-58 (50-100 keV), a SNR, and (d) EXO 0748-676 (20-50 keV), a LMXB.

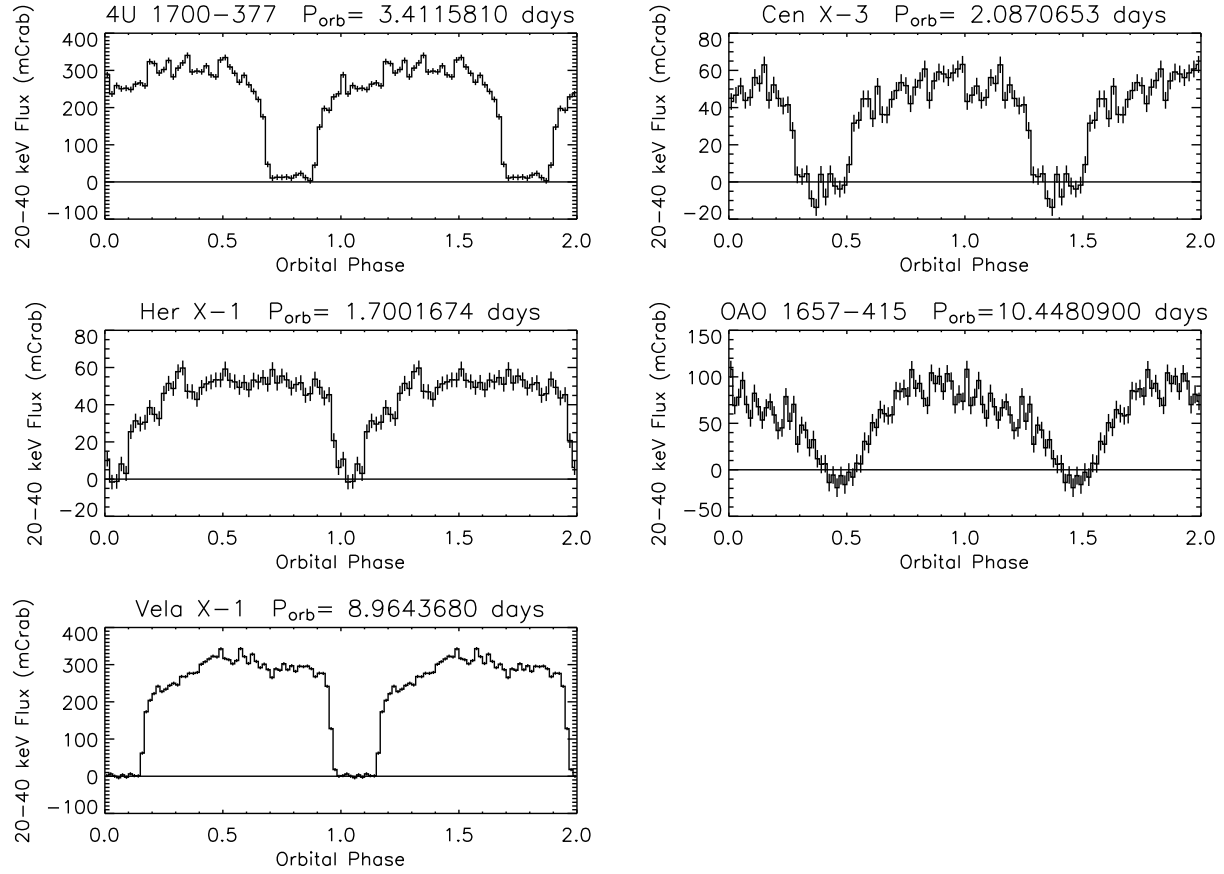
Fig. 17.— Broadband spectra for (a) the LMXB Cir X-1 and (b) the SNR PSR 1509-58 from the JPL EBOP (open squares) and MSFC EOT measurements (filled circles) for Truncated Julian Dates 8393-8800. For comparison, we also show the 9.1y average 4-band fluxes from Table 4, with systematic errors applied, and converted to photon fluxes using the multipliers in Table B2.

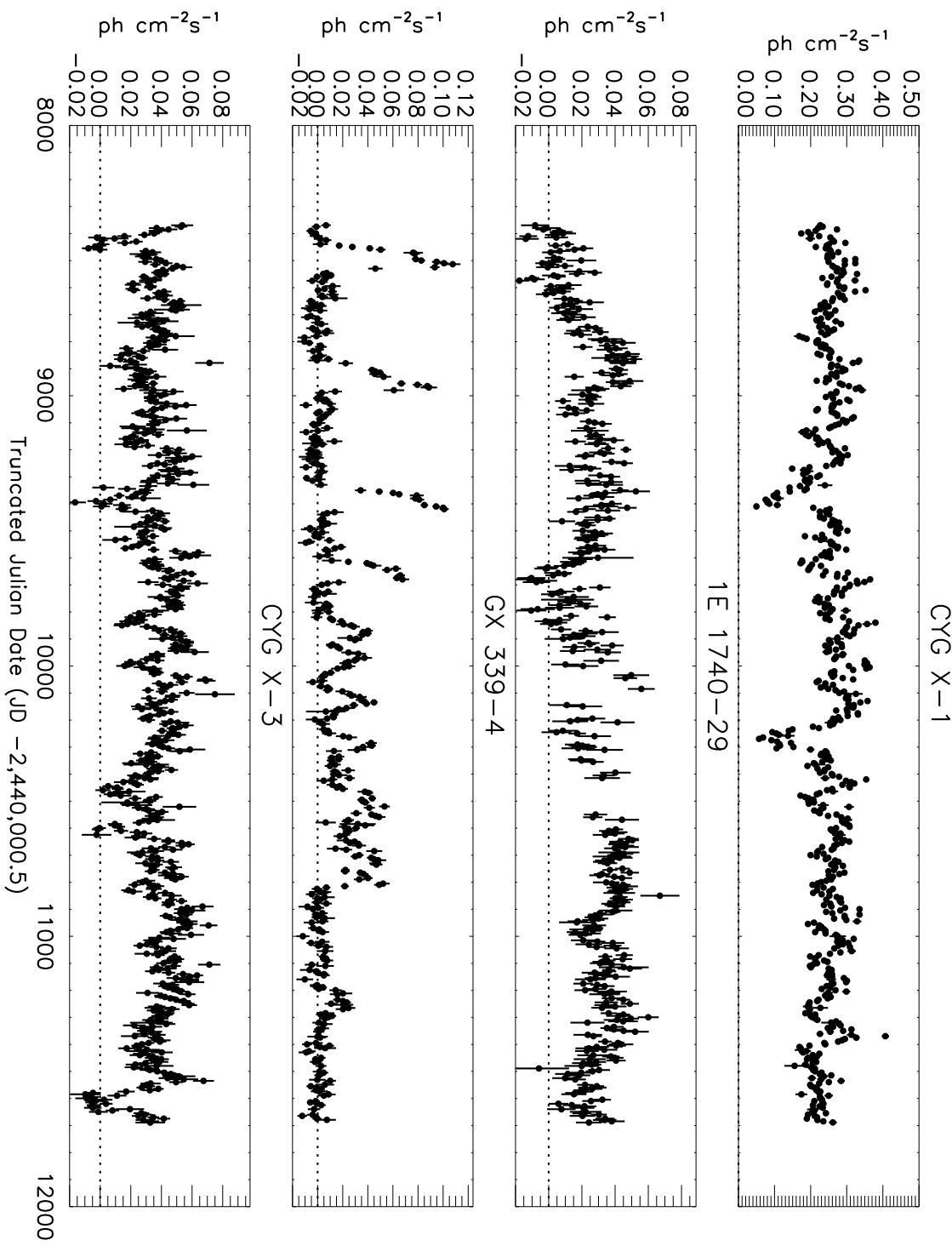




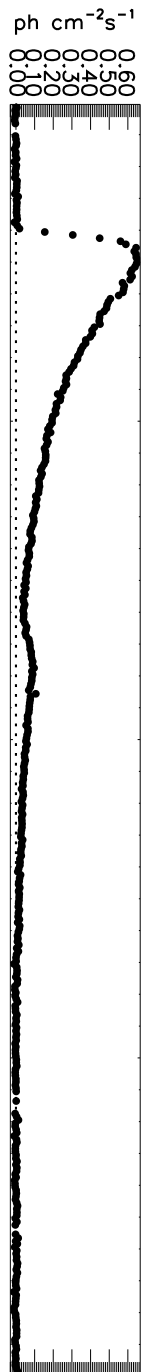




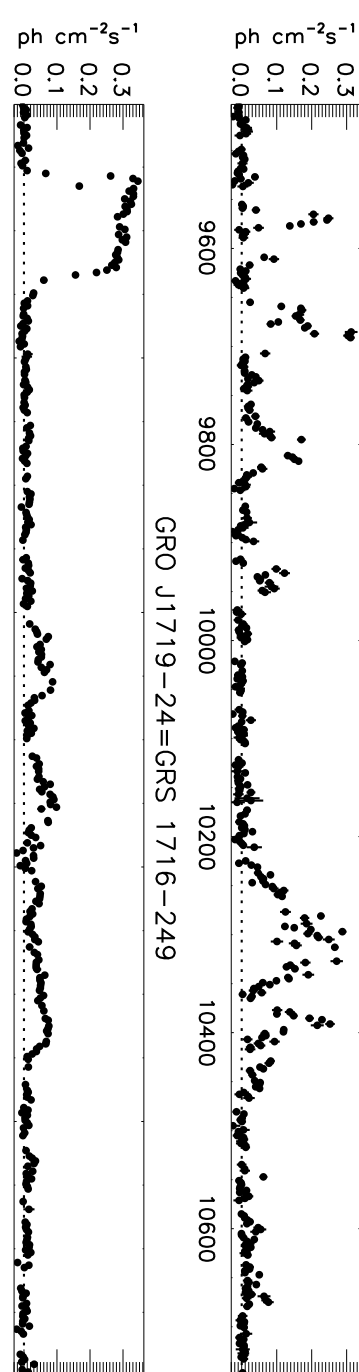




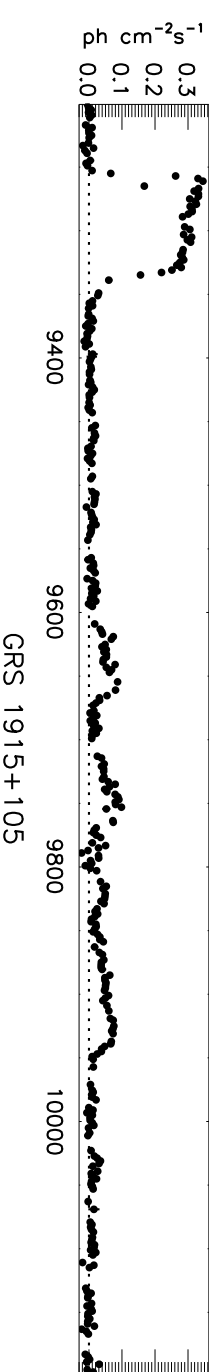
GRO J0422+32



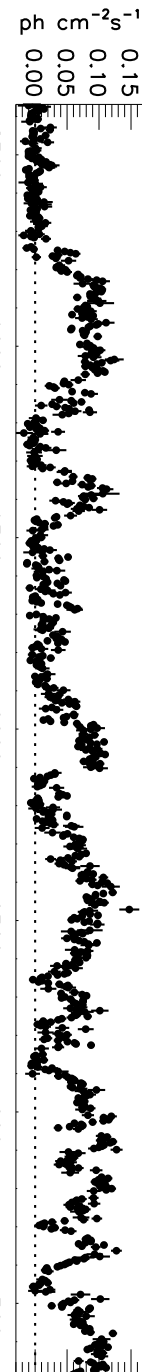
GRO J1655-40

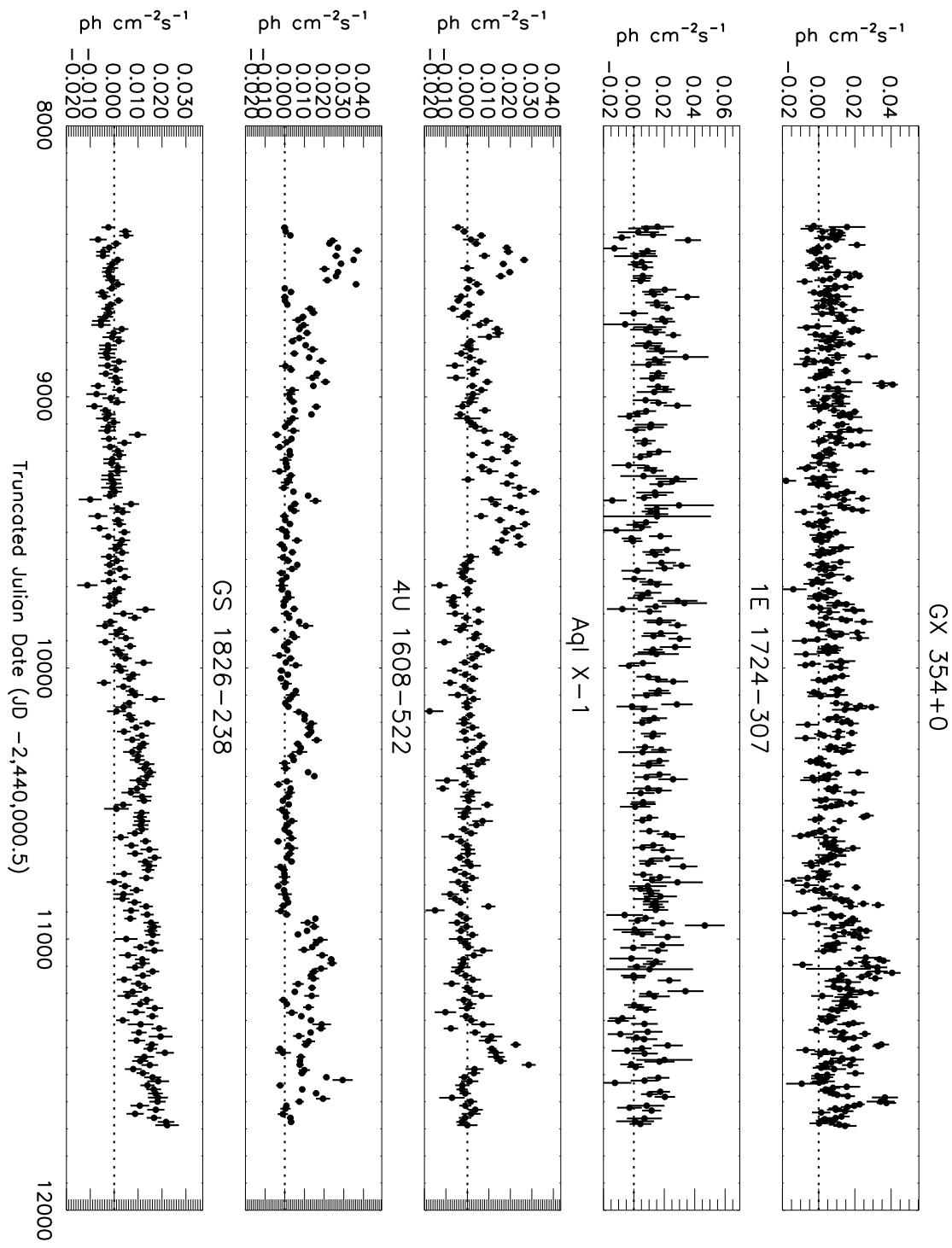


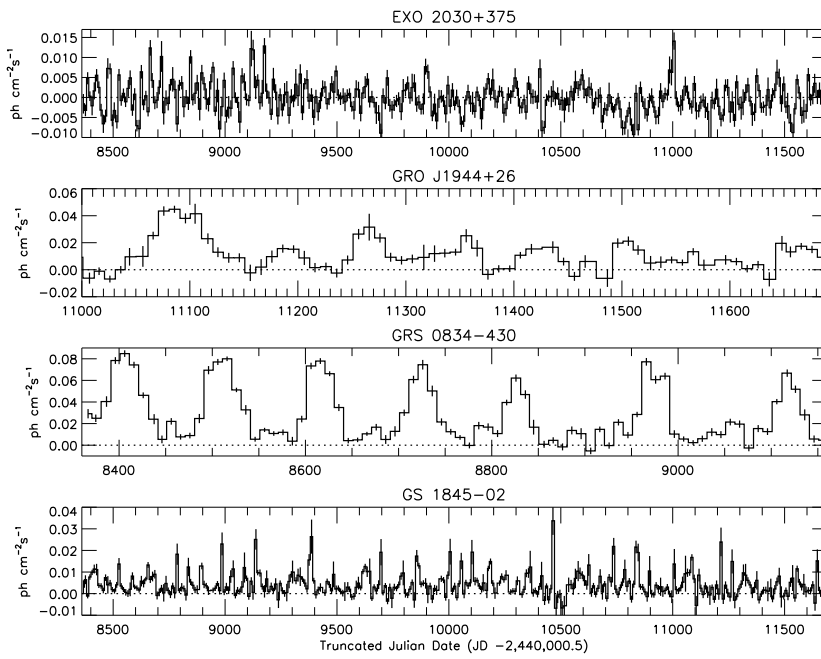
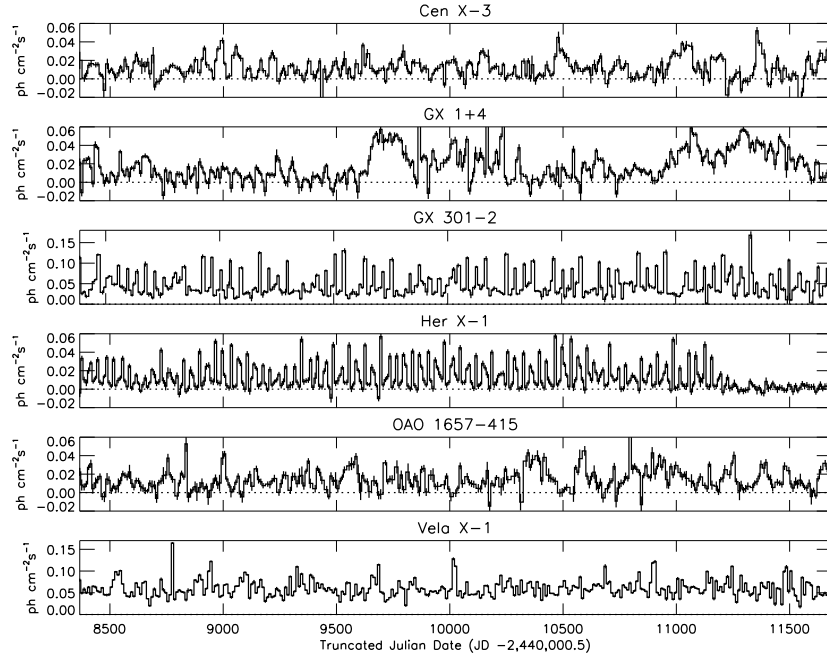
GRO J1719-24=GRS 1716-249

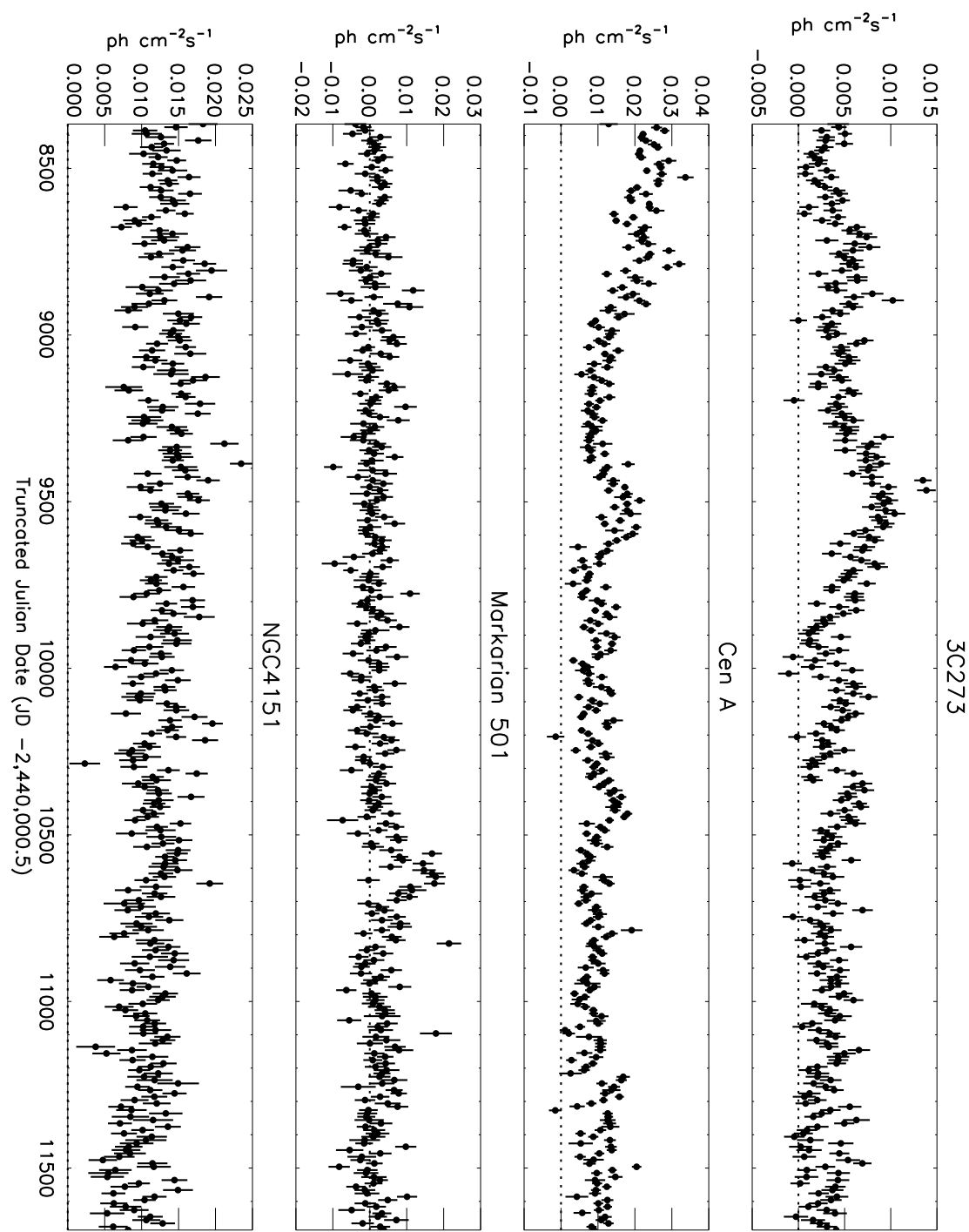


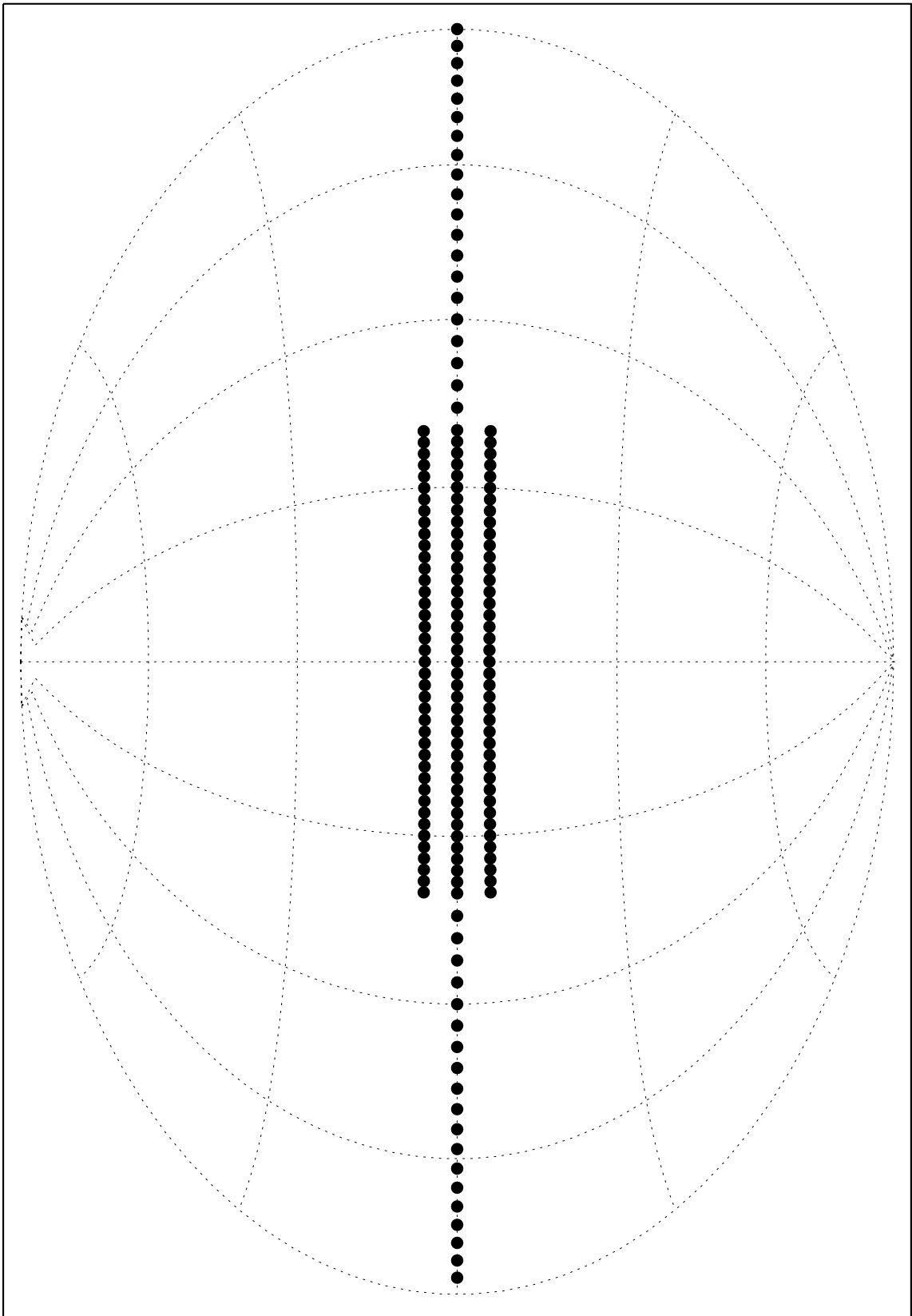
GRS 1915+105

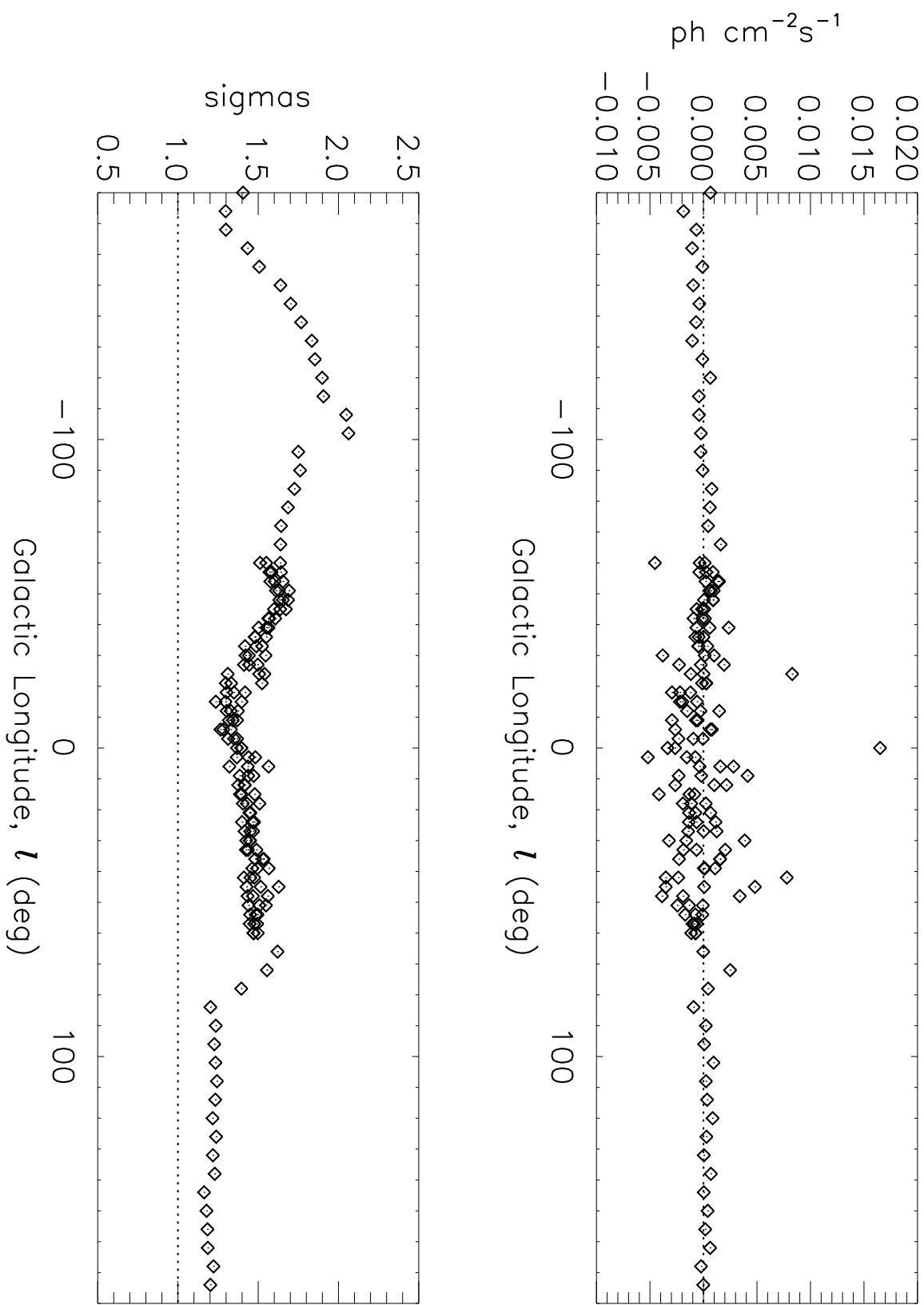


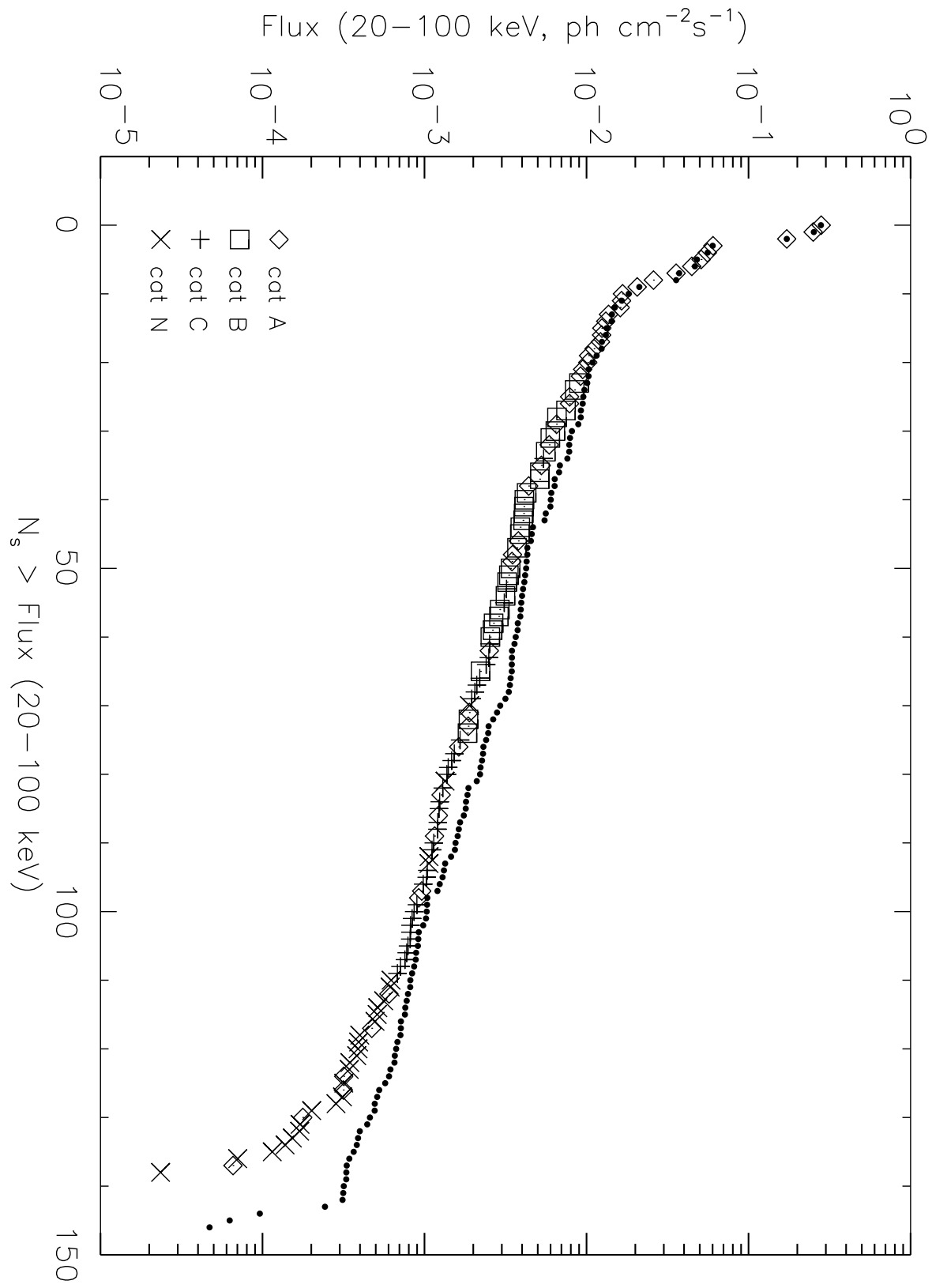


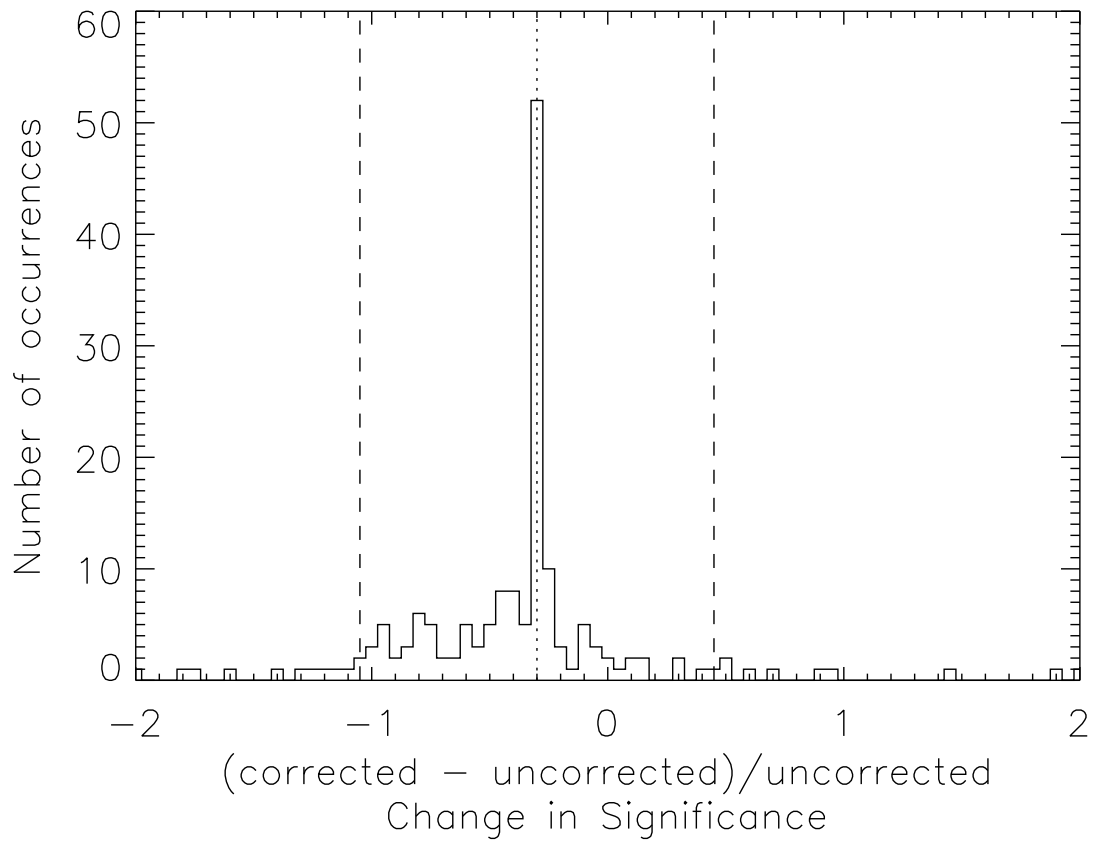


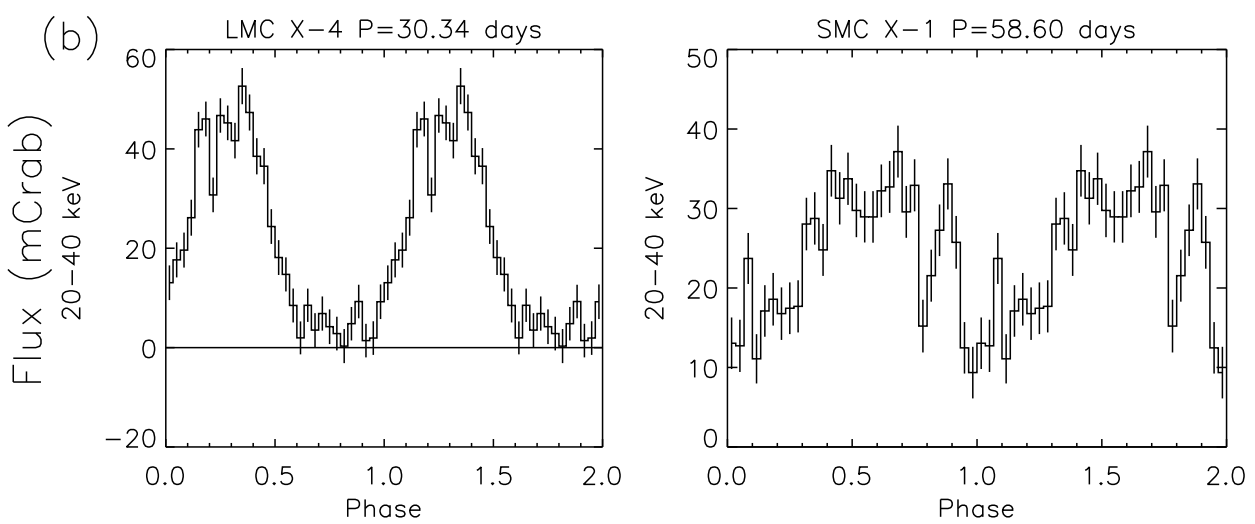
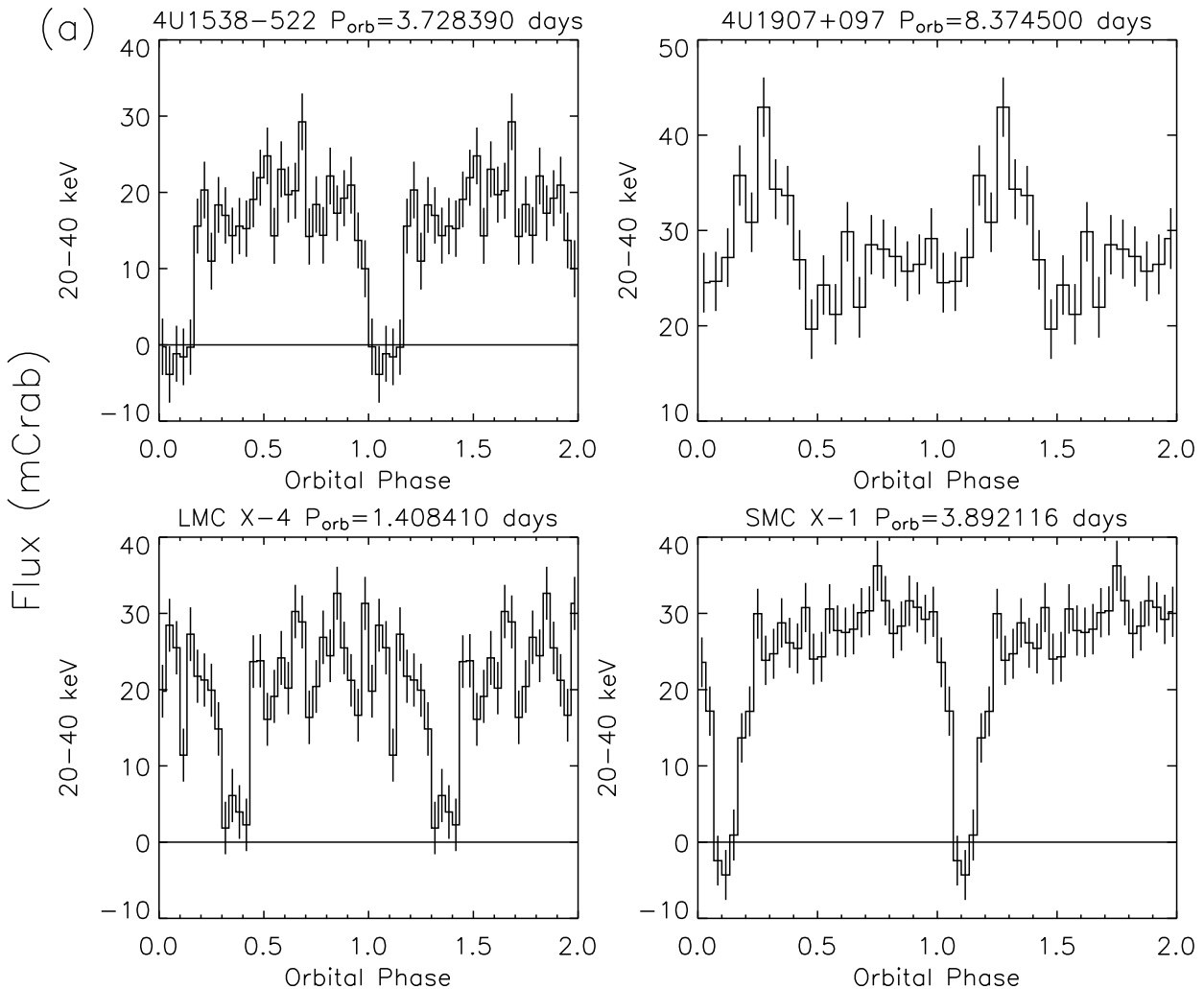


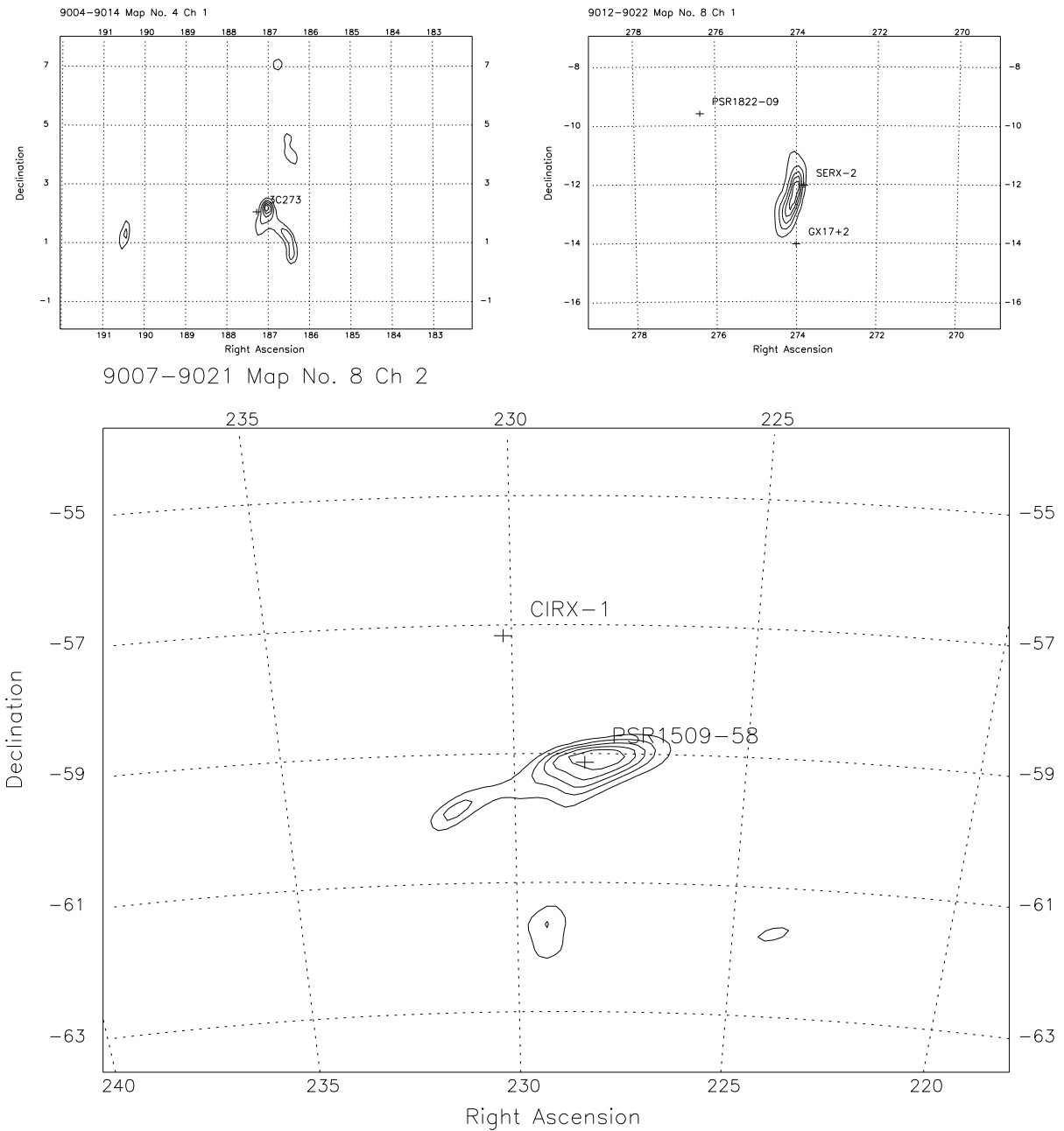












9110-9122 Map No. 2 Ch 1

